ii
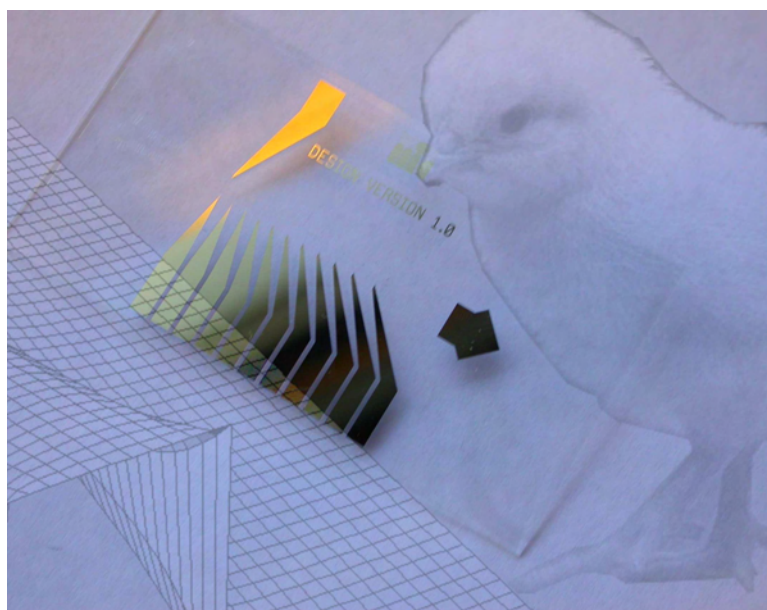
Cell Sorting Using AC Dielectrophoresis

Christian Møller Pedersen

Supervisor: Niels-Asger Mortensen

Co-supervisor: Anders Wolff

MIC – Department of Micro and Nanotechnology
Technical University of Denmark

6 Febuary 2006

Abstract

As the dream of creating a true Lab-on-a-Chip device is closer to realization than ever before, the need for an efficient and reliable sample pre-treatment system is more urgent than ever. The object of a sample pre-treatment system is to separate constituents of interest from those of unimportance or obstruction, before the sample is subjected to the actual analysis. Dielectrophoresis is a term used to describe the motion of dielectric particles, e.g. cells, by means of an AC-electric field. The dielectrophoretic force acts differently on particles of different dielectric properties and can therefore be used to distinguish between these. In this project, a microfluidic device, which uses negative dielectrophoresis to manipulate cells has been designed, fabricated and tested. In addition, analytical solutions to the dielectrophoretic force fields generated by the electrodes in three different cell sorting devices, including the one fabricated, has been obtained. Based on these solutions, a mathematical model for particle sorting has been constructed and applied to the fabricated device. The theoretical predictions of the model have been compared with experimental results where this was possible.

Resumé

I en tid, hvor drømmen om at skabe et ægte Lab-on-a-Chip system nærmer sig virkelighed med stadig større fart, er behovet for et stabilt og effektivt prøve-prepareringssystem mere presserende end nogensinde før. Formålet med et prøve-prepareringssystem er at sortere prøvens interessante bestanddele fra de uinteressante eller problematiske. Dielektroforese er betegnelsen for dielektrikas, f.eks. cellers, bevægelse i et AC-elektrisk felt. Den dielektroforetiske kraft virker forskelligt på dielektrika med forskellige dielektriske egenskaber og kan derfor benyttes til at skelne mellem disse. Jeg har i dette projekt designet, fabrikeret og afprøvet et mikrofluidsystem, som benytter negativ dielektroforese til manipulation af celler. Derudover har jeg fundet analytiske løsninger til det dielektroforetiske kraftfelt, som skabes af elektroderne i tre forskellige celle-sorteringssystemer, herunder det fabrikerede. Baseret på disse løsninger, har jeg udviklet en matematisk model for partikelsorteringsdynamik, som jeg efterfølgende har anvendt på det fremstillede mikrofluidsystem. Modellens teoretiske forudsigelser er blevet sammenholdt med de eksperimentelle resultater, hvor dette var muligt.

Preface

This thesis, titled "Cell Sorting Using AC-Dielectrophoresis" has been submitted to obtain the Master of Science degree at the Technical University of Denmark. The project was carried out with the Microfluidic Theroy and Simulation group at the Department of Micro- and Nanotechnology in the period February 2005 - February 2006 under the supervision of Niels-Asger Mortensen and Anders Wolff.

I shall here take the opportunity to thank both of my supervisors for their assistance during the project as well as Troels Balmer Christensen for his fine collaboration and support all along. I also thank Anders Brask for helping me out on numerous practical issues, Lauritz H. Olesen for inspiring theoretical input, Misha Marie Gregersen for her assistance with the experimental setups, Anders Michael Jørgensen for his advice on SU-8 design, Helle Vendelbo Jensen and Rune Christiansen at DanChip for their assistance, and the MIFTS-group and my fellow-students Thomas Pedersen and Morten Berg Arnoldus for providing good vibes. Finally, I thank Bronwen.

<div style="text-align:center">

Christian Møller Pedersen
MIC – Department of Micro and Nanotechnology
Technical University of Denmark
6 February 2006

</div>

Contents

List of Figures

List of Tables

Chapter 1

Introduction

1.1 Lab on a chip

The idea of downsizing an entire laboratory to the size of a credit card emerged in the early 1990s [3]. The advantages of such a concept are obvious. Miniaturization would provide portability and combined with a high degree of automation make point-of-care analysis possible, e.g. the blood analysis is performed at the doctor's office or even at home by the patient herself. In addition, Lab-on-a-Chip systems would in general provide a faster and less expensive analysis [4] due to the small amounts of reagents needed. A more technical advantage of going to micro-scale is the possibility of manipulating liquids and bio-particles using e.g. electric fields and temperature gradients, which are useless under normal macroscopic circumstances. The fields of application of Lab-on-a-Chip technology include diagnostics, therapeutics, ecological monitoring and drug discovery. It is estimated that the worldwide annual revenues of microfluidic devices today are well beyond $15 billion and growing at a rate of 20% every year [4].

1.2 Objectives and motivation

The group of A. Wolff [5] wishes to realize a Lab-on-a-Chip system, which is capable of detecting food pathogens or equivalent in biological samples. The system will consist of three functional subsystems each of which carries out a specific step in the biochemical analysis. The subsystems are: sample pre-treatment, DNA amplification and detection. The task of the sample pre-treatment subsystem is to separate the potentially present pathogens from the rest of the sample and dispose of the latter. The remaining pathogens will (if present) then be transferred to a micro-chamber in which they will have their DNA extracted and amplified by means of PCR. Finally, the massively amplified DNA is detected, possibly by optical methods. The PCR-process is rather sensitive to contamination, it is therefore crucial for the functionality of the entire device, that an efficient and reliable sample pre-treatment subsystem is engineered.

Seger and collaborators [6] have fabricated and successfully tested a microfluidic device,

which uses negative dielectrophoresis (this term will be explained below) to continuously sort cells. However, the fabrication of this device involves a tedious and error prone alignment of micro-electrodes. As an attempt to avoid the alignment and yet maintain the sorting ability of the device, Wolff has suggested an alternative design. The realization and test of this design has been the objective of the experimental part of this thesis.

While continuous cell sorting using negative dielectrophoresis, as presented by Seger and others, has been successfully realized and reported, little effort has, to my knowledge, been devoted into describing and understanding the dynamics of the sorting process. The main theoretical object of this thesis has therefore been to mathematically model the sorting process and subsequently apply this model to the designs of Seger and Wolff. This should result in a quantitative comparison of the sorting performances of the two designs. Finally, the predictions of the model should be held against the experimental results obtained.

1.3   Introduction to dielectrophoresis

Since the object of this project has been to understand and apply dielectrophoresis, I find it natural to include a brief introduction to this physical phenomenon and its various applications. The term *dielectrophoresis* is due to Pohl (1951, 1978) ([7], [8]). It is defined as the motion of dielectric particles in the presence of an inhomogeneous ac-electric field. Pohl undoubtedly derived the word from the related term *electrophoresis*, which is used to describe the motion of electrically charged particles. Unlike electrophoresis, dielectrophoresis (DEP) does not require particles to be charged in order for them to interact with the electric field, and the DEP-force is insensitive to the field polarity. Basically, a particle can interact with an inhomogeneous ac-field in two ways: either it is attracted towards areas of higher field magnitudes (this we call positive DEP) or it is repelled by such areas (negative DEP). The properties of the particle and the field frequency determine the outcome. Important contributions to the theoretical understanding of DEP were among others given by Kallio (1978) [9] and Jones and Kallio (1979) [10], who unified the theories of Pohl and Kuz'min to give the presently widely used formula for the DEP-force.

The manipulation of dielectric particles using ac-fields is not restricted to translational displacements. Arnold and Zimmermann (1982) [11] were the first scientists to rotate a single cell using a rotating ac-field. The rotational spectrum obtained from this technique, known as electrorotation or *ROT*, has later proven very useful in the investigation of the interior dielectric properties of biological particles. Other manipulation techniques include the 3D *field-cages*, where a three-dimensional electrode configuration generates a local three-dimensional field minimum in which cells can be trapped and confined, as well as *travelling wave* DEP [12], where a travelling electric field moves the cells in a conveyer belt-like fashion.

At the time of its discovery, the field of application of DEP was limited by the lack of high frequency power generators and particularly by the lack of reliable micro-electrode

fabrication techniques. With the emergence of micro-technology, it became possible to manufacture electrodes on the micro-scale allowing generation of the large gradients in field magnitude, which are necessary for the DEP-force to reach a magnitude of practical relevance. The advantages of DEP as a cell manipulating tool became obvious. Of these, Pethig [13] lists the ability of DEP to both attract (positive DEP) and repel (negative DEP) particles and the few requirements to instrumentation. The fact that the DEP handling method requires no prior tagging of the cells in order to manipulate and even distinguish noninvasively between them should also be mentioned. This latter property has inspired many researchers to use DEP as a cell sorting tool. A common approach to sorting [1] is to use positive DEP to hold on to the cells of interest, while the rest is flushed away and then release the cells for further handling. To avoid the discrete steps of which this batch-wise sorting method consists, effort has been put into developing a continuous cell sorting techniques. Markx [14] has thus reported the use of negative DEP to push flowing cells into different regions of a parabolic flow profile hence achieving a spatial dispersion reflecting the dielectric properties of the cells. A similar technique, in which cells travelling in one laminar flow are guided into another by means of negative DEP, has been reported by Doh [15] and, as mentioned, by Seger [6].

1.4 Thesis outline

The chapters of this thesis reflect, to some extent, the time spent on the respective subjects they treat. However, though effort and time devoted to unfruitful experimental approaches, has been documented, their lack of results inevitably introduces some disproportion in retrospect. The thesis is outlined as follows:

- Chapter 2. The aspects of electrodynamics of which we shall make use are presented.

- Chapter 3. Relevant equations governing microfluidcs are outlined and the solutions to two important flow problems are derived.

- Chapter 4. The theory is applied to three electro-fluidic devices in order to solve the dielectrophoretic force field. A mathematical model for cell sorting is presented, and its predictions are accounted for. Minor calculations on cell dielectric properties and the temperature field in the vicinity of electrodes are included as well.

- Chapter 5. The design and fabrication of a microfluidic test device is documented.

- Chapter 6. Experimental results obtained from the testing of the fabricated device are reported and discussed.

Chapter 2

Electrodynamics

2.1 Governing equations

The most important equation for this thesis is undoubtedly the Poisson equation which is given by

$$\nabla^2 \phi = -\frac{\rho_{\text{el}}}{\epsilon}. \tag{2.1}$$

Here ϕ is the electric potential, ϵ is the dielectric permittivity and ρ_{el} is the charge density. In most cases we will be dealing with problems in which $\rho_{\text{el}} = 0$, and in this special case Poisson's equation becomes the Laplace equation

$$\nabla^2 \phi = 0. \tag{2.2}$$

The importance of Eq. (2.1) and Eq. (2.2) owes to the fact that once these partial differential equations have been solved, the electric field is known through ϕ using the defining equation [1]

$$\mathbf{E} \equiv -\nabla \phi, \tag{2.3}$$

and $\mathbf{E}$ is exactly what we need to calculate the dielectrophoretic force $\mathbf{F}_{\text{DEP}}$, which is our ultimate goal. We will go into more details with $\mathbf{F}_{\text{DEP}}$ in the next section. In our calculation of the dielectrophoretic force we will also rely on Ohm's law and charge conservation:

$$\mathbf{J} = \sigma \mathbf{E}, \tag{2.4}$$

$$\nabla \cdot \mathbf{J} = -\partial_t \rho_{\text{el}}, \tag{2.5}$$

where $\mathbf{J}$ is the electric current and σ is the electric conductivity. We shall use Gauss' law for the electric field $\mathbf{E}$ and the electric flux density $\mathbf{D}$:

$$\nabla \cdot \mathbf{E} = \frac{\rho_{\text{el}}}{\epsilon} \tag{2.6}$$

$$\nabla \cdot \mathbf{D} = \rho_f, \tag{2.7}$$

---

[1] which holds given that no time varying magnetic field is present thus ensuring that the rotation of $\mathbf{E}$ is zero according to Faraday's law.

Negatively charged wall

Stern layer   Debye layer
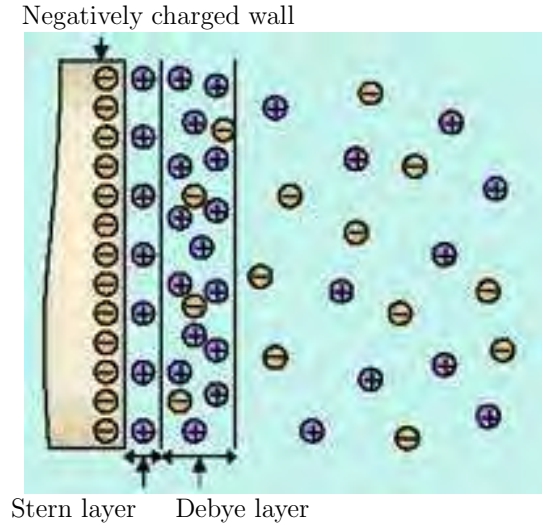
Figure   2.1:   The   Stern   and   Debye   layers   build   up   due   to
ion   exchange   between   channel   wall   and   electrolyte.   Source:
http://www.chemsoc.org/exemplarchem/entries/2003/leeds_chromatography/chromatography/images/

where ρ_f is the free charge distribution. Eq. (2.7) gives us the boundary conditions for $\mathbf{D}$
on the interface between two media:

$$(\mathbf{D}_1 - \mathbf{D}_2) \cdot \mathbf{n} = \sigma_f. \tag{2.8}$$

where $\mathbf{n}$ is a unit vector normal to the interface pointing from media 2 to media 1, and
σ_f is the surface charge.

    Finally, in the case of linear dielectrics we note the relation

$$\mathbf{D} = \epsilon \mathbf{E}. \tag{2.9}$$

2.2   The Debye layer

In any electrolyte which is encaged by walls such as those of channel, ions are exchanged
between the wall and the fluid. The result is a charged wall and an oppositely charged
fluid. However, due to random thermal motions, the wall charge is not perfectly screened
by the ions in the electrolyte. The charging of the electrolyte is strongest close to the
channel wall and gradually decreases as one moves out in the bulk to ultimately reach
neutrality, see Fig. 2.1. The two or three atomic layers of the electrolyte which are
closest to the wall comprise the *Stern layer*. This layer is quite immobile due to its strong
electrical attraction to the charged wall. The next zone of the electrolyte which is also
fairly charged is termed the *Debye layer*. This layer is more mobile than the Stern layer.
We wish to derive an expression for the electric potential ϕ resulting from this local charge

imbalance. Our starting point is the chemical potential μ given by

$$\mu = \mu_0 + kT \ln\left(\frac{c_\pm(\mathbf{r})}{c_0}\right) \pm Z\epsilon_0\phi(\mathbf{r}), \tag{2.10}$$

where k is Boltzmann's constant, T is the absolute temperature, c_0 is the equilibrium ion concentration, $c_\pm$ is the concentration of positive and negative ions, respectively, μ_0 is the chemical potential at zero electric potential and Z is the valence of the symmetric electrolyte. Assuming thermodynamic equilibrium, μ must be constant in space, i.e.

$$kT\nabla \ln\left(\frac{c_\pm(\mathbf{r})}{c_0}\right) = \mp Z\epsilon_0\nabla\phi(\mathbf{r}). \tag{2.11}$$

The boundary conditions for $c_\pm$ and ϕ are

$$c_\pm(z=\infty) = c_0$$
$$\phi(z=\infty) = 0$$
$$\phi(z=0) = \zeta,$$

where z is the distance from the channel wall and ζ by definition is the wall potential. We then get

$$c_\pm = c_0 \exp\left(\mp\frac{Z\epsilon_0}{kT}\phi\right). \tag{2.12}$$

Using Eq. (2.1) and the fact that $\rho_{el}(\mathbf{r}) = Ze(c_(\mathbf{r}) + -c_-(\mathbf{r}))$ for a symmetric electrolyte we get the Poisson–Boltzmann equation

$$\nabla^2\phi = 2\frac{Zec_0}{\epsilon}\sinh\left(\frac{Ze}{kT}\phi\right). \tag{2.13}$$

In the Debye–Hückel limit where the thermal dominates the electrical force ($Ze\zeta \ll kT$), Eq. (2.13) can be linearized to

$$\nabla^2\phi = \frac{2Z^2e^2c_0}{\epsilon kT}\phi. \tag{2.14}$$

The factor on the right hand side is usually written as λ_D^{-2} to get

$$\nabla^2\phi = \lambda_D^{-2}\phi, \tag{2.15}$$

where $\lambda_D = \sqrt{\frac{\epsilon kT}{2Z^2e^2c_0}}$ is the Debye length, the characteristic length over which ϕ falls off. The Debye–Hückel limit is a relevant regime for our purpose and we therefore solve Eq. (2.15) with the infinite parallel plate geometry which gives us the following boundary conditions for ϕ:

$$\phi|_{z=\pm\frac{h}{2}} = \zeta. \tag{2.16}$$

The solution is clearly hyperbolic:

$$\phi = \zeta\frac{\cosh\left(\frac{z}{\lambda_D}\right)}{\cosh\left(\frac{h}{2\lambda_D}\right)}, \tag{2.17}$$

and is depicted in Fig. 2.2.
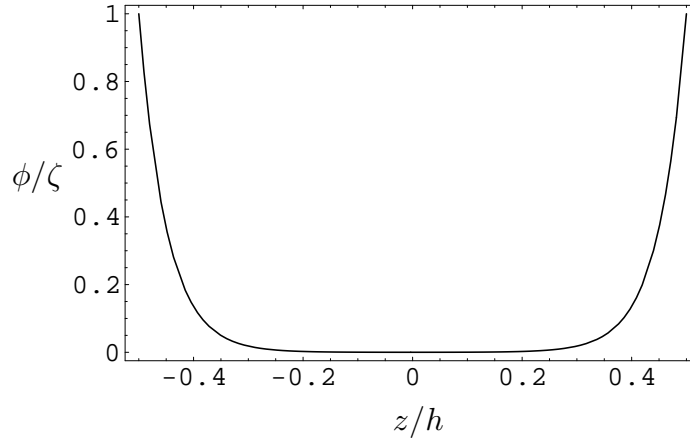
Figure 2.2: The potential generated by the ion transfer between wall and electrolyte. In this plot the ratio $\frac{\lambda_D}{h} = 0.1$ which is unrealistically large, however it makes it easier for the reader to grasp the shape of the potential.

2.3   Dielectrophoresis

2.3.1   Polarization of dielectric sphere by static homogeneous field

When a dielectric particle, e.g. a cell, is subjected to an electric field it will be polarized to a certain extent meaning that the many little dipoles in the particle will tend to align with the $\mathbf{E}$-field. This induced polarization will itself generate an electric field which in turn induces polarization in the particle and so on. We end up with a resulting field $\mathbf{E}_{\mathrm{res}}$ which is a sum of the original field $\mathbf{E}$ and the field generated by the induced polarization $\mathbf{E}_{\mathrm{pol}}$. The problem of finding the resulting field $\mathbf{E}_{\mathrm{res}} = \mathbf{E} + \mathbf{E}_{\mathrm{pol}}$ can be a very complicated task. However, for some particularly simple geometries the problem can be overcome analytically. The homogeneous linear dielectric sphere in a dielectric fluid subjected to a homogeneous electric field is an important example of such geometries. When a dielectric sphere is placed in a homogeneous electric field $\mathbf{E}_{\mathrm{hom}}$, it turns out that it is polarized in such manner that the field $\mathbf{E}_{\mathrm{pol}}$ generated by this polarization corresponds exactly to the $\mathbf{E}$-field from an electric dipole $\mathbf{p}$ placed at the center of the sphere. This dipole is given by [2]

$$\mathbf{p} = 4\pi\epsilon_m \frac{\epsilon_p - \epsilon_m}{\epsilon_p + 2\epsilon_m} a^3 \mathbf{E}_{\mathrm{hom}}, \tag{2.18}$$

where ϵ_p and ϵ_m are the dielectric constants of the particle and surrounding media, respectively and a is the radius of the particle. The fraction which dictates the orientation of $\mathbf{p}$ with respect to $\mathbf{E}_{\mathrm{hom}}$ is called the Claussius–Mossotti factor, $K(\epsilon_p, \epsilon_m)$.

---

[2] The calculation is given in Appendix B.

2.3.2 Dielectrophoretic force on a small particle

The remarkably simple result for the dipole moment of a linear dielectric sphere in a homogenous field given in Eq. (2.18) allows us to treat the particle as a dipole when calculating the force exerted on the particle by the field. The force $\mathbf{F}_{\mathrm{dip}}$ on a dipole situated in a field $\mathbf{E}$ is

$$\mathbf{F}_{\mathrm{dip}} = (\mathbf{p} \cdot \nabla)\,\mathbf{E}. \qquad (2.19)$$

As it appears, it takes a nonzero gradient in the $\mathbf{E}$-field for there to be a net force on the dipole. But this obviously violates the assumption of field homogeneity under which $\mathbf{p}$ was calculated in Eq. (2.18). However, if the particle radius a is much smaller than the characteristic distance d over which $\mathbf{E}$ varies, i.e. $a \ll d$, then the particle will within its near vicinity experience a field which is largely homogeneous and we can justify applying Eq. (2.18) even in an inhomogeneous field. This is known in the literature as *the dipole moment approximation*, see e.g. [16]. The force on the particle, from this point onwards referred to as the dielectrophoretic force $\mathbf{F}_{\mathrm{DEP}}$ is then

$$\begin{aligned}
\mathbf{F}_{\mathrm{DEP}} &= 4\pi\epsilon_m \frac{\epsilon_p - \epsilon_m}{\epsilon_p + 2\epsilon_m} a^3 \left(\mathbf{E} \cdot \nabla\right) \mathbf{E} \\
&= 2\pi\epsilon_m \frac{\epsilon_p - \epsilon_m}{\epsilon_p + 2\epsilon_m} a^3 \nabla \left[\mathbf{E}^2\right].
\end{aligned} \qquad (2.20)$$

Note that in this expression, the electric field only appears as a squared quantity meaning that the direction of $\mathbf{E}$ has no significance for the direction of the DEP-force $\mathbf{F}_{\mathrm{DEP}}$. What dictates the orientation of the DEP force is the gradient of the field and the sign of the Claussius–Mossotti factor. If $K < 0$, the particle will be repelled by areas of high field gradients and we use the term *negative dielectrophoresis* or nDEP. If $K > 0$, the particle will be attracted towards areas of higher field gradients and we use the term *positive dielectrophoresis* or pDEP.

2.3.3 The dielectrophoretic-force generated by an AC-field

We now wish to investigate the dielectrophoretic force when we subject a dielectric particle to a harmonically time varying electric field of the form

$$\mathbf{E}(\mathbf{r}, t) = \mathbf{E}(\mathbf{r})e^{i\omega t}. \qquad (2.21)$$

This time varying field will drive a current inside the particle, and the particle can no longer be considered a perfect dielectric (zero conductivity). If we differentiate Gauss' law Eq. (2.6) with respect to time, using charge conservation Eq. (2.5) and the expression for the field Eq. (2.21) we get

$$i\omega \nabla \cdot \mathbf{E}(\mathbf{r}, t) = -\frac{1}{\epsilon} \nabla \cdot \mathbf{J}(\mathbf{r}, t)$$

$$\Rightarrow \nabla \cdot \left(\epsilon + \frac{\sigma}{i\omega}\right) \mathbf{E}(\mathbf{r}, t) = 0, \qquad (2.22)$$

using Ohm's law Eq. (2.4). If we define a complex permittivity $\tilde{\epsilon} \equiv \epsilon + \frac{\sigma}{i\omega}$, Eq. (2.22) we get

$$\nabla \cdot \tilde{\epsilon} \mathbf{E}(\mathbf{r}, t) = 0,$$

which has the same form as Eq. (2.7). But in the static field problem discussed in Sec. 2.3.1, Eq. (2.7) was just the equation which led to the second of the three boundary conditions Eqs. (B.3), and since the other two boundary conditions are unaffected by the introduction of time dependence, the coefficient B_1 in Eq. (B.5) ends up having the same form as in the static problem with the only difference being the replacement of ϵ_m and ϵ_p by their complex counterparts $\tilde{\epsilon}_m$ and $\tilde{\epsilon}_p$. The solution for $\mathbf{F}_{\mathrm{DEP}}$ therefore becomes:

$$\mathbf{F}_{\mathrm{DEP}}(\mathbf{r}, t) = 2\pi\epsilon_m \frac{\tilde{\epsilon}_p - \tilde{\epsilon}_m}{\tilde{\epsilon}_p + 2\tilde{\epsilon}_m} a^3 \nabla \left[\mathbf{E}(\mathbf{r}, t)^2 \right]. \qquad (2.23)$$

Now, we are really not interested in the temporal variation of $\mathbf{F}_{\mathrm{DEP}}$ during the (typically very short) oscillation period $\frac{2\pi}{\omega}$ so we evaluate the time average of Eq. (2.23) and get

$$\mathbf{F}_{\mathrm{DEP}}(\mathbf{r}) = \pi\epsilon_m \Re \left[\frac{\hat{\epsilon}_p - \hat{\epsilon}_m}{\hat{\epsilon}_p + 2\hat{\epsilon}_m} \right] a^3 \nabla \left[\mathbf{E}(\mathbf{r})^2 \right], \qquad (2.24)$$

which is the result we will be using throughout this thesis. As in the static case, (the real part of) the complex Claussius–Mossotti factor $\mathrm{Re}\,[K]$ plays an important role in determining the sign of $\mathbf{F}_{\mathrm{DEP}}(\mathbf{r})$. However, as opposed to the static case, K is now frequency dependent. This is shown in Fig. 2.3, where we see that particles of different permittivi-
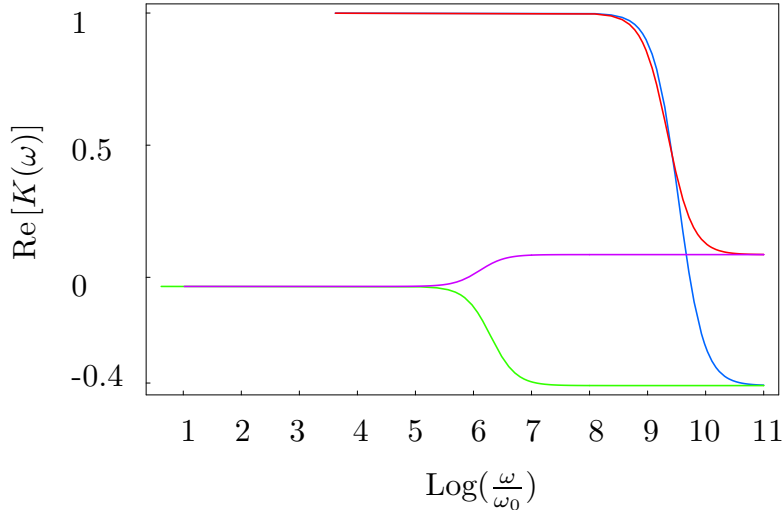
Figure 2.3: Log-plot of the real part of the Claussius–Mossotti factor $K(\tilde{\epsilon}_p, \tilde{\epsilon}_m)$ as a function of frequency ω. The graphs represent four different combinations of permittivities and conductivities for the particle and surrounding media: $\epsilon_p > \epsilon_m \wedge \sigma_p > \sigma_m$ (red), $\epsilon_p > \epsilon_m \wedge \sigma_p < \sigma_m$ (purple), $\epsilon_p < \epsilon_m \wedge \sigma_p > \sigma_m$ (blue) and $\epsilon_p < \epsilon_m \wedge \sigma_p < \sigma_m$ (green).

ties and/or conductivities may experience different types of dielectrophoresis (positive or negative) at a given frequency. For example at $\omega = 10$ GHz, particles represented by the green and blue graphs will experience nDEP, particles represented by the red graph will experience pDEP and particles represented by the purple graph will hardly be affected by the force.

Chapter 3

Hydrodynamics

3.1 Governing equations

3.1.1 Navier-Stokes equation

What Newton's second law is for mechanical particles Navier-Stokes is for fluid particles. Fluid particles are little volumes into which the macroscopic fluid is divided. The particles should be large enough to make random molecular fluctuations insignificant for the particle properties and small enough that the macroscopic physical properties such as temperature, pressure and electric potential do not change significantly within the boundaries of the particle. In practise, a fluid particle can be thought of as a cube of side lengths 10 nm. Newton's 2. law is where we start when we wish to motivate the Navier-Stokes equation,

$$\rho D_t \mathbf{v} = \sum_i \mathbf{f}_i, \tag{3.1}$$

where ρ is the mass density, $\mathbf{v}$ is the velocity vector and $\mathbf{f}$ is a force density acting on the particle. D_t is the so-called material time derivative which is given by [1]

$$D_t = \partial_t + (\mathbf{v} \cdot \nabla). \tag{3.2}$$

The right hand side of Eq. (3.1) is the sum of all (or relevant) force densities acting on the fluid. The force densities relevant in this thesis are the viscous $\mathbf{f}_{\text{visc}}$, the electrical $\mathbf{f}_{\text{el}}$ and the pressure-gradient $\mathbf{f}_{\text{pres}}$ force densities which are given by[2]

$$\mathbf{f}_{\text{visc}} = \eta \nabla^2 \mathbf{v} \tag{3.3}$$

$$\mathbf{f}_{\text{el}} = \rho_{el} \mathbf{E} \tag{3.4}$$

$$\mathbf{f}_{\text{pres}} = -\nabla p, \tag{3.5}$$

---

[1]This expression is obtained by applying the chain rule on the time differential operator d_t which acts on the Lagrangian description of the velocity field $\mathbf{v}(\mathbf{r}(t), t)$.

[2]the expression for $\mathbf{f}_{\text{visc}}$ is only valid provided that the fluid is incompressible (ρ=constant) and that the viscosity η is constant.

where η is the viscosity, ρ_{el} is the charge density, $\mathbf{E}$ is the electric field and p is the pressure. The Navier-Stokes equation then takes the form

$$\rho\left[\partial_t + (\mathbf{v}\cdot\nabla)\right]\mathbf{v} = -\nabla p + \eta\nabla^2\mathbf{v} + \rho_{\mathrm{el}}\mathbf{E}, \tag{3.6}$$

which we shall use in what follows. Though present, gravity is not written explicitly on the right hand side of Eq. (3.6). Instead we redefine the pressure so that it excludes the hydrostatic component which is cancelled by gravity (provided that the channel is not tilted).

3.1.2 Continuity equation

The continuity equation expresses the fact that matter is not created or destroyed but only transported from one place to another. Given a domain Ω, we equate the change in matter within the domain and the net flow of matter $\rho\mathbf{v}$ across the domain boundary $\partial\Omega$:

$$\partial_t \int_\Omega d\mathbf{r}\,\rho = -\int_{\partial\Omega} da\,\mathbf{n}\cdot(\rho\mathbf{v})$$

$$\Rightarrow \int_\Omega d\mathbf{r}\,\partial_t\rho = -\int_\Omega d\mathbf{r}\,\nabla\cdot(\rho\mathbf{v})$$

$$\Rightarrow \partial_t\rho + \nabla\cdot\rho\mathbf{v} = 0, \tag{3.7}$$

which is the continuity equation for compressible fluids. Note that $\mathbf{n}$ is a unit vector normal to $\partial\Omega$ pointing out of Ω, and da is an infinitesimal area element. In the first step we have used that Ω is constant in time and Stokes theorem. If the fluid is incompressible, i.e. $\partial_t\rho = 0$, then we have

$$\nabla\cdot\mathbf{v} = 0. \tag{3.8}$$

3.2 Poiseuille flow

Poiseuille flow is the term used for pressure driven steady state flow in a translationally symmetric channel at the walls of which a zero velocity or *no-slip* condition is assumed satisfied.

3.2.1 The general case

The Navier-Stokes equation Eq. (3.6) is simplified considerably by the steady state assumption which implies that $\partial_t\mathbf{v} = 0$ and even more so by the translational symmetry of the channel in the x-direction which implies

$$\mathbf{v} = v_x(y,z)\hat{\mathbf{x}}, \tag{3.9}$$

and therefore the nonlinear term $(\mathbf{v}\cdot\nabla)\mathbf{v}$ vanishes. Eq. (3.6) then narrows down to (since no electric field is present):

$$\eta\nabla^2\mathbf{v} = \nabla p. \tag{3.10}$$
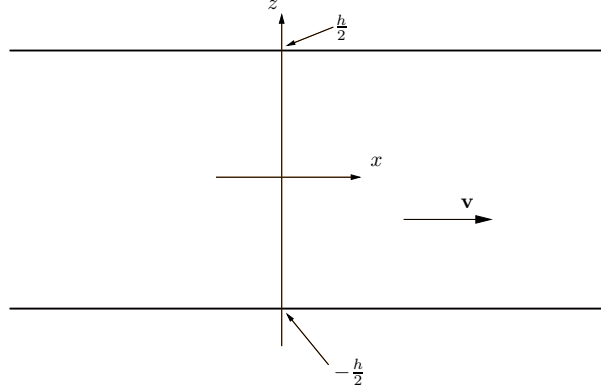
Figure 3.1: Geometry and coordinate system of a channel defined by two infinite parallel plates.

Due to translational symmetry, only the x-component of this equation is non-trivial:

$$\eta \left[\partial_y^2 + \partial_z^2\right] v_x(y, z) = \partial_x p. \tag{3.11}$$

According to Eq. (3.9), the transverse velocity of the fluid is zero and therefore the pressure, being the only driving force can only depend on x. Eq. (3.10) then tells us that $p = p(x) = \alpha x$ since the left hand side is constant with respect to x. The constant pressure gradient α is then given by $\alpha = \frac{\Delta p}{L}$. Our final formulation of the general Poisson flow problem is then

$$\eta \left[\partial_y^2 + \partial_z^2\right] v_x(y, z) = \frac{\Delta p}{L}, \tag{3.12a}$$

$$v_x(y, z) = 0 \quad, \quad (y, z) \in \partial\Omega. \tag{3.12b}$$

3.2.2 Infinite parallel plates

The microsystems we shall treat in this work will have channels of rectangular cross sections, the width of which will be about 6 times the height. One can solve the Poiseuille flow problem for a rectangular cross section, but the solution is not on closed form and therefore cumbersome to treat analytically. Alternatively, one may approximate the wide and shallow channel by two infinitely wide parallel plates, see Fig. 3.1, and then solve Eqs. (3.12) using this geometry. This is what we will do. Making the width of the channel infinite introduces translational invariance in the y-direction as well as the x-direction, wherefore $\partial_y^2 v = 0$, and Eq. (3.12a) reduces to an ordinary differential equation. If we let h denote the distance between the two plates then our Poiseuille flow problem has the form:

$$\eta d_z^2 v_x(z) = \frac{\Delta p}{L}$$

$$v_x|_{z=\pm\frac{h}{2}} = 0, \tag{3.13}$$
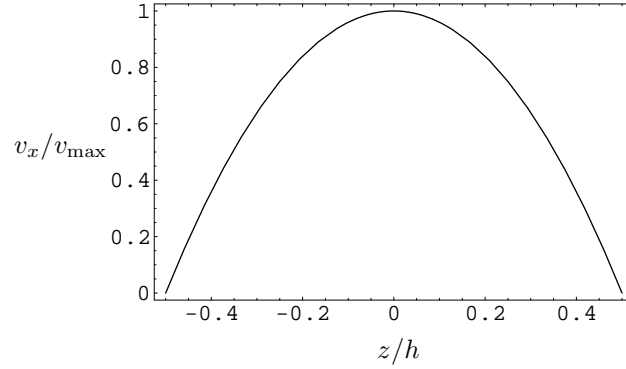
Figure 3.2: The Poiseuille flow profile between two infinite parallel plates given by Eq. (**??**). Here, h is the height of the channel and $v_{\max}$ is the maximum velocity.

and the solution is a simple parabolic flow profile

$$\mathbf{v} = \frac{\Delta p}{2\eta L}\left(\left(\frac{h}{2}\right)^2 - z^2\right)\hat{\mathbf{x}} \tag{3.14a}$$

$$= v_{\max}\left(1 - \left(\frac{z}{h/2}\right)^2\right)\hat{\mathbf{x}} \tag{3.14b}$$

$$= \frac{3Q}{2h}\left(1 - \left(\frac{z}{h/2}\right)^2\right)\hat{\mathbf{x}}, \tag{3.14c}$$

where Q is the flow per unit channel width given by $Q = \int_{-h/2}^{h/2} dz v$. This solution is shown in Fig. 3.2

3.3 Electroosmotic flow

Instead of using pressure as the driving force to generate flow one may set the Debye layer, described in Sec 2.2, in motion by subjecting the fluid to an electric potential gradient parallel to the channel. In the following section we shall explore what happens when an electrolyte enclosed by two infinite parallel plates is biased by an external potential.

3.3.1 EO-flow between infinite parallel plates

The infinite parallel plate geometry is shown in Fig. 3.1. To find $\mathbf{v}$ we must solve the Navier-Stokes equation Eq. (3.6) in which we note the following

$$\nabla p = \mathbf{0}$$
$$\rho_{\text{el}} = -\epsilon\nabla^2\phi_{\text{eq}}$$
$$\mathbf{E} = -\nabla\phi_{\text{ext}}$$
$$\mathbf{v} = v_x(z)\hat{\mathbf{x}},$$
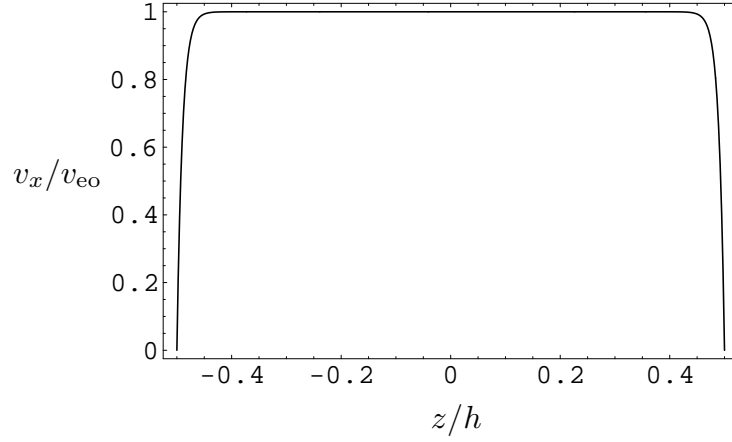
Figure 3.3: The electroosmotic flow profile between two infinite parallel plates as given by Eq. (3.16b). h is the height of the channel and v_{eo} is the maximum velocity. In this plot λ_D/h =???.

where ϕ_{eq} is the potential resulting from the ion transfer between the channel wall and the electrolyte. ϕ_{eq} is given by Eq. (2.17) and from this expression we note that $\partial_x^2 \phi_{\mathrm{eq}} = \partial_y^2 \phi_{\mathrm{eq}} = 0$. Likewise, $(\mathbf{v} \cdot \nabla)\mathbf{v} = 0$ due to translational invariance in the x- and y-directions. Finally, restricting ourselves to the steady state regime we have thus transformed Eq. (3.6) into an ordinary differential equation:

$$d_z^2 \left[v_x(z) + \frac{\epsilon E}{\eta} \phi_{\mathrm{eq}} \right] = 0. \tag{3.15}$$

Integrating Eq. (3.15) twice with respect to z and using the no-slip boundary conditions Eq. (3.13) we get

$$\mathbf{v} = \frac{\epsilon E}{\eta} \left[\zeta - \phi_{\mathrm{eq}} \right] \hat{\mathbf{x}},$$

and inserting Eq. (2.17) for ϕ_{eq}

$$\mathbf{v} = \frac{\epsilon \zeta E}{\eta} \left[1 - \frac{\cosh\left(\frac{z}{\lambda_D}\right)}{\cosh\left(\frac{h}{2\lambda_D}\right)} \right] \hat{\mathbf{x}} \tag{3.16a}$$

$$= v_{\mathrm{eo}} \left[1 - \frac{\cosh\left(\frac{z}{\lambda_D}\right)}{\cosh\left(\frac{h}{2\lambda_D}\right)} \right] \hat{\mathbf{x}}. \tag{3.16b}$$

This solution is plotted in Fig. 3.3. For $\lambda_D/h \ll 1$, $\mathbf{v}$ can be approximated by the constant function

$$\mathbf{v} = v_{\mathrm{eo}} \hat{\mathbf{x}} \tag{3.17a}$$

$$= \frac{Q}{h} \hat{\mathbf{x}}. \tag{3.17b}$$

3.4   Stokes drag force

When a particle such as a cell travels through fluid it will experience a viscous drag opposing its velocity. For a particle of radius a, travelling at constant speed v_0 in a fluid of viscosity η the drag force is given by [17]:

$$\mathbf{F}_{\mathrm{Drag}} = 6\pi\eta a\mathbf{v}. \tag{3.18}$$

This result is only valid in the low Reynolds number regime, $Re \ll 1$, where $Re = \eta a v/\rho$. Inserting our expressions for the velocity fields of Poiseuille and electroosmotic flows Eq. (3.14c) and Eq. (3.17b) gives

$$\mathbf{F}_{\mathrm{Drag,EO}} = 6\pi\eta a\frac{Q}{h}\hat{\mathbf{x}} \tag{3.19}$$

$$\mathbf{F}_{\mathrm{Drag,pres}} = \frac{3}{2}\left(1 - \left(\frac{z}{h/2}\right)^2\right) \times \mathbf{F}_{\mathrm{Drag,EO}}. \tag{3.20}$$

Chapter 4

Modelling

4.1 Cell sorting using dielectrophoresis

As mentioned in section 2.3.2 when dielectric particles are exposed to an inhomogeneous field they may be either attracted to or repelled by the field gradient. In the first case we use the term positive dielectrophoresis and in the latter negative dielectrophoresis. Whether we obtain positive or negative dielectrophoresis (pDEP and nDEP) depends on the conductivity and permittivity of the particle (and fluid), a fact which makes it obvious to attempt to use the DEP-force to distinguish between different particles. However, in order to obtain a significant magnitude of the DEP force, very large field gradients are needed. In fact so large, that they are only achievable in microsystems. This makes cell sorting an interesting application for dielectrophoresis. There exists a wide range of different microfluidic designs which employ dielectrophoresis to sort cells. The basic idea in all of them is to setup a field gradient using an AC-potential at a frequency which causes one type of particles to be repelled by the field gradient whereas the other type will be attracted by it. A common approach is to use pDEP to catch and hold on to the particles of interest while the rest of them is flushed away in the micro channel ([18], [19]). In this chapter, we shall explore electrode designs, which use nDEP to guide cells of interest from one fluid stream to another while leaving those of no interest alone. Three different designs will be treated theoretically and compared as to their cell sorting properties.

4.2 Frequency dependent screening

The sample in which we wish to sort cells will typically be a biological one such as blood or saliva. Such fluids have non-zero conductivities, and the fact that our fluid thus is an electrolyte forces us to take into account the ionic screening of the electric field generated by the electrodes. For DC fields, ions will screen the potential within a few Debye lengths λ_D (see Sec. 2.2) and thus also our opportunity to manipulate cells. However, when we turn to AC-potentials, the ions in the electrolyte will start travelling back and forth in sync with the field. They have no problem doing so in the low frequency regime, but as we crank up the frequency, ω becomes comparable to the inverse response time of the system

Ω^{-1}, where Ω is given by [20]

$$\Omega \sim \lambda_D/d(1+\delta)\omega_D, \tag{4.1}$$

and the ions begin to lack time to fully screen the potential. In Eq. (4.1), d is the characteristic electrode width, δ is the ratio of the Debye layer capacitance and the intrinsic capacitance of the channel wall and ω_D is the Debye frequency. Eventually, as we keep increasing the frequency into the MHz and GHz-regime, the screening effect becomes neglectable and the ions become invisible to the potential. Mathematically this corresponds to gradually leaving the realm of the Poisson equation Eq. (2.1) and entering that of the Laplace equation Eq. (2.2) [21]. As far as particle manipulation using dielectrophoresis goes, we shall always have that $\omega \gg \Omega^{-1}$, thus we only need to concern ourselves with solving the Laplace equation.

4.3   A general tool for solving the potential

To find an analytical expression for the **E**-field and ultimately the DEP-force, we solve the potential, ϕ and then use Eq. (2.3). Since we will be solving three similar Dirichlet-problems with different Dirichlet boundary conditions we wish to develop a general tool for this purpose. We do this using Fourier transforms. The idea is that if we can solve Eq. (2.2) when subjected to a harmonic Dirichlet condition, we can construct solutions to Eq. (2.2) with any Dirichlet condition by linear combination of the harmonic solutions. This fact of course owes to the linearity of the Laplace problem and the completeness of the harmonic functions.

Assume that we have found the solution to the Laplace equation $\phi_q(x,z)$ which satisfies the general harmonic boundary condition such that:

$$\nabla^2\phi_q(x,z) = 0 \quad , \quad (x,z) \in \Omega \tag{4.2}$$

$$\phi_q(x,z_0) = \phi_{q_0}(x) = \exp(-iqx) \quad , \quad z_0 \in \partial\Omega, \tag{4.3}$$

where Ω is the domain of solution. As we shall see, $\phi_q(x,z)$ is a product of two functions each of which only depends on either z or x, respectively. We therefore write:

$$\phi_q(x,z) = \zeta(z)\exp(-iqx) \tag{4.4}$$

and Eq. (4.2) then becomes:

$$\partial_z^2\zeta(z) = q^2\zeta(z). \tag{4.5}$$

Now, suppose we are given an arbitrary boundary condition of the form $\phi_0(x)$ subjected to which we wish to solve the Laplace equation. Due to the linearity of the Laplace equation any linear combination of solutions is itself a solution. We therefore construct a new

solution $\phi(x, z)$ by linear combination of the harmonic solutions:

$$\phi(x, z) = \int_{-\infty}^{\infty} dq A(q) \phi_q(x, z) \tag{4.6}$$

$$= \int_{-\infty}^{\infty} dq A(q) \zeta(z) \exp(-iqx) \tag{4.7}$$

$$= \sqrt{2\pi} \mathscr{F} \left[A(q) \zeta(z) \right], \tag{4.8}$$

where $\mathscr{F}$ denotes a Fourier transform. We demand that this new solution, ϕ, satisfies our given boundary condition $\phi_0(x)$:

$$\phi_0(x) = \phi(x, z_0) \quad , \quad (x, z_0) \in \partial\Omega$$

$$= \int_{-\infty}^{\infty} dq A(q) \phi_q(x, z_0)$$

$$= \int_{-\infty}^{\infty} dq A(q) \zeta(z_0) \exp(-iqx)$$

$$= \sqrt{2\pi} \mathscr{F} \left[A(q) \zeta(z_0) \right]$$

$$\Rightarrow A(q) = \frac{1}{\sqrt{2\pi} \zeta(z_0)} \mathscr{F}^{-1} \left[\phi_0(x) \right]. \tag{4.9}$$

Inserting Eq. (4.9) into Eq. (4.8) we get

$$\phi(x, z) = \mathscr{F} \left[\frac{\zeta(z)}{\zeta(z_0)} \mathscr{F}^{-1} \left[\phi_0(x) \right] \right]. \tag{4.10}$$

As soon as $\zeta(z)$ is found, Eq. (4.10) provides (in principle) a general tool for the solution of ϕ given any boundary condition of the form $\phi_0(x) = \phi(x, z_0)$. To find $\zeta(z)$ we need to further specify the boundary conditions, coordinate system and geometry of the domain Ω in which we wish to solve Eq. (4.5). In the following sections, We will therefore look at specific electrode designs.

4.4 Design 1: Aligned electrodes

In this design, realized by Seger and collaborators [6], two electrodes, each of width d, are located on the channel bottom, $z = -h/2$, and ceiling, $z = h/2$, respectively, see Fig 4.1. The electrodes are placed at an angle θ with respect to the stream direction and are biased by an ac potential difference V. The idea is, that the red particles will experience negative dielectrophoresis and therefore be guided from the sample stream into the buffer stream whereas the green particles will experience no or very little DEP-force which is too weak to hold them against the drag force of the flow and consequently they will slip through the field and remain in the sample stream. The potential ϕ is given by Eq. (4.10), but we need to find $\zeta(z)$ first. We transform the problem into a two-dimensional one in the (x, z)-plane by imagining the channel as being infinitely wide. This means that we will be
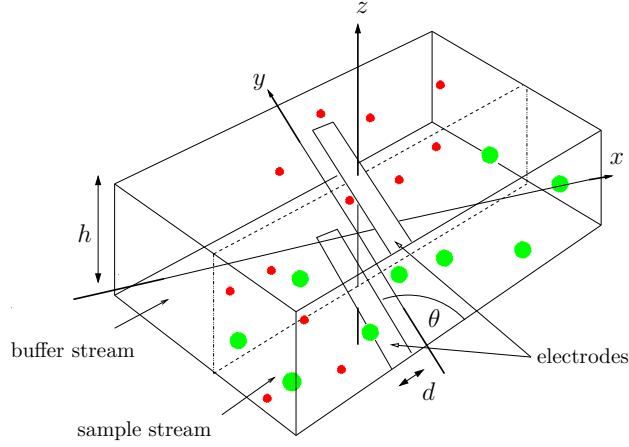
Figure 4.1: The aligned electrodes design (desgin 1).

neglecting boundary effects at the tip of the electrodes. Our boundary value problem is then the following:

$$\nabla^2 \phi_q(x, z, t) = 0, \tag{4.11}$$
$$\phi_q(x, \pm h/2, t) = \mp \exp(-iqx) \exp(-i\omega t). \tag{4.12}$$

The time dependence of ϕ_q is obviously on the form $\exp(-i\omega t)$ and will be omitted in what follows. With the geometry and coordinate system determined we can now insert the trial solution $\phi_q(x, z) = \zeta(z) \exp(-iqx)$ into Eq. (4.12) and obtain the boundary condition for $\zeta(z)$:

$$\partial_z^2 \zeta(z) = q^2 \zeta(z),$$
$$\zeta(\pm h/2) = \mp 1, \tag{4.13}$$

which has the solution

$$\zeta(z) = -\frac{\sinh(qz)}{\sinh(qh/2)}. \tag{4.14}$$

Turning back to Eq. (4.10) we get

$$\phi(\mathbf{r}) = \mathscr{F}_q \left[-\frac{\sinh(qz)}{\sinh(qh/2)} \mathscr{F}_q^{-1} \left[\phi_0(x) \right] \right]. \tag{4.15}$$

To solve the potential ϕ we now only need to formulate the boundary condition $\phi_0(x)$. In the following we will explore two different models of the aligned electrodes design.

4.4.1 The thin electrode model

In this model, the bottom electrode is modelled as an infinitely thin line. This results in the boundary condition:

$$\phi_{1,\delta_0}(x) = \frac{V}{2} d\delta(x), \tag{4.16}$$

where the prefactor follows from the demand that the integral along the boundary should be preserved, i.e.

$$\int_{-\infty}^{\infty} dx \; \phi_{1,\delta_0}(x, \pm h/2) = \int_{-\infty}^{\infty} dx \; \phi_{1,\Theta_0}(x, \pm h/2)$$
$$= \int_{-\infty}^{\infty} dx \; \frac{\mp V}{2}\Theta\left(\frac{d}{2} - |x|\right)$$

Here, $\Theta(\cdot)$ is the Heaviside function and $\phi_{\Theta_0}(x)$ is a hat shaped boundary condition which appreciates the finite width of the electrode, see Fig. 4.3. Inserting Eq. (4.16) into Eq. (4.15) gives us the solution for ϕ:

$$\phi_{1,\delta}(x, z) = -\mathscr{F}\left[\frac{\sinh(qz)}{\sinh(qh/2)}\mathscr{F}^{-1}\left[\frac{V}{2}d\delta(x)\right]\right]$$
$$= -\mathscr{F}\left[\frac{\sinh(qz)}{\sinh(qh/2)}\frac{V}{2}d\sqrt{2\pi}\right]$$
$$= \frac{-Vd}{2h}\frac{\sin(\frac{2\pi}{h}z)}{\cos(\frac{2\pi}{h}z) + \cosh(\frac{2\pi}{h}x)}. \tag{4.17}$$

This solution is plotted in Fig. 4.2(a). The DEP force $\mathbf{F}_{\text{DEP}}$ is then given by:

$$\mathbf{F}_{\text{DEP}_{1,\delta}}(\mathbf{r}) = V^2\frac{a^3}{h^3}\frac{d^2}{h^2}\,\epsilon_m\text{Re}\left[K(\tilde{\epsilon}_m, \tilde{\epsilon}_p)\right] \times 4\pi^4 \frac{-\sinh(2\pi\frac{x}{h})\hat{\mathbf{x}} + \sin(2\pi\frac{z}{h})\hat{\mathbf{z}}}{\left[\cos(2\pi\frac{z}{h}) + \cosh(2\pi\frac{x}{h})\right]^3}. \tag{4.18}$$

Fig 4.2(b) shows a normalized vector plot of $\mathbf{F}_{\text{DEP}_{\delta}}(\mathbf{r})$.

4.4.2 The finite width electrode model

In this model we depart from the delta-function approximation and use a "hat"-function in order to take the finite width of the electrode into account. Our boundary condition becomes:

$$\phi_{1,\Theta_0}(x) = \phi_{1,\Theta}(x, \pm h/2) = \mp\frac{V}{2}\Theta\left(\frac{d}{2} - |x|\right), \tag{4.19}$$

which is depicted in Fig. (4.3). Inserting the hat boundary condition Eq. (4.19) into our

(a) The solution to the potential $\phi_{1,\delta}$ generated by design 1. The electrode potential has been modelled using a Dirac δ-function.

(b) Normalized plot of the corresponding $\mathbf{F}_{\mathrm{DEP}}$. The plot shows the case of negative dielectrophoresis, i.e. $\mathrm{Re}[K] < 0$.
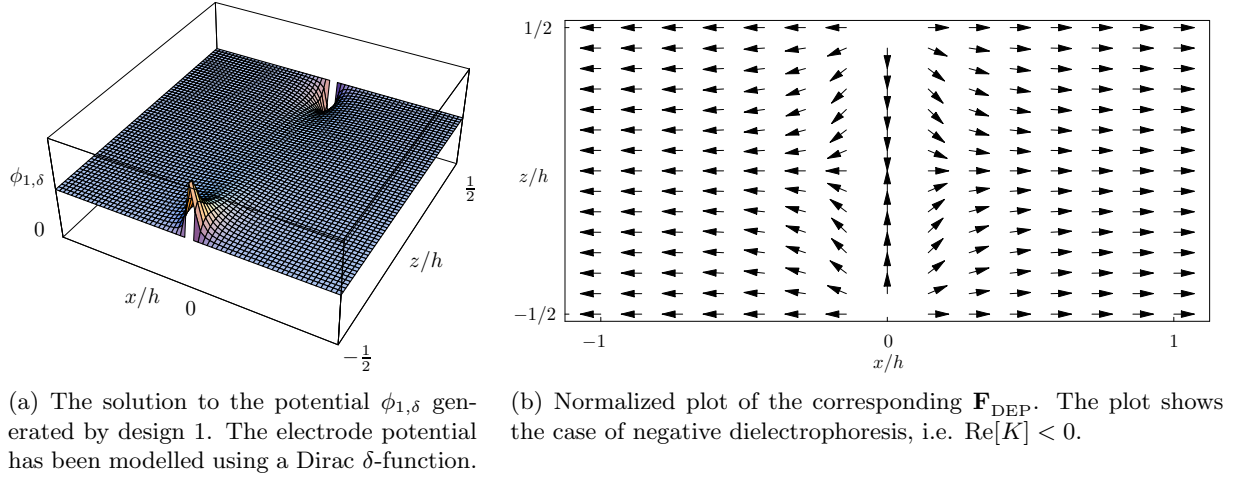
Figure 4.2: Design 1 solutions. The electrode potential has been modelled using a $\delta(x)$-function.
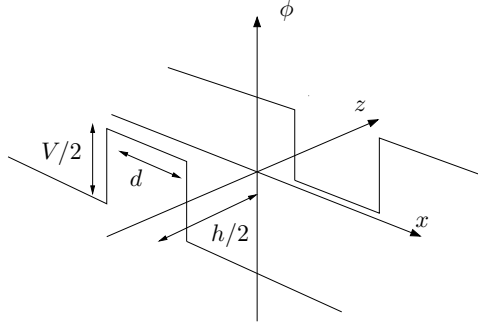
Figure 4.3: Graphical interpretation of the boundary conditions as formulated in the finite width electrode model.

general solution for the aligned electrodes configuration Eq. (4.15) we get:

$$\phi_{1,\Theta}(x,z) = -\mathscr{F}\left[\frac{\sinh(qz)}{\sinh(qh/2)}\mathscr{F}^{-1}\left[\frac{V}{2}\Theta(\frac{d}{2} - |x|)\right]\right]$$

$$= -\frac{V}{2}\mathscr{F}\left[\frac{\sinh(qz)}{\sinh(qh/2)}\frac{\sqrt{\frac{2}{\pi}}\sin(\frac{qd}{2})\Theta(\frac{w}{2})}{q}\right]$$

$$= -\frac{V}{2\pi}\int_{-\infty}^{\infty}dq\,e^{-iqx}\frac{\sinh(qz)}{\sinh(qh/2)}\frac{\sin(\frac{qd}{2})}{q}.$$

Since the left hand side of this equation is real we may conjugate the right side and thereby invert the Fourier transform:

$$-\frac{2\pi}{V}\phi_{1,\Theta}(x,z) = \int_{-\infty}^{\infty} dq e^{iqx} \frac{\sinh(qz)}{\sinh(qh/2)} \frac{\sin(\frac{qd}{2})}{q}$$

$$= \sqrt{2\pi}\mathscr{F}^{-1}\left[\frac{\sinh(qz)}{\sinh(qh/2)} \cdot \frac{\sin(\frac{qd}{2})}{q}\right] \tag{4.20}$$

Now, according to the convolution theorem we have that

$$\sqrt{2\pi}\mathscr{F}^{-1}[f(q) \cdot g(q)] = (\mathscr{F}^{-1}[f(q)] \star \mathscr{F}^{-1}[g(q)]), \tag{4.21}$$

where $\star$ denotes convolution. We then get:

$$-\frac{2\pi}{V}\phi_{1,\Theta}(x,z) = \left(\mathscr{F}^{-1}\left[\frac{\sinh(qz)}{\sinh(qh)}\right] \star \mathscr{F}^{-1}\left[\frac{\sin(\frac{qd}{2})}{q}\right]\right)$$

$$= \left(\frac{\sqrt{\frac{\pi}{2}}\sin(\frac{\pi}{h}z)}{h\left(\cosh(\frac{\pi}{h}x) + \cos(\frac{\pi}{h}z)\right)} \star \frac{1}{2}\sqrt{\frac{\pi}{2}}\left(\text{Sign}(d-2x) + \text{Sign}(\frac{d}{2}+x)\right)\right) \tag{4.22}$$

We note that

$$\text{Sign}(d-2x) + \text{Sign}\left(\frac{d}{2}+x\right) = \begin{cases} 0 & \text{for } |x| > \frac{d}{2} \\ 1 & \text{for } |x| = \frac{d}{2} \\ 2 & \text{for } |x| < \frac{d}{2} \end{cases}$$

and get:

$$\phi_{1,\Theta}(x,z) = -\frac{V\sin(\frac{\pi}{h}z)}{2h}\int_{-\frac{d}{2}}^{\frac{d}{2}} d\tau \frac{1}{\cosh(\frac{\pi}{h}(x-\tau)) + \cos(\frac{\pi}{h}z)}$$

$$= \frac{V}{\pi}\left[\arctan\left(\frac{e^{\frac{2\pi}{h}x} + \cos\left(\frac{2\pi z}{h}\right)}{\sin\left(\frac{2\pi z}{h}\right)}\right) - \arctan\left(\frac{e^{\frac{2\pi}{h}\left(\frac{d}{2}+x\right)} + \cos\left(\frac{2\pi z}{h}\right)}{\sin\left(\frac{2\pi z}{h}\right)}\right)\right.$$

$$\left. - \arctan\left(\frac{e^{\frac{2\pi}{h}\left(\frac{d}{2}-x\right)} + \cos\left(\frac{2\pi z}{h}\right)}{\sin\left(\frac{2\pi z}{h}\right)}\right) + \arctan\left(\frac{e^{-\frac{2\pi}{h}x} + \cos\left(\frac{2\pi z}{h}\right)}{\sin\left(\frac{2\pi z}{h}\right)}\right)\right], \tag{4.23}$$

which is plotted in Fig. 4.4(a). We note that $\phi \to 0$ as $d \to 0$ as it should be. To verify that Eq. (4.23) satisfies the boundary conditions one may investigate the limits $z \to \pm h^{\mp}$ for $|x| > \frac{d}{2}, |x| = \frac{d}{2}$ and $|x| < \frac{d}{2}$ respectively. This is done in Appendix A. We then have:

$$\mathbf{E}_{1,\Theta}(x,z) = \frac{V}{h\left[\cos\left(\frac{\pi}{h}z\right) + \cosh\left(\frac{\pi}{h}\left(\frac{w}{2}-x\right)\right)\right]} \cdot$$

$$\left[-\frac{\sin\left(\frac{\pi}{h}z\right)\left(-1 + e^{\frac{\pi}{h}w}\right)\left(-1 + e^{\frac{\pi}{h}2x}\right)}{2\left[1 + e^{\frac{\pi}{h}(w+2x)} + 2e^{\frac{\pi}{h}\left(\frac{w}{2}+x\right)}\cos\left(\frac{\pi}{h}z\right)\right]}\hat{\mathbf{x}} + \right.$$

$$\left.\frac{\left[\cosh\left(\frac{\pi}{2h}w\right) + \cos\left(\frac{\pi}{h}z\right)\cosh\left(\frac{\pi}{h}x\right)\right]\sinh\left(\frac{\pi}{h}\frac{w}{2}\right)}{\left[\cos\left(\frac{\pi}{h}z\right) + \cosh\left(\frac{\pi}{h}\left(\frac{w}{2}+x\right)\right)\right]}\hat{\mathbf{z}}\right] \tag{4.24}$$

(a) 3D plot of $\phi_{1,\Theta}$ for design 1 in which the electrode potential has been modelled by a hat-shaped boundary condition.

(b) Normalized vector plot of the corresponding $\mathbf{F}_{\mathrm{DEP}}$ in the case of nDEP.

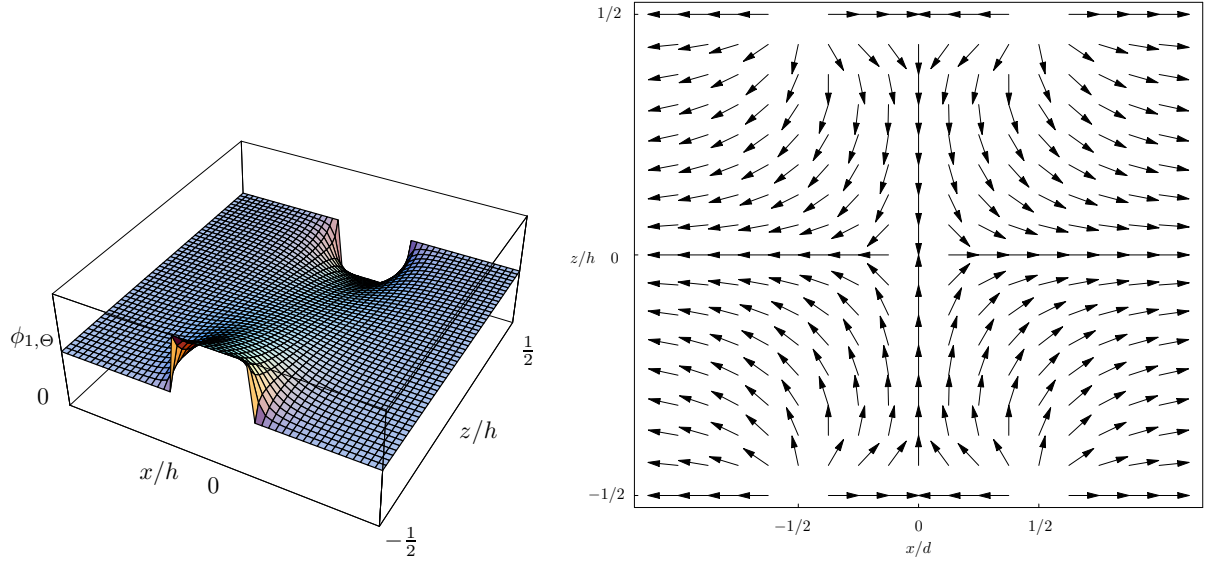Figure 4.4: Design 1 solutions. The electrode potentials have been modelled using a hat-shaped function.

Including the expression $\mathbf{F}_{\mathrm{DEP}}$ is futile due to its complexity. Fig. 4.4(b) shows a normalized vector plot of $\mathbf{F}_{\mathrm{DEP}}$. We see that in essence, the DEP-force field is similar to the solution shown in Fig. 4.2(b), although Fig. 4.4(b) reveals a more complex structure in the region $|x| < d/2$.

4.5   Design 2: Large top electrode

This design is invented by A. Wolff and is similar to the aligned electrodes design in section 4.4 except that the top electrode has been replaced by a large electrode which covers the entire channel ceiling. The design is shown in Fig. 4.5. The Dirichlet problem is outlined in Fig. 4.6. The traditional way to attack such a problem would be to sine- or cosine-Fourier transform the PDE into an ODE in q-space, then solve the ODE and finally transform the solution back into configuration space, see e.g. [22]. However, the success of this method relies on knowing either $\phi(x = 0, z)$ or $\partial_x \phi(x = 0, z)$. In this case, we know by symmetry that $\partial_x \phi(x = 0, z) = 0$, so the cosine-Fourier transform method would be applicable. However, we shall use our own tool which provides an easier way. As in design 1, we will model the small electrode by a hat function or a δ-function. We begin with the latter.

   We take advantage of the linearity of the Laplace equation and split the Dirichlet problem into two, as shown in Fig. 4.6, which we solve independently. The sum of these two solutions $\phi_{\delta,1}$ and $\phi_{\delta,2}$ is then the solution to the composite problem. The boundary
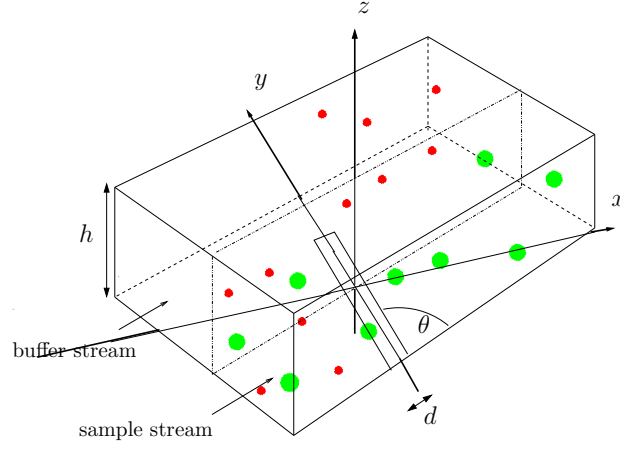
Figure 4.5: The large top electrode design (design 2). The top electrode is transparent in picture.
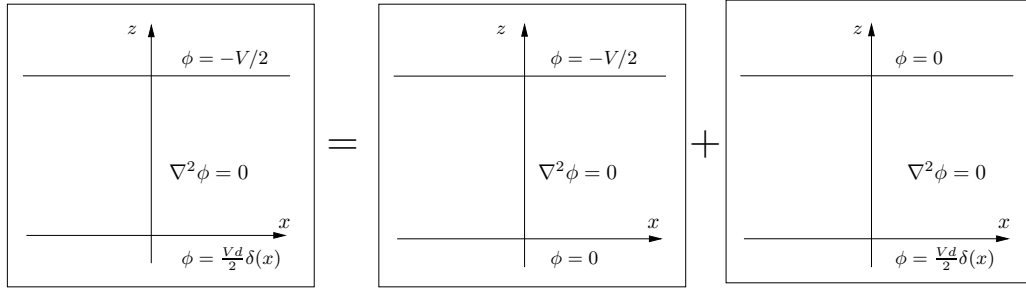
Figure 4.6: The Dirichlet problem of design 2 can be split up in two complimentary Dirichlet problems the solutions of which sum up to give the solution of the original problem.

conditions for $\zeta_1(z)$ and $\zeta_2(z)$ (ζ is defined in Eq. (4.4)) are then changed from Eq. (4.13) to

$$
\begin{aligned}
\zeta_a(0) &= 0 & \zeta_b(0) &= 1 \\
\zeta_a(h) &= 1 & \zeta_b(h) &= 0
\end{aligned}
$$

and the solutions to Eq. (4.5) are

$$
\zeta_a(z) = \frac{\sinh(qz)}{\sinh(qh)}
$$

$$
\zeta_b(z) = 1 - \frac{\sinh(qz)}{\sinh(qh)}
$$

For ϕ_{2,δ_a} we get (inserting into Eq. (4.10))

$$\phi_{2,\delta_a} = \mathscr{F}\left[\frac{\sinh(qz)}{\sinh(hz)}\mathscr{F}^{-1}\left[-\frac{V}{2}\right]\right]$$
$$= -\frac{V}{2h}z,$$

and for ϕ_{2,δ_b} we get

$$\phi_{2,\delta_b} = \mathscr{F}\left[\left(1 - \frac{\sinh(qz)}{\sinh(qh)}\right)\mathscr{F}^{-1}\left[\frac{Vd}{2}\delta(x)\right]\right]$$
$$= -\frac{Vd\sin\left(\frac{\pi z}{h}\right)}{2h\left(\cos\left(\frac{\pi(h+z)}{h}\right) + \cosh\left(\frac{\pi x}{h}\right)\right)},$$

and finally

$$\phi_{2,\delta} = -\frac{V}{2h}z - \frac{Vd\sin\left(\frac{\pi z}{h}\right)}{2h\left(\cos\left(\frac{\pi(h+z)}{h}\right) + \cosh\left(\frac{\pi x}{h}\right)\right)}. \tag{4.25}$$

The potential arising from design 2 is the same as for design 1 (apart from the coordinate shift) with the addition of a linear term in z. The linear term slightly tilts the potential solution in Fig. 4.7(a) compared to Fig. 4.2(a) in which it is horizontal. The DEP-force for the δ-model is given by

$$\mathbf{F}_{\mathrm{DEP}_{2,\delta}} = \frac{V^2\pi^2 d}{4h^5\left(\cos\left(\frac{\pi z}{h}\right) - \cosh\left(\frac{\pi x}{h}\right)\right)^3} \times$$
$$\left[\left(3h + 2d\pi - h\cos\left(\frac{2\pi z}{h}\right) - 2h\cos\left(\frac{\pi z}{h}\right)\cosh\left(\frac{\pi x}{h}\right)\right)\sinh\left(\frac{\pi x}{h}\right)\hat{\mathbf{x}}\right.$$
$$\left. + \left(\left(3h + 2d\pi - h\cosh\left(\frac{2\pi x}{h}\right)\right)\sin\left(\frac{\pi z}{h}\right) - h\cosh\left(\frac{\pi x}{h}\right)\sin\left(\frac{2\pi z}{h}\right)\right)\hat{\mathbf{z}}\right]. \tag{4.26}$$

Fig. 4.7(b) shows a normalized plot of $\mathbf{F}_{\mathrm{DEP}_{2,\delta}}$. Going through the same calculation using the finite electrode-width model we get:

$$\phi_{2,\Theta} = \frac{V}{\pi}\left[\arctan\left(\frac{e^{\frac{\pi}{h}x} + \cos\left(\frac{\pi z}{h}\right)}{\sin\left(\frac{\pi z}{h}\right)}\right) - \arctan\left(\frac{e^{\frac{\pi}{h}\left(\frac{d}{2}+x\right)} + \cos\left(\frac{\pi z}{h}\right)}{\sin\left(\frac{\pi z}{h}\right)}\right)\right.$$
$$\left. - \arctan\left(\frac{e^{\frac{\pi}{h}\left(\frac{d}{2}-x\right)} + \cos\left(\frac{\pi z}{h}\right)}{\sin\left(\frac{\pi z}{h}\right)}\right) + \arctan\left(\frac{e^{-\frac{\pi}{h}x} + \cos\left(\frac{\pi z}{h}\right)}{\sin\left(\frac{\pi z}{h}\right)}\right)\right] - \frac{V}{2h}z \tag{4.27}$$

The algebraic solution for the corresponding DEP-force is of such complexity that it conveys little information. Fig. 4.8(a) shows a plot of the potential solution Eq. (4.27) and
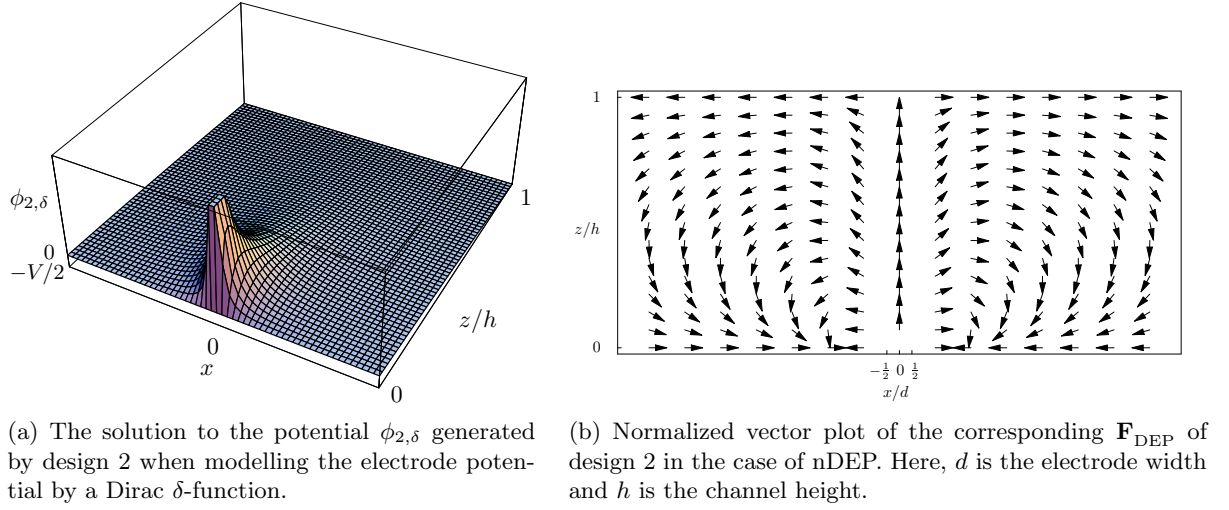
(a) The solution to the potential $\phi_{2,\delta}$ generated by design 2 when modelling the electrode potential by a Dirac δ-function.

(b) Normalized vector plot of the corresponding $\mathbf{F}_{\text{DEP}}$ of design 2 in the case of nDEP. Here, d is the electrode width and h is the channel height.

Figure 4.7: Design 2 solutions. The electrode potential has been modelled using a Dirac δ-function.

a normalized plot for the corresponding DEP-force. The plot reveals that there exist domains in which the DEP force points towards the electrode. This is, however, not at problem as far as particle guiding is concerned, since the magnitude of the DEP-force in these domains is vanishing compared to its magnitude close to the electrode. Consequently, particles exhibiting nDEP will be repelled by the electrode.

4.6 Design 3: Adjacent electrodes

We wish to calculate the potential and the $\mathbf{E}$-field generated by a pair of parallel electrodes both lying on the bottom of the channel. Choi and collaborators [23] have realized designs based on the same principle. The design is shown in Fig 4.9(a). As for the preceding design, we may choose to model this design using the δ-potential or the hat-potential. Accordingly,we get the boundary conditions

$$\phi_{3,\delta}(x, z = 0) = \phi_{3,\delta_0}(x) = \frac{V}{2} d \left(\delta \left(x - \frac{l}{2} \right) - \delta \left(x + \frac{l}{2} \right) \right), \tag{4.28a}$$

$$\phi_{3,\Theta}(x, z = 0) = \phi_{3,\Theta_0}(x) = \frac{V}{2} \left[\Theta \left(\frac{d}{2} - \left| x - \frac{l+d}{2} \right| \right) - \Theta \left(\frac{d}{2} - \left| x + \frac{l+d}{2} \right| \right) \right], \tag{4.28b}$$
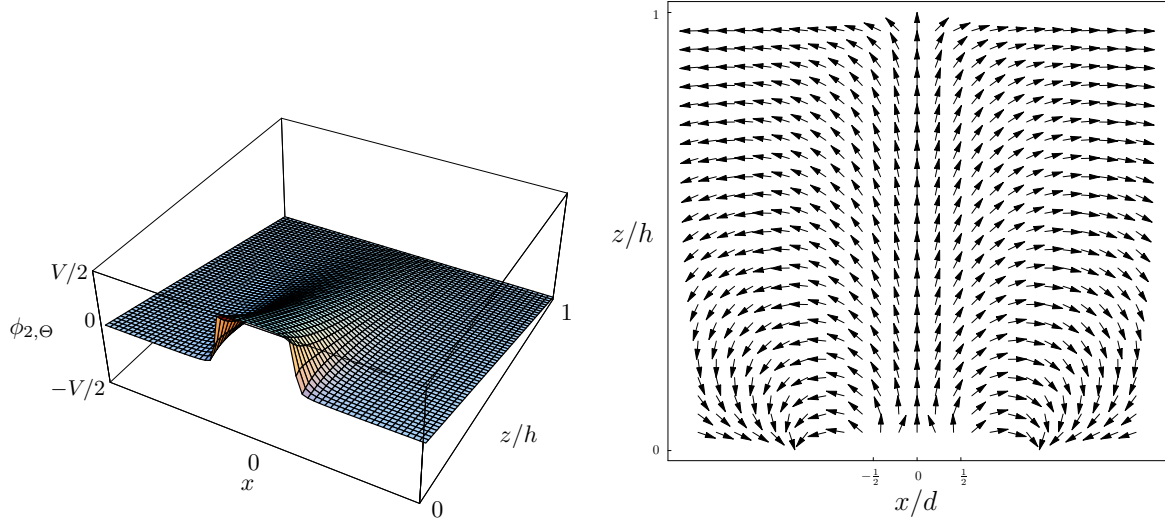
and

$$\phi_{3,\delta}(x, z = \infty) = \phi_{3,\Theta}(x, z = \infty) = 0. \tag{4.29}$$

$\phi_{\Theta_0}(x, z = 0)$ is displayed in Fig. 4.9(b): We use the usual method and start by finding $\zeta(z)$ which must satisfy the boundary conditions:

$$\zeta(\infty) = 0 \tag{4.30}$$

$$\zeta(0) = 1, \tag{4.31}$$

(a) The solution to the potential $\phi_{2,\Theta}$ generated design 2 when the electrode potential is modelled by a hat-shaped function.

(b) Normalized vector plot of the corresponding $\mathbf{F}_{\mathrm{DEP}}$ in the case of nDEP. Here, d is the electrode width and h is the channel height.

Figure 4.8: Design 2 solutions. The electrode potential has been modelled using a hat-shaped function.

in addition to Eq. (4.5). Unsurprisingly, $\zeta(z)$ turns out to be a decreasing exponential function:

$$\zeta(z) = e^{-|q|z}. \tag{4.32}$$

As in Sec. 4.5 the easiest way to attack the adjacent electrodes problem is to take advantage of linearity. We therefore solve the problem in which there is just one electrode centered around $x = 0$. We then get the familiar boundary conditions

$$\phi_{3,\delta_0}(x) = \frac{V}{2}d\delta\left(x\right) \tag{4.33a}$$

$$\phi_{3,\Theta_0}(x) = \frac{V}{2}\Theta\left(\frac{d}{2} - |x|\right). \tag{4.33b}$$

Due to linearity of the Laplace equation, the solution to Eqs. (4.28) can the be constructed by subtraction of two single electrode solutions which have been translated along the x-axis.

The solutions are

$$\phi_{3,\delta}(\mathbf{r}) = \frac{Vdz}{2\pi}\left(\frac{1}{(x-l)^2 + z^2} - \frac{1}{(x+l)^2 + z^2}\right) \tag{4.34}$$

$$\phi_{3,\Theta}(\mathbf{r}) = \frac{V}{\sqrt{2\pi}}\left[\arctan\left(\frac{\pi\left(d - 2\left(x - \frac{l+d}{2}\right)\right)}{z}\right) + \arctan\left(\frac{\pi\left(d + 2\left(x - \frac{l+d}{2}\right)\right)}{z}\right)\right.$$
$$\left. - \left[\arctan\left(\frac{\pi\left(d - 2\left(x + \frac{l+d}{2}\right)\right)}{z}\right) + \arctan\left(\frac{\pi\left(d + 2\left(x + \frac{l+d}{2}\right)\right)}{z}\right)\right]\right], \tag{4.35}$$

(a) Design 3, the parallel adjacent electrodes.

(b) The boundary condition for $\phi_{3,\Theta}$ for the two adjacent electrodes on the channel bottom. d is the width of each of the electrodes and l is the distance between them.
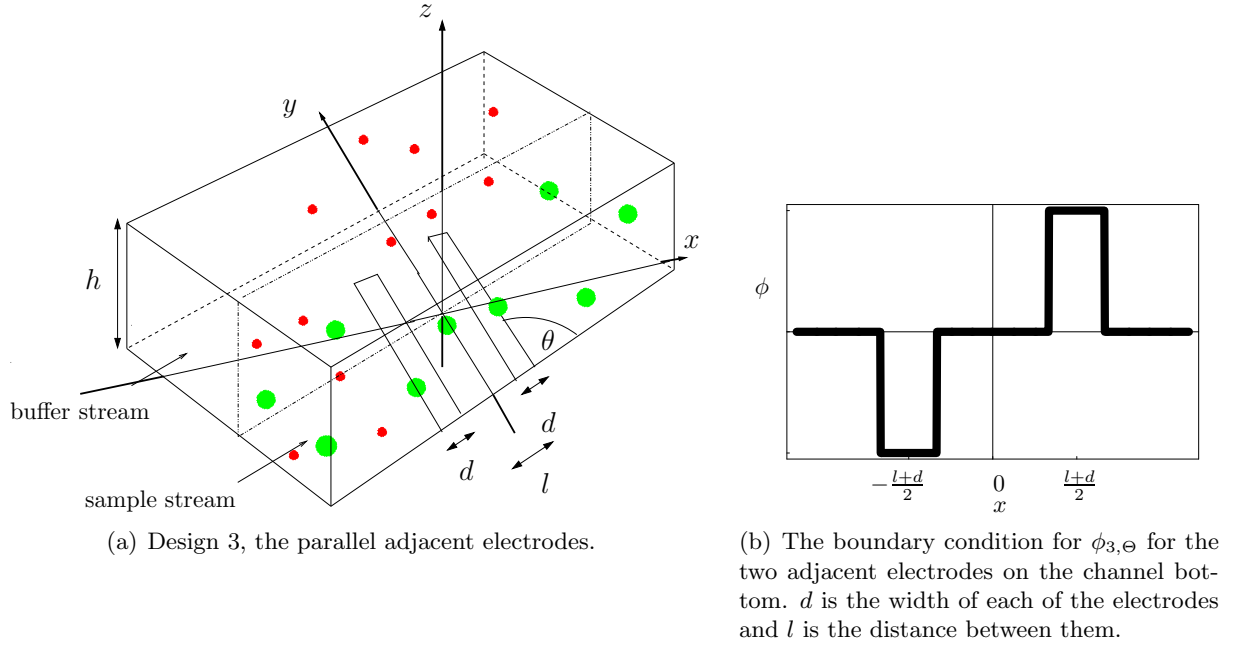
Figure 4.9: Design 3.

which are shown in Fig. 4.10(a) and Fig. 4.11(a) respectively. $\mathbf{F}_{\mathrm{DEP}_{3,\delta}}$ is given by

$$
\mathbf{F}_{\mathrm{DEP}_{3,\delta}} = \frac{8\epsilon_m a^3 \mathrm{Re}\left[K(\tilde{\epsilon}_m, \tilde{\epsilon}_p)\right] d^2 l^2 V^2}{\pi \left(l^4 - 2l^2\left(x - z\right)\left(x + z\right) + (x^2 + z^2)^2\right)^3} \times
$$
$$
\left[x\left(l^4 - 3(x^2 + z^2)^2 + 2l^2(x^2 + 3z^2)\right)\hat{\mathbf{x}} + z\left(l^4 - 3(x^2 + z^2)^2 - 2l^2(3x^2 + z^2)\right)\hat{\mathbf{z}}\right],
$$
$$
(4.36)
$$

and is visualized in Fig. 4.10(b). Again, we omit the expression for $\mathbf{F}_{\mathrm{DEP}_{3,\Theta}}$ due to its complexity, however, a normalized vector plot of the solution is shown in Fig. 4.11(b).

4.7 Cell sorting ability

In order to evaluate the cell sorting ability and suitability of the three electrode designs we need first of all to define what is meant by sorting, secondly we need to identify parameters which are suitable as indicators of sorting performance.

4.7.1 Phase diagrams and maximum electrode angle

Once a cell has passed the tip of the electrode(s) after having been guided by the electric field from the sample stream into the buffer stream, we say that it has been guided, cf. Fig. 4.12. We then define sorting to be guiding of all (relevant) cells irrespective of their vertical position z in the channel. In order for the guiding to happen the DEP force must
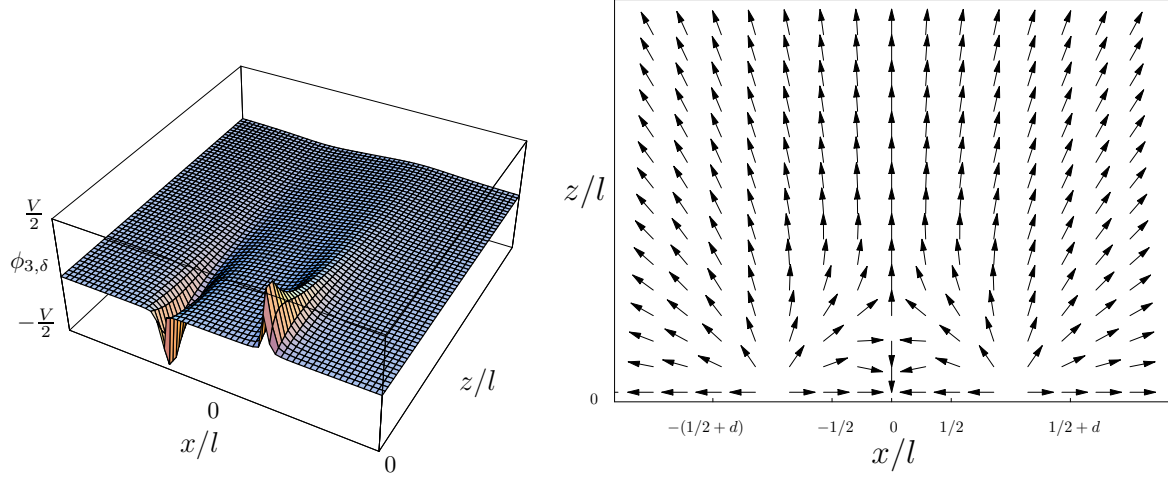
(a) The potential $\phi_{3,\delta}$ generated by two adjacent electrodes modelled by a δ-function boundary condition.

(b) The corresponding nDEP-force.

Figure 4.10: Design 3 solutions modelling the electrodes using $\delta(x)$-boundary condition.

be able to hold the cell against the drag force or more precisely, we must have that the magnitude of $\mathrm{F}_{\mathrm{DEP}_x}$ is equal to or greater than $\mathrm{F}_{\mathrm{Drag}_x}$ at least for one value of x, see Fig. (4.13). If this condition is satisfied for just one value of x, say x_0, the cell will be guided along the plane $x = x_0$. For a cell travelling at vertical position z, our condition for guidance is then

$$\max_x \left[\mathrm{F}_{\mathrm{DEP}_x} \right](z) \geq \mathrm{F}_{\mathrm{Drag}_x}(z) \tag{4.37}$$

Note that we have tacitly assumed that the cell does not shift its vertical position in the channel. Whether this is a reasonable assumption or not is not immediately evident. We know that the calculated DEP forces certainly have non-zero z-components, c.f. Figs. 4.2(b), 4.7(b) and 4.10(b), however these z-components all decrease when the distance to the electrode increases. So whether or not they can be neglected depends on the value of x_0. Since both $\mathrm{F}_{\mathrm{DEP}_x}(z)$ and $\mathrm{F}_{\mathrm{Drag}_x}(z)$ depend on a wide range of parameters, c.f. Eq. (3.19) and for example Eq. (4.18), so does the answer to whether a cell is successfully guided or not. However, in this thesis we are particularly interested in the role played by the electrode angle θ, so we define an indicator function $\Gamma(z, \theta)$ given by

$$\Gamma(z, \theta) = \frac{\max_x \left[\mathrm{F}_{\mathrm{DEP}_x} \right](z)}{\mathrm{F}_{\mathrm{Drag}_x}(z, \theta)}, \tag{4.38}$$

and according to our guiding condition Eq. (4.37) we have guidance for $\Gamma(z, \theta) > 1$. While the nominator of Γ is different for different electrode designs, the denominator is the same for all designs but changes with the flow driving mechanism. The nominator is given by

$$\max_x \left[\mathrm{F}_{\mathrm{DEP}_x} \right](z) = \mathrm{F}_{\mathrm{DEP}_x}(x_{\max}(z), z), \tag{4.39}$$

(a) The potential $\phi_{3,\Theta}$ generated by the adjacent electrodes design when modelled by a step function boundary condition.

(b) Normalized vector plot of $\mathbf{F}_{\mathrm{DEP}}$ generated by two adjacent electrodes when modelled by a step function boundary condition. The case of nDEP is shown. In the plot $l = d = 1$.
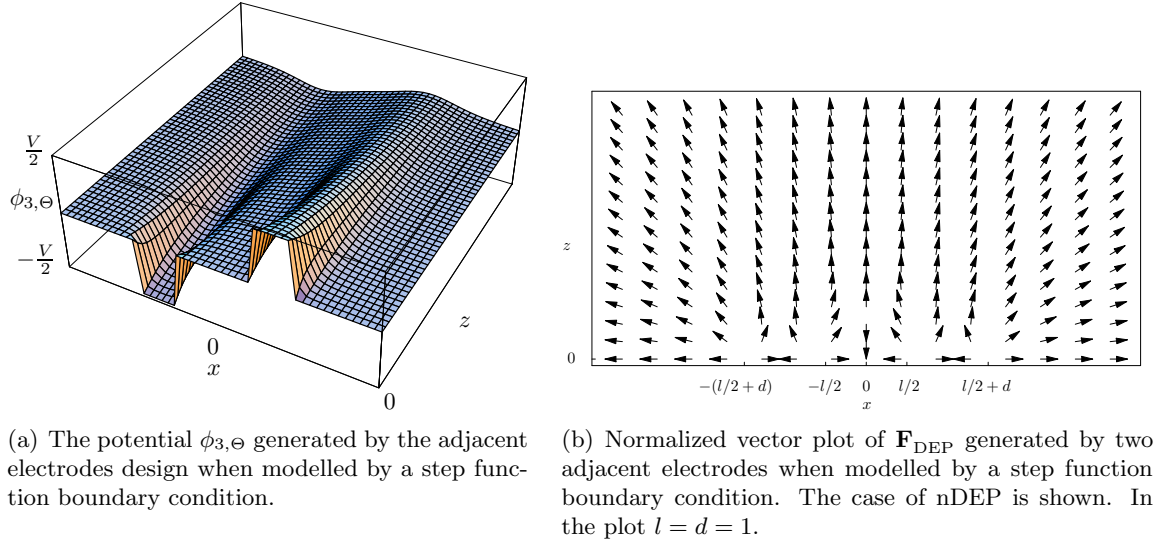
Figure 4.11: Design 3 solutions modelling the electrodes using the hat-shaped boundary condition.

where $x_{max}(z)$ is the solution to $\partial_x \mathrm{F}_{\mathrm{DEP}_x}(x, z) = 0$. Though we have analytical expressions for $x_{\max}(z)$ for all three electrode design, the expressions are all quite complex and therefore provide little insight wherefore we shall not include them here. It is convenient to collect the many different parameters contained in Γ in one or two dimensionless parameters which then characterize the system quantitatively with respect to cell guidance. Design 1 can be characterized by the parameter

$$\gamma_1 = -\frac{\epsilon_m V^2 a^2 d^2 \mathrm{Re}\,[K]}{\eta Q h^4}, \tag{4.40}$$

which is a measure for the extent to which the electro-fluidic system favors the DEP-force over the drag force. Systems which favor the DEP-force are characterized by a large value of γ_1 whereas systems which favor the drag force have low γ_1 values. Design 2 cannot be characterized by one single parameter in the same manner due to the algebraic form of its DEP-force, c.f. Eq. (4.26). Therefore we choose to characterize both design 1 and 2 by two parameters namely

$$\gamma = -\frac{\epsilon_m V^2 a^2 \mathrm{Re}\,[K]}{\eta Q h^2} \tag{4.41}$$

and

$$\chi = \frac{d}{h}. \tag{4.42}$$

These two parameters provide us with a measure of the intrinsic force preference associated with the electro-fluidic system, and because this measure applies to both design 1 and 2, we are able to conduct a meaningful comparison of their guiding performances. Design 3
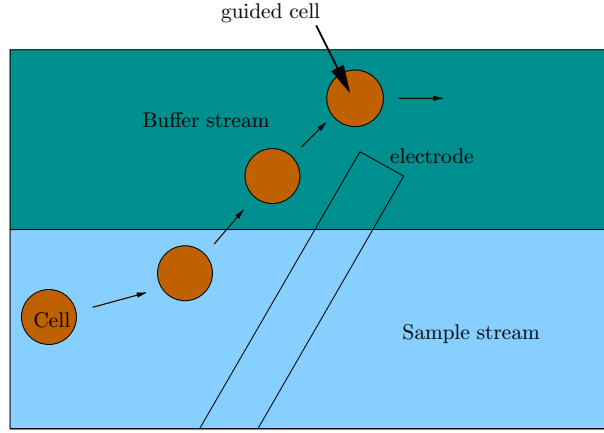
Figure 4.12: Top view of a cell as it travels up the electrode. According to our working definition, a cell is not guided until it passes the tip of the electrode.

differs from the two others by featuring an additional parameter l, the distance between the two electrodes. The characterizing parameter therefore takes a different form

$$\xi = -\frac{\epsilon_m V^2 a^2 d^2 h \mathrm{Re}\,[K]}{\eta Q l^5}. \tag{4.43}$$

If we choose the following typical values for the various parameters: $\epsilon_m = 78$, $V = 10$ V, $a = 5\,\mu$m, $d = 10\,\mu$m, $h = 50\,\mu$m, $|\mathrm{Re}\,[K]| = 0.5$, $\eta = 1 \cdot 10^{-3}$ Pa s, $Q = 6 \cdot 10^{-8}$ m^2 s^{-1}, $l = 20\,\mu$m, we get the values

$$\gamma_0 \sim 6 \tag{4.44a}$$

$$\chi_0 \sim 0.2 \tag{4.44b}$$

$$\xi_0 \sim 20. \tag{4.44c}$$

Note the extreme sensitivity of ξ to the parameter l, which makes it possible to tune the value within several orders of magnitude.

Figs. (4.14) and (4.15) show contour plots of $\Gamma(z, \theta)$ for the three electrode designs at three different values of γ and ξ, namely $\gamma = \{5\gamma_0, 0.5\gamma_0, 0.05\gamma_0\}$ and $\xi = \{5\xi_0, 0.5\xi_0, 0.05\xi_0\}$, respectively. In all plots, $\chi = \chi_0$. Only the contour $\Gamma = 1$ is shown. In the shaded area below this contour, we have $\Gamma > 1$ and cells will be guided and the opposite is the case for the white area above the contour. As expected, the shaded area (the guiding phase) increases in size when γ and ξ does. For design 1, the phase diagram is symmetric with respect to z because both of the forces are. For design 2 and 3, this symmetry is broken by $\mathrm{F}_{\mathrm{DEP}_x}$.
According to our definition of sorting in Sec. 4.7.1, sorting occurs when all cells, irrespective of their vertical coordinate z, are guided by the electrode. In the phase diagrams, the sorting phase is the rectangular area below the horizontal tangent to the $\Gamma = 1$-contour.
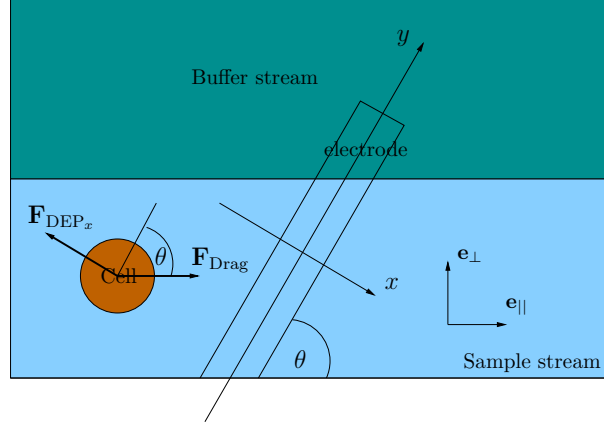
Figure 4.13: A cell approaches the electrode at vertical position z in the sample stream. The drag force has a y- and x-component whereas the DEP force has a z- and x-component of which only the latter can be seen in this 2D picture.

We denote the critical angle identified by this tangent by $\theta^\star$. From the phase diagrams, design 2 appears to be better than design 1 at sorting cells since it has the largest critical angle $\theta^\star$ for all three shown values of γ. The performance of design 3 is not directly comparable to those of the two others due to the difference in characterizing parameters, however, we may say that if the value of the respective characterizing parameters are at the same fraction of the respective typical values, Eq. 4.44, the phase diagrams predict that design 2 will provide the best performance. Fig. 4.16 shows plots of the critical angle $\theta^\star$ below which sorting is achieved as a function of γ and ξ and these plots confirm the tendency suggested by the phase diagrams.

4.7.2 Rapid sorting

In this section we shall optimize θ with respect to the speed at which the cells are guided and sorted. During its journey along the channel, the cell experiences an $\mathbf{F}_{\text{Drag}}$ parallel to the channel walls and an $\mathbf{F}_{\text{DEP}}$ in the x- and z-direction, the strength of which increases as the cell approaches the electrode. The net force is given by (again disregarding the z-component of $\mathbf{F}_{\text{DEP}}$), see Fig. 4.13 :

$$\mathbf{F}_{\text{Net}} = (|\mathbf{F}_{\text{Drag}}| - |\mathbf{F}_{\text{DEP},x}|\sin(\theta))\mathbf{e}_\parallel + |\mathbf{F}_{\text{DEP},x}|\cos(\theta)\mathbf{e}_\perp, \qquad (4.45)$$

where $\mathbf{e}_\parallel$ and $\mathbf{e}_\perp$ are unit vectors parallel and perpendicular to the flow, respectively. As it appears, only $\mathbf{F}_{\text{DEP}}$ contributes to the perpendicular force and velocity $v_\perp$ of the cell. We now assume that the magnitude of $\mathbf{F}_{\text{DEP},x}$ experienced by the cells is neglectable until the cells are at the distance from the electrode at which the guiding condition, Eq. (4.37), is satisfied (this distance is $|x_{\max}(z)|$ which we defined in Sec 4.7.1). This implies that the cells will all be guided across the channel along the same path parallel to the electrode. Now, the guiding will happen at maximum perpendicular speed when the $\mathbf{e}_\perp$-component

(a) Design 1   (b) Design 2   (c) Design 3

(d) Design 1   (e) Design 2   (f) Design 3

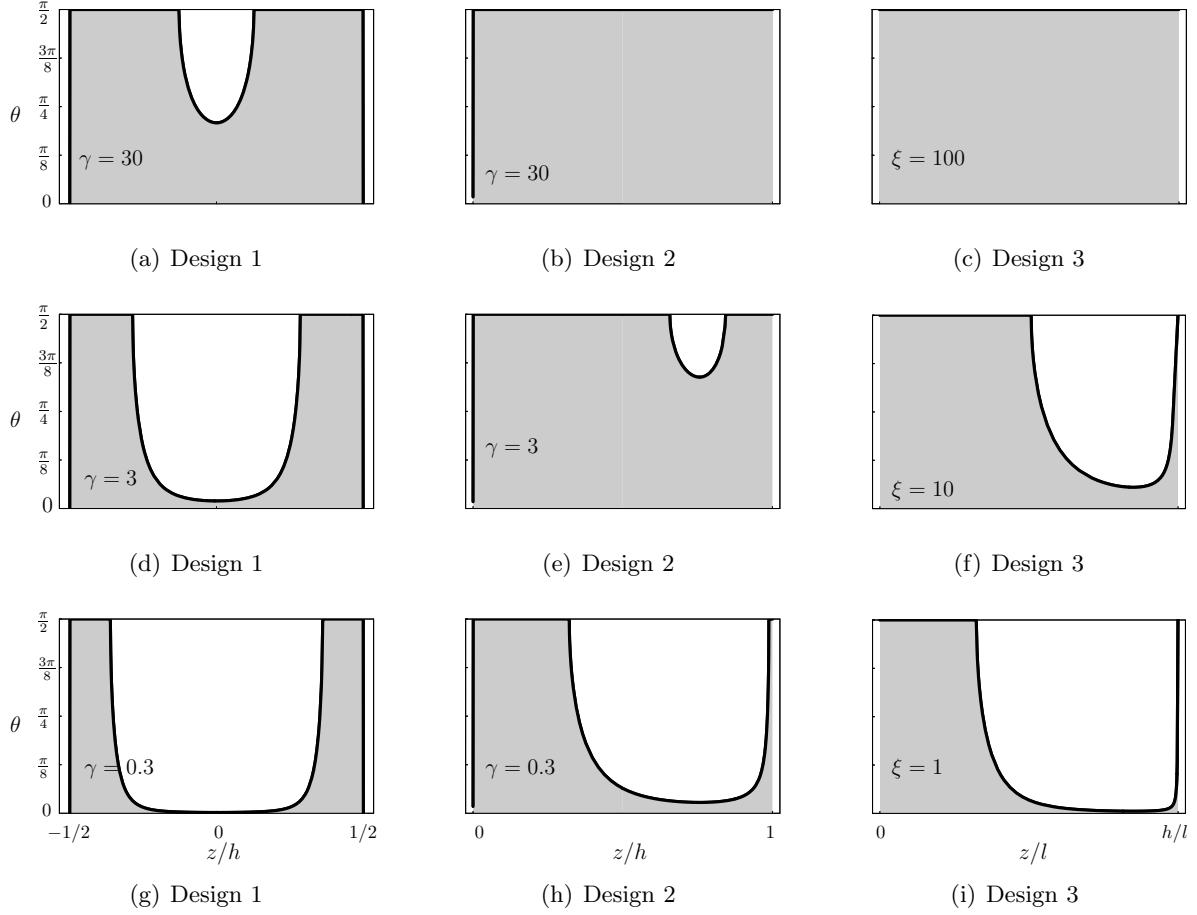(g) Design 1   (h) Design 2   (i) Design 3

Figure 4.14: Phase diagrams for pressure driven flow. The contour $\Gamma = 1$ is shown, and the guiding phase ($\Gamma > 1$) has been shaded. In all plots $\chi = \chi_0 = 0.2$.

of $\mathbf{F}_{\text{Net}}$ is at its maximum. Eq. (4.45) suggests that this happens at $\theta = 0^o$, however, on the guiding path, the guiding condition Eq. (4.37) is satisfied so that:

$$|\mathbf{F}_{\text{DEP},x}| = |\mathbf{F}_{\text{Drag}}| \sin(\theta) \quad , \quad x = x_{\max(z)} \tag{4.46}$$

giving a perpendicular force, $|\mathbf{F}_{\text{Net},\perp}|$:

$$|\mathbf{F}_{\text{Net},\perp}| = |\mathbf{F}_{\text{Drag}}| \sin(\theta) \cos(\theta) \tag{4.47}$$

$$= \frac{1}{2} |\mathbf{F}_{\text{Drag}}| \sin(2\theta), \tag{4.48}$$

which obviously attains its maximum at $\theta = 45^o$. Thus, the angle of maximum perpendicular speed is found as a compromise between two extremes: obtaining the maximum perpendicular component of $\mathbf{F}_{\text{Net}}$ (suggesting $\theta \to 0°$) and shortening the path across the channel (suggesting $\theta \to 90°$).
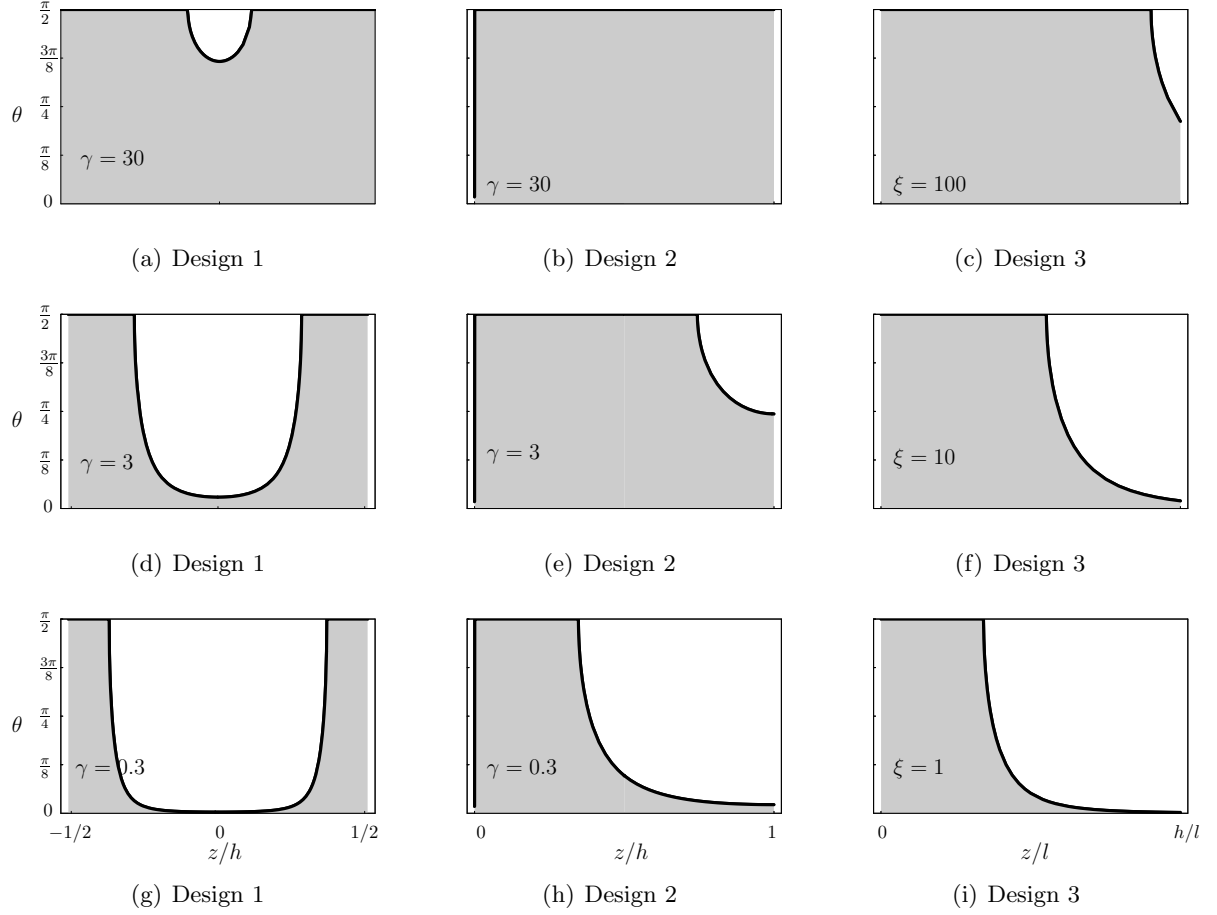
Figure 4.15: Phase diagrams for electroosmotic flow. The contour $\Gamma = 1$ is shown, and the guiding phase ($\Gamma > 1$) has been shaded. In all plots, $\chi = 0.2$.

4.8 Biological particles

4.8.1 Joule heating

With electric current flowing between the electrodes in the microchannel the fluid will be heated due to ohmic resistance. Because high temperatures can damage cells it is relevant to investigate the temperature field in the vicinity of a guiding electrode. The temperature field in a fluid is governed by the temperature balance equation which is given by

$$\rho c_p \left(\partial_t T + \mathbf{v} \cdot \nabla T \right) = k \nabla^2 T + \sigma |\mathbf{E}|^2. \tag{4.49}$$

Here c_p is the specific heat capacity and k is the thermal conductivity. This equation states that the change in temperature over time is caused by either heat convection (second term on l.h.s.), heat diffusion (first term on r.h.s.) or heat generation (second term on r.h.s.). Working in the steady state regime the time dependent term vanishes. Moreover, by dimensional analysis the convection term is dwarfed by the diffusion term and we are left
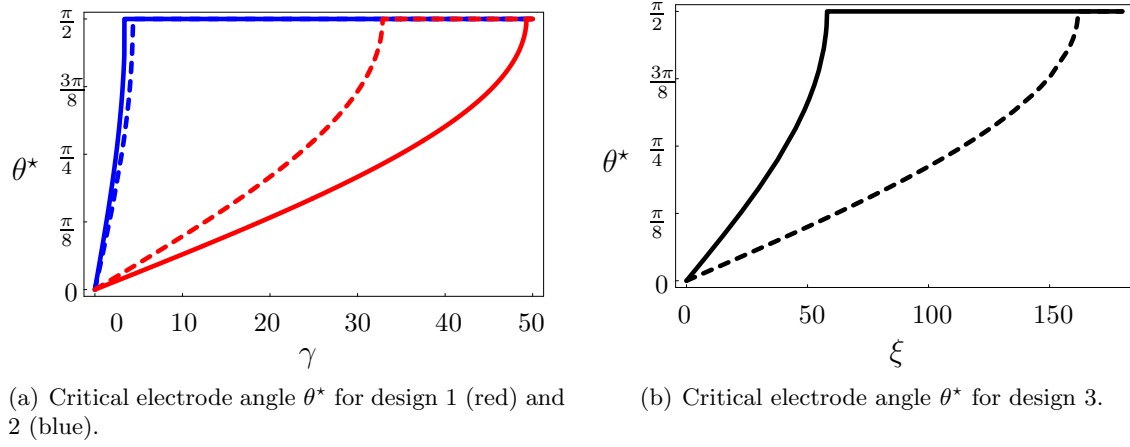
(a) Critical electrode angle $\theta^\star$ for design 1 (red) and 2 (blue).

(b) Critical electrode angle $\theta^\star$ for design 3.

Figure 4.16: The critical electrode angle $\theta^\star$, below which cell sorting is achieved, plotted as a function of the dimensionless force ratios γ and ξ given by Eq. (4.41) and Eq. (4.43). The red graphs represent electrode design 1, and design 2 is represented by the blue graphs. The black graphs represent design 3. Solid lines indicate pressure driven flow, dashed lines indicate EO flow. In all plots, $\chi = \chi_0 = 0.2$.

with[1]

$$0 = k\nabla^2 T + \sigma|\mathbf{E}|^2 \tag{4.50}$$

Knowing $|\mathbf{E}|$ from our potential solutions ϕ, it is a simple task to solve Eq. (4.50) numerically. Fig. 4.17 shows a numerically obtained contour plot of $T(x,z)$ for the electrode geometry of design 2 , see Sec. 4.5, using the finite width electrode model. Modelling the surroundings as an infinite heat bath, we use a constant boundary condition ($T = 20°C$). The plot reflects the fact that $|\mathbf{E}|$ has its maximum at the edge of the electrode, and we see that the temperature is at most raised by approximately one degree above the surrounding heat bath. This result can be regarded as a safe estimate, since the model does not appreciate the cooling impact of convection.

4.8.2 The Claussius–Mossotti factor for yeast

Throughout this chapter we have treated the cells as homogeneous dielectric spheres characterized by one permittivity ϵ_p and one conductivity σ_p. Real cells, however, have quite complex structures, see Fig. 4.18(a). Roughly, eukaryotic cells consist of a nucleus wrapped in a nuclear membrane which in turn is surrounded by cytoplasm in which a massive amount of different enzymes and organelles float around. The cytoplasm is surrounded by the cell membrane and possibly a cell wall. In order to grasp the most important features of this structural complexity, we expand our crude homogeneous model to a spherical shell structure in which each shell is characterized by a permittivity, conductivity and thickness. This model is sometimes referred to as the *smeared-out sphere* model in the literature. The simplest case is the single shell model, which mimics the nucleus and the surrounding cytoplasm, see Fig. 4.18(b). Subjecting this composite body

---

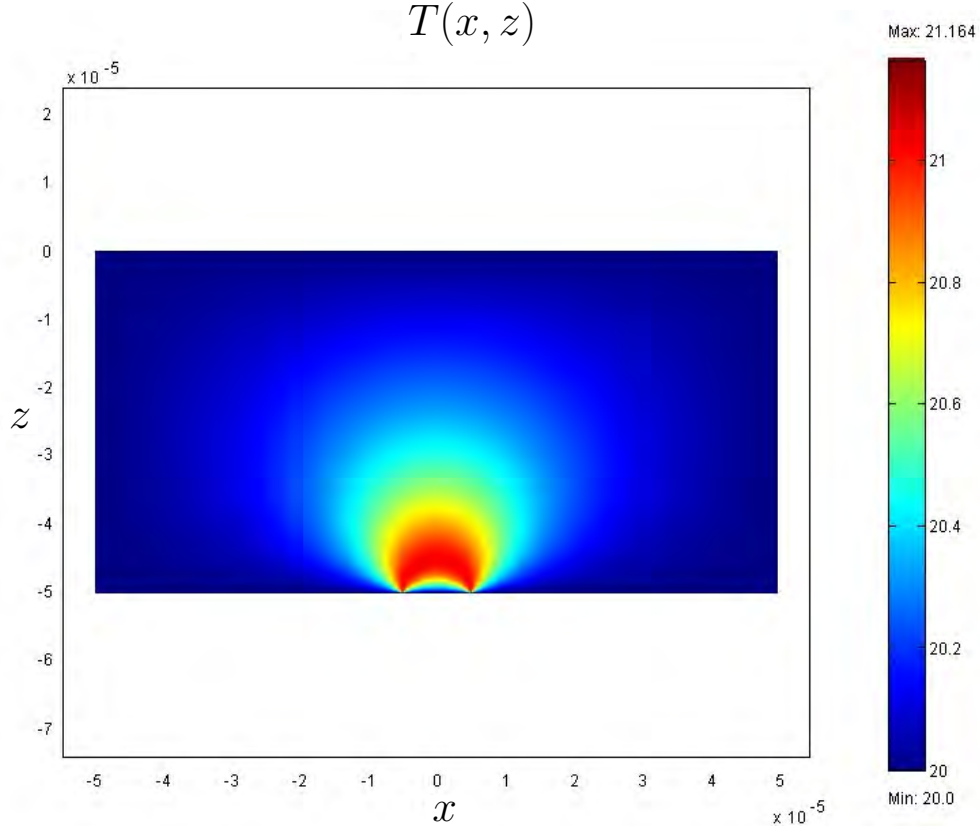[1]Please refer to Morgan & Green [24] for the full derivation.

Figure 4.17: Contour plot of the temperature field $T(x, z)$ obtained from a numerical calculation based on Eq. (4.50). The calculation made for electrode design 2 and the parameter values are $k = 0.6$ W m^{-1} K^{-1}, $\sigma = 0.055$ S m^{-1}, $V = 10$ V, channel height h is 50 μm, and the electrode width d is 10 μm.

to a homogeneous electric field, we now wish to find the effective dipole moment as we did for the homogeneous sphere in Appendix B. The boundary conditions are

$$\phi_3|_{r=R_2} = \phi_2|_{r=R_2}$$
$$\phi_2|_{r=R_1} = \phi_1|_{r=R_1}$$
$$\epsilon_3\partial_r\phi_3|_{r=R_2} = \epsilon_2\partial_r\phi_2|_{r=R_2}$$
$$\epsilon_2\partial_r\phi_2|_{r=R_1} = \epsilon_1\partial_r\phi_1|_{r=R_1}.$$

We need only ϕ_1 to find the dipole moment and interestingly the solution is given by [25]

$$\phi_1 = -E_0 r \cos(\theta) + \frac{\epsilon_2' - \epsilon_m}{\epsilon_2' + 2\epsilon_m} a^3 E_0 \frac{\cos(\theta)}{r^2}, \tag{4.51}$$
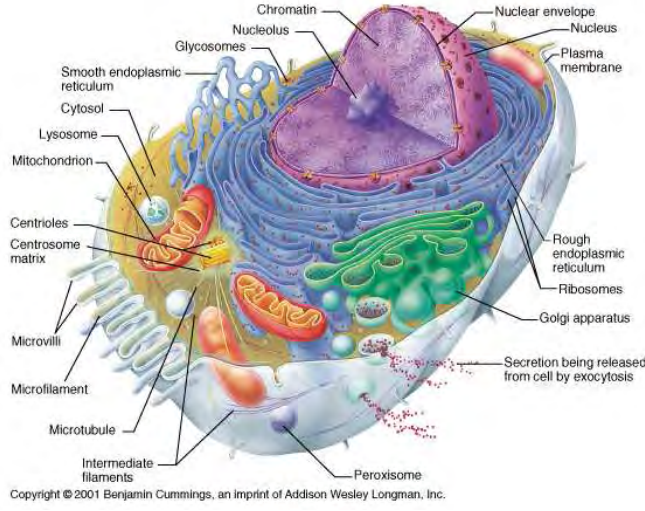
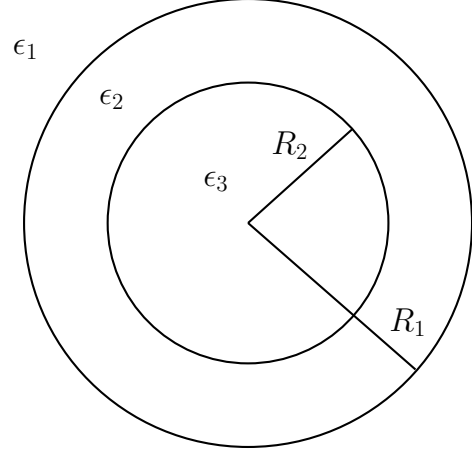(a) Basic anatomy of a eukaryotic cell. Source: www.octc.kctcs.edu/gcaplan/anat/Notes/

(b) The spherical single shell model consists of a core of radius R_2 and permittivity ϵ_3 surrounded by a shell of outer radius R_1 and permittivity ϵ_2. The medium permittivity is ϵ_1.

Figure 4.18: Cell and cell model.

where

$$\epsilon_2' = \epsilon_2 \frac{\left(\frac{R_1}{R_2}\right)^3 + 2\frac{\epsilon_3-\epsilon_2}{\epsilon_3+2\epsilon_2}}{\left(\frac{R_1}{R_2}\right)^3 - \frac{\epsilon_3-\epsilon_2}{\epsilon_3+2\epsilon_2}}.$$

We immediately note that the potential solution Eq. (4.51) has the exact same form as for the homogeneous dielectric sphere Eq. (B.6) if ϵ_p is replaced by ϵ_2'. Hence, ϵ_2' is to be thought of as an effective permittivity of the single shell structure. Hence, we have reduced a 1-shell structure to an 0-shell structure by introducing an effective permittivity. But then, by applying this substitution n times on an n-shell structure starting with the core and inner shell and working our way out, we can reduce any multi-shell structure to a homogeneous sphere characterized by one effective permittivity ϵ_1' which comprise all the permittivities. Of course this happens at the cost of an increasingly more complex algebraic expression for the permittivity.

Since we are in essence back at the problem of a homogeneous sphere, we may replace the permittivities by complex permittivities as we did in Sec. 2.3.3 thereby rendering the model frequency dependent. As an attempt to predict the frequency dependence of the Claussius–Mossotti factor for yeast cells (*Saccharomyces cerevisiae*), we perform a four shell model calculation using data on ϵ, σ and shell thicknesses from the literature, see table 4.1.

The result is shown in Fig. 4.19. In general, the more shells we introduce to our model the more details in the spectrum of $K(\omega)$ are we able to appreciate. However, the

Cell Compartment	Thickness	ϵ_r	σ^2 $[10^{-4}\text{S m}^{-1}]$
Interior	3.0 μm	51	12000
Membrane	3.5 nm	3.0	0.046
Periplasmic space	25 nm	14.4	41
Inner wall	110 nm	60	62
Outer wall	50 nm	5.9	200

Table 4.1: Dielectric data for *Saccharomyces cerevisiae* (yeast) obtained from the literature [2]. The conductivities have been measured at a medium conductivity of 90 μS m^{-1}.

introduction of additional shells beyond the 4th or 5th shell will only rarely reveal new peaks and plateaus in the spectrum.

4.9 Summary of chapter 4

The dielectrophoretic force fields of three different cell guiding electrode designs have been solved. This has been done by solving the electric potential in the high frequency limit in which it is effectively governed by the Laplace equation. For each design, two different models of the Dirichlet boundary conditions have been applied and the solutions have been found using a Fourier transform tool particularly well-suited for the channel geometry. Furthermore, criteria for successful cell guiding have been pinpointed and the cell guiding ability of each electro-fluidic design has been quantitatively characterized by one (or two) dimensionless parameters. Based on the guiding criteria identified, predictions have been made concerning the general form of the guiding and non-guiding domains in (z, θ)-space, where θ is the electrode angle and z is the vertical coordinate of the channel. In particular, the value of the critical angle, below which all cells are guided, has been predicted.

A numerical calculation of the temperature field in the vicinity of the electrode has been performed. The temperature is expected to be higher near the electrode than elsewhere due to Joule heating caused by the relatively dense current in this area. Finally, the spectrum of the real part of the Claussius–Mossotti factor for yeast has been calculated using a spherical four shell dielectric model for the cell.
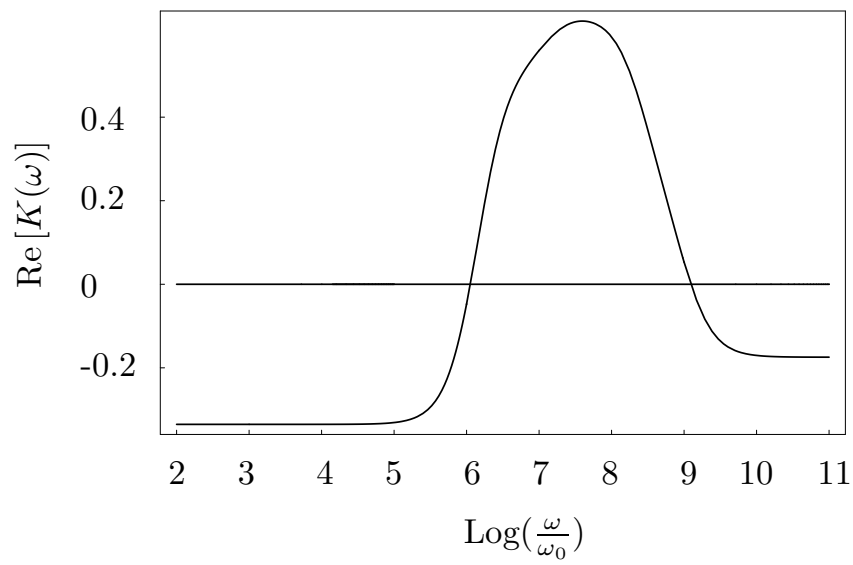
Figure 4.19: The frequency dependence of the Claussius–Mossotti factor when calculated from a spherical four shell model using the parameters from Table 4.1.

Chapter 5

Device fabrication

Electrode design 1 from sections 4.4 has been realized and tested in practise ([6],) and design 3 from Sec. 4.6 is a typical planar electrode design which is well-described in the literature. Design 2, on the other hand, is interesting because it combines a cell sorting ability which is better than that of the two others with a fabrication simplicity comparable to that of design 3. As to the cell sorting capabilities of the three designs, these are described in Sec. 4.7.1. As to fabrication, design 2 is considerably less cumbersome to fabricate than design 1 since the need to define and align electrodes on the channel lid has been eliminated by the introduction of the large top electrode.

We have chosen to realize design 2 on a micro chip using a Borofloat® glass wafer as the substrate material and gold for the bottom electrode. For the large top electrode we use indium tin oxide (ITO) due to the transparency of this material. In order to test our theoretical predictions concerning the critical electrode angle $\theta^\star$ in Sec. 4.7, we have designed a chip which contains a row of electrodes all making different angles with the flow direction. In the following sections, two different chip fabrication approaches are described: the SU-8-chip and the double-sided tape-chip (DST-chip). At the time of writing, only the DST-chip has proven successful, however the SU-8 approach has not been abandoned and the exploring of it accounts for a considerable part of the time spent in the project and it will therefore be treated accordingly in this thesis.

The fabrication sections offer a brief description of the most important steps in the fabrication processes and the reader may refer to Appendices C and D for the detailed process protocol.

5.1 The SU-8 chip

5.1.1 Design

To keep things as simple as possible, our chip consists of one main channel with three inlet channels and two outlet channels connected to each end, see Fig. 5.1. The channels are 300 μm wide. In Fig. 5.1, objects in red represent structures to be made in polymer, more specifically the photo resist SU-8, and black represents gold structures. Though it is not clear from the drawing, the metal layer will be lying underneath the polymer layer on
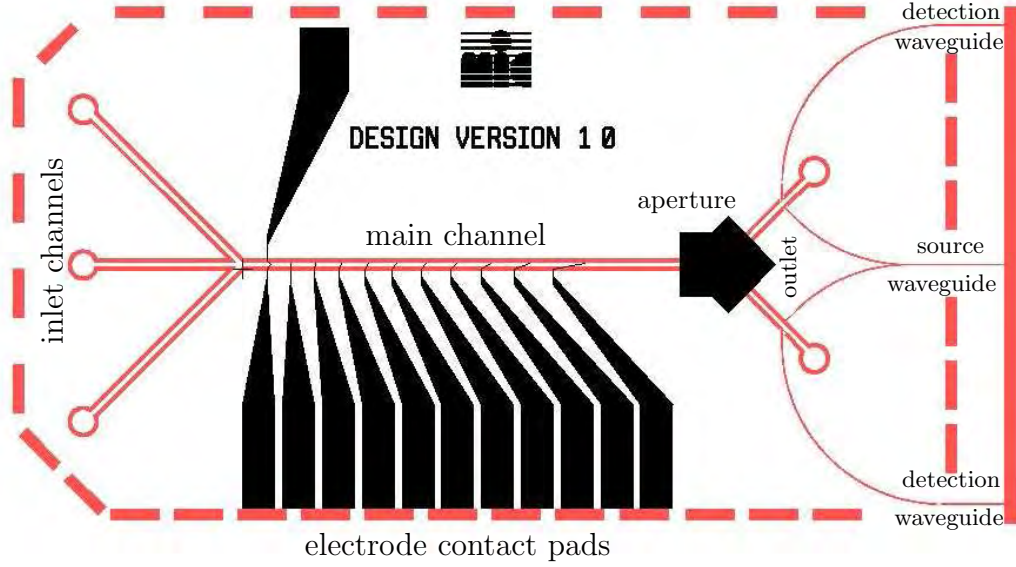
Figure 5.1: CAD drawing of the SU8-chip.

the actual device. On the bottom of the main channel we have placed a row of electrodes which make angles (starting from left) 90°, 80°, 70°, 60°, 50°, 45°, 40°, 30°, 20° and 10° with the channel wall. The width of the electrodes is 10 μm. The very first electrode structure to the left in the main channel is a focusing electrode which is intended to focus the incoming cells into a narrow line in the middle of the channel by means of negative dielectrophoresis. The metal structure located at the outlet branch is an aperture which serves to keep light from passing through the otherwise transparent bottom of the chip. Hardly visible on the figure, two tiny slits make it possible for the light (of a laser typically) to pass through the bottom in each outlet. When a cell passes above the slit, it will cause a disturbance in the light which can be sensed by a photo detector placed above the channel. Thus the structure is intended to facilitate flow cytometry in each outlet channel to keep track of the numbers of particles that go either way. The three curved polymer structures connected to the outlet channel walls are optical waveguides which constitute a micro flow cytometer. The design is inspired by Wang *et al.*, [26],[27]. The source waveguide is to be connected to a light source, the light from which is then guided to each of the outlet channels. Here it will travel across the channel and be absorbed by the fluid and the opposite channel wall. Very little light will find its way into the detection waveguide due to the angle it makes with the travelling direction of the light. However, when a particle passes the light beam, it will scatter the light and the amount of light which makes it into the detection waveguide, will change and so will the detected signal.

The channel and electrodes are surrounded by a dashed line of rod-like polymer structures. The purpose of these is to provide sufficient contact area for the lid to bond to. Filling out the entire space with polymer would of course give the largest contact area, however, this would also maximize the risk of directing the adhesive into the channels during bonding, see Sec. 5.2.1. As a compromise, we choose to fill out the space with tiny polymer rods, see Fig. 5.3. The purpose of the large beam-like polymer structure to the very right in the drawing is to prevent the wave guides from bending during dicing of the chip. The dicing track is located between the dashed polymer line and the beam, consequently the beam is not part of the final device.

5.1.2 Cleaning of wafer

Our starting point in the fabrication process is a 4" borofloat pyrex (glass) wafer of thickness 0.5 mm. The wafer is cleaned for 10 minutes in an ultra sound water bath to which 1 mL of Triton X-100 soap has been added. It is then left for 10 minutes in piranha (1:4 mixture of H_2O_2 and H_2SO_4) followed by a 10 minutes rinse in a water/N_2 bubble bath.

5.1.3 Electrode fabrication

The metal structures on the chip are fabricated using a lift-off process. A 1.5 μm thick layer of the positive photoresist [1] AZ5214E is spun on to the wafer using a spinner and the wafer is then exposed to uv-light through the electrode mask, using the aligner. The electrode mask is shown in Fig. 5.2(a). Being a positive resists, the exposed areas (i.e. not-electrode-areas) become more soluble than the non-exposed areas. However, AZ5214E can be image reversed by subjecting it to temperatures >110° C, which causes the exposed (not- electrode-) areas to become insoluble and light insensitive. After such an image reversing heat treatment, we expose the wafer to uv-light without using a mask thus making the previously unexposed (electrode-) areas soluble. The resist is then developed in AZ351B removing the soluble (electrode-) areas. The Then a 10 nm thick layer of titanium is deposited on the wafer followed by a 200 nm thick layer of gold. This is done in an e-beam evaporator. The thin layer of titanium is necessary because gold adheres poorly to AZ5214E. The fully gold covered wafer is then submerged into an acetone ultra sound bath which dissolves the soluble (not electrode-) areas of the underlying resist and gold remains only in the electrode areas. This final step is called *lift-off*. The reason we use an image-reversable positive photoresist instead of a negative photoresist, is the undercut obtained when developing AZ5214E, see Fig. 5.2(b). This undercut improves the accuracy with which the electrodes are defined.

---

[1]A photoresist is a polymer which is sensitive to ultra violet light. When heated it cross-links or polymerizes, meaning that the polymer chains bond together to a certain extent and the material cures. If the photoresist is exposed to uv-light prior to the heat treatment its cross-linking ability will be either enhanced or reduced. In the first case we are dealing with a negative resist and in the latter a positive.
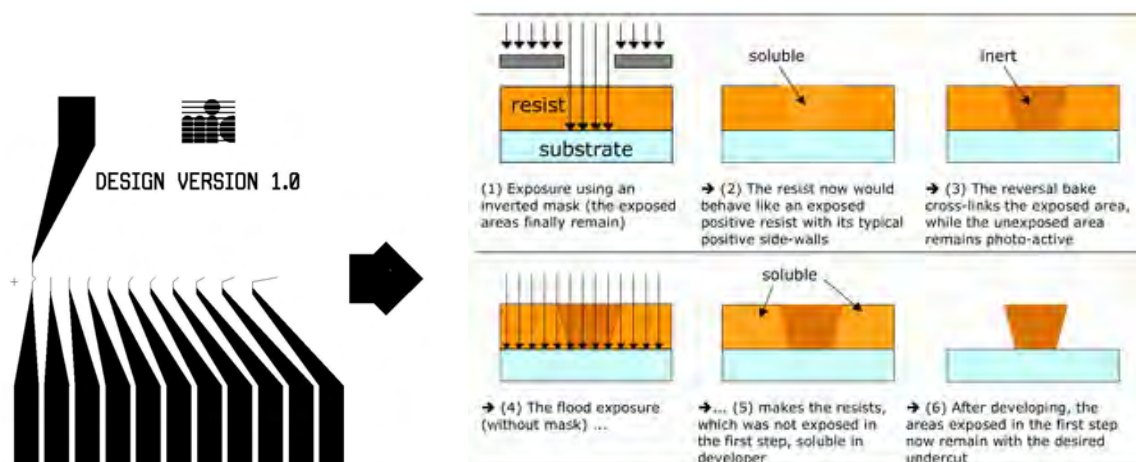
(a) The electrode mask used to define the electrodes by means of photolithography. The mask is a bright field mask, which means that the mask will be transparent in white areas and carry chrome in black areas.

(b) The use of an image-reversable positive resist for electrode definition provides sharper edges after lift-off. Source: http://www.microchemicals.de/photoresist/

Figure 5.2: Electrode mask and photo-lithographic definition.

5.1.4 Channel fabrication

Approximately 4 mL of the negative photo resist SU-8 25 is spun onto the wafer which now carries the electrodes fabricated as described in Sec. 5.1.3. The resist is soft-baked and then exposed to uv-light through the channel mask shown in Fig. 5.3. After a post-exposure bake, the wafer is submerged into the developer PGMEA for 10 minutes and rinsed in isopropanol. The completed structure is shown in Fig. 5.4. To investigate the uniformity of the channel height, five wafers of the first batch were subjected to a surface topology inspection using a profiler. Five distinct and fairly distributed areas on each wafer were scanned. The maximum deviation in height of the SU-8 structures between two wafers was 4 μm, (the height varied between 36 and 40 μm). The maximum deviation observed within one wafer was 1 μm.

5.2 Glass lid

Many different solutions have been suggested and tried when it comes to the problem of sealing a microfluidic device. PolyDiMethylSilooxane (PDMS) is a popular choice of lid material ([15],[28]) due to its morphological flexibility and adhesive properties. However, we were limited by the fact that our lid must be transparent in order for the cell sorting to be directly visible through a microscope, also the use of flow cytometry, see Sec. 5.1.1, requires a free optical path through the chip. Furthermore, our lid had to be coated with indium tin oxide to provide the top electrode. Our first choice was therefore to use a glass wafer, similar to the one used for the substrate, as a lid. The advantages of a glass
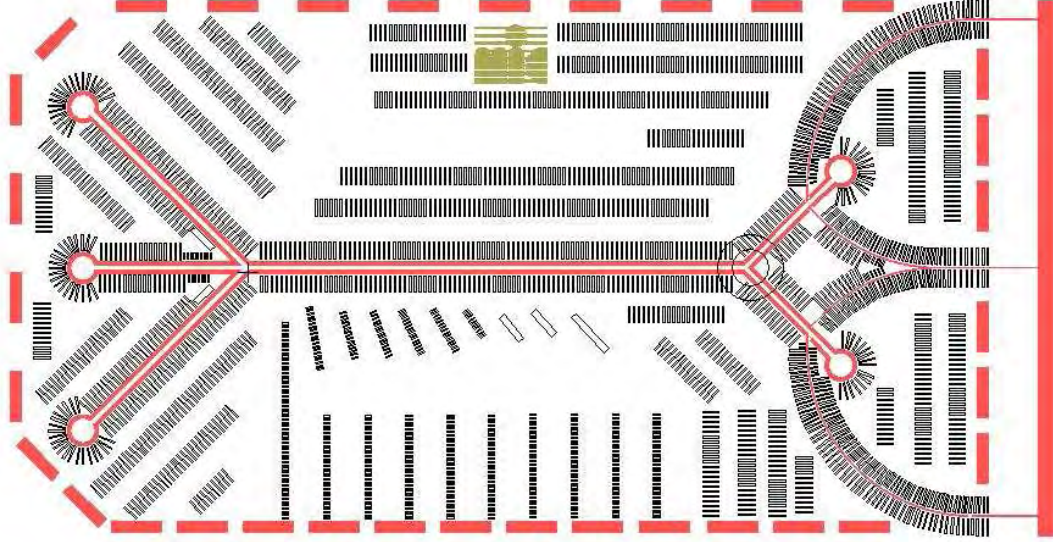
Figure 5.3: The channel mask which is used to define the SU8 structures by means of photolithography. The many small black rectangles (which were not shown in Fig. 5.1) are polymer structures serving to increase the contact area to which the lid shall bond. The channel mask is a dark field mask, so that colored areas in the mask design will be transparent on the actual mask.

lid include transparency, good heat tolerance (needed in the SU-8-bonding process) and the commercial availability of ITO-coated glass wafers. The fact that the dicing machine, which is used to separate the chips on the wafer, is capable of sawing two glass layers at a time also favors the use of a glass lid. However, the fact that glass is fragile and hard to shape are among its clear drawbacks as a lid material.

5.2.1 SU-8-bonding

A successful bonding of chip and lid is characterized by having no leakage and by its ability to withstand the general handling of the chip. The successful use of SU-8 as an adhesive between channel wall and lid has been reported in the literature [29] so our the strategy was to:

- 1. Spin coat the glass wafer lid with a thin layer of SU-8 2005 and soft-bake.

- 2. Make holes in the lid for inlets, outlets and electric contacts (outside clean room).

- 3. Press together the chip-wafer and lid-wafer while subjecting them to heat.

- 4. Expose the chip-lid sandwich to uv-light through the channel mask, see Fig. 5.3, thus causing the thin SU-8 2005 layer to cross-link exclusively in areas where it has contact to the underlying SU-8 structures.
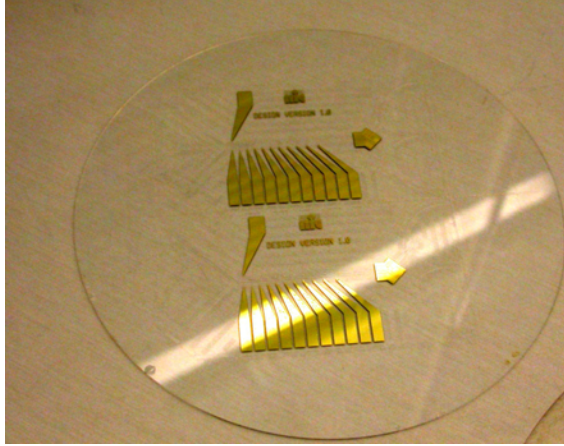
Figure 5.4: The fully processed glass wafer containing two SU8-chips. Being a mere $\sim 40\,\mu$m tall, the SU-8 structures are barely visible on the photo.

- 5. Develop the 3-dimensional structure in PGMEA inside and outside the channels.

In the following we shall comment on the above procedure, for a detailed protocol please refer to Appendix D. The first step in the procedure involves no pitfalls. Due to its low viscosity, SU-8- 2005 was chosen for the $\sim 5\,\mu$m thick adhesive layer. Then the coated wafer was soft-baked at a temperature slightly lower than the one prescribed by the SU-8 supplier[2]. This hinders the polymerization process somewhat, and the polymer therefore preserves some of its cross-linking ability. In step two, the wafer is to be brought out of the uv-light-proof cleanroom in order for the holes to be made. Therefore, we carefully wrapped the coated wafer in black light-proof tape. However, underneath the black tape we needed blue film to protect the SU-8 against strong adhesive glue of the black tape. Step two, the making of holes, is described in details in Sec. 5.2.2. Having made the holes in the wrapped wafer, we cleaned it thoroughly with water and brought it back to the clean room where the protective films were carefully removed. The lid was then placed onto the chip-wafer and this wafer-sandwich was then loaded into the chamber of a bonder, see Fig. 5.6(a). The bonder was programmed to deliver a precise and uniformly distributed force to the wafers while controlling temperature and gas pressure inside the chamber. In our program, which was inspired by the protocol used by Blanco *et al.* [30], the wafers were subjected to a force of 2500 N for 20 minutes at 100°C and 10 $^{-3}$ mbar. Our hope was then, that the channels and the adhesive layer would crosslink with each other. The bonding program lasted ~ 1 hour in total. After the completion of step 3, it turned out that the lid already bonded quite well to the chip, so the remaining steps were never carried out. To test the bonding for possible leakage or channel blocking, colored fluid was pumped and sucked through the channels. In most cases, the test revealed leakages but no blocking in the channels. Areas around the outlet and inlet holes were particularly

---

[2]Standard soft-baking temperature is 90°C. We have experimented with temperatures in the range 70-85°C.

(a) Successful SU-8-bonding
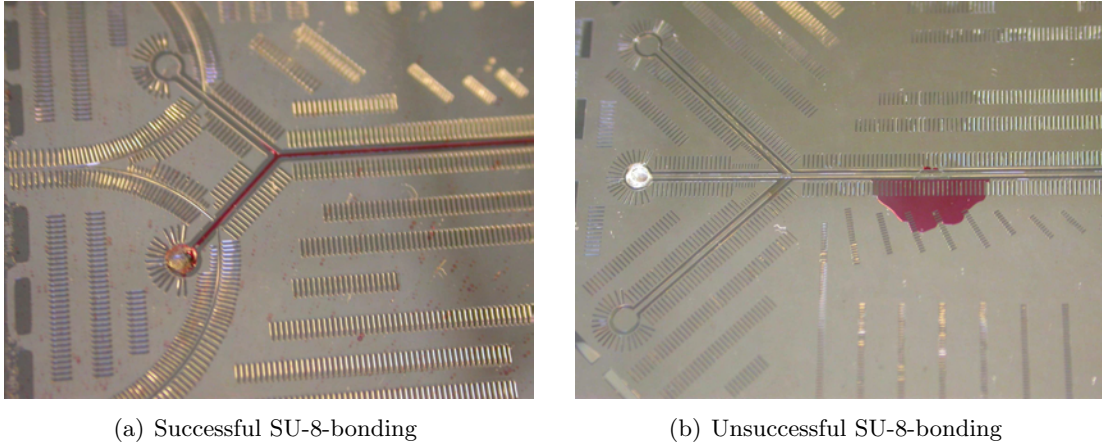
(b) Unsuccessful SU-8-bonding

Figure 5.5: Testing of the SU-8-bonding of a glass wafer to the SU-8-chip. Leakage tended to occur at inlets and outlets, however, as shown, the channel could leak midway as well. For the test chips shown here, silicon wafers were used as substrates due to their lower cost.

prone to leakage. A possible explanation to this fact is the damage caused to the SU-8 during the laser ablation patterning of the protective film, see Sec 5.2.2. Fig. 5.5 shows examples of successful and non-successful bonding.

5.2.2 Holes in glass lid

Step two in the glass lid procedure in Sec. 5.2.1 concerns the making of holes in the glass wafer which is wrapped in two layers of protective films. Two different hole making methods were employed: drilling and powder blasting. The relative location of the holes is critical since a deviation of 0.5 mm will result in leakage at inlets or outlets. Therefore, a computer controlled laser, see Fig. 5.6(b), was used to pattern the protective film, i.e. remove (by ablation) the film where the holes were to be made.

In order for the powder blasting to work properly, this patterning had to be done on both sides of the wafer, otherwise the powder would have difficulties in penetrating the wafer. For the drilling method, a pattern on one side sufficed. Double side patterning involved careful and time consuming alignment of the wafer yet was not impossible. Furthermore, successful powder blasting required both layers of film to be removed completely by the laser at the designated spots, drilling on the other hand did not, although our experience was that remains of protective film obstructed the drilling somewhat. This presented us with a dilemma: the need to remove both layers of film entirely advocates for increasing the laser power, however, the excessive heat generated during a high power ablation process will very possibly affect the SU-8 in the vicinity of the ablation spot. It may e.g. cause it to polymerize which is exactly what we have been trying to avoid by wrapping the wafer in protective film[3]. A compromise was to use low power to avoid heat

---

[3]We wished to preserve the crosslinking ability of the SU-8-layer until the time of bonding, see Sec. 5.2.1

(a) The EVG-NIL bonder which was used to facilitate the SU-8 bonding. Source: : http://www.j-ml.com/images/eq/evg520he.jpg
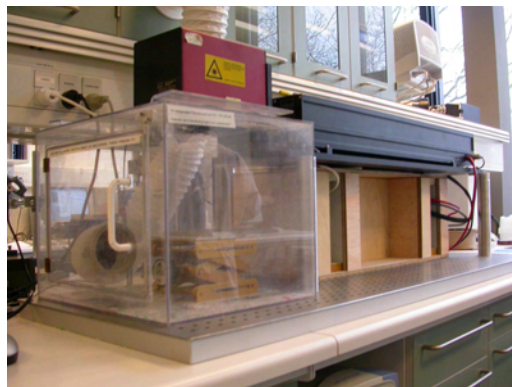
(b) The CO_2-laser was used to pattern the protective film in which the glass wafers were wrapped. Later it was used to cut channel structures in the double-sided tape as well as cutting out polymer lids used for both chip types.

Figure 5.6: Two important machines for the fabrication of the chip.

damage and in return make the laser repeat the pattern several times to make sure that both layers were removed entirely.

Once successfully patterned, the film acts as a template for the powder blaster since the powder cannot penetrate the soft polymer film. The drilling was carried out using a multi speed drill and the drill pieces were diamond coated dental drills. To keep the drill piece cool and minimize the amount of glass powder getting stuck in the holes, the wafer was kept under water during the process. Cracking wafers during drilling turned out to be a serious obstacle. The problem was evaded to some extent by replacing the drill piece every 8-10 holes and by operating at maximum speed. Powder blasting was a less brutal way of creating holes and offered a lower failure rate, yet the special alignment demands associated with this method made it a cumbersome alternative to drilling. Also we suspected that the powder blasting introduced radial cracks in the material causing it to crack easier as described in [31]. Either way, if all holes were actually made without damaging the wafer, pealing off the two layers of film on each side without breaking the awfully fragile wafer proved to be just as challenging as the actual making of the holes. As a result, the number of wafers surviving step 2 in the glass lid procedure was unacceptably low.

As an attempt to avoid the cracking of wafers, we tried to swap step two and three so that the holes were drilled *after* the lid had been bonded to the chip. This approach eliminated the need for laser patterning and hence the time consuming alignment and risk of damaging the SU-8, however it also turned out to introduce glass powder into the channels during drilling, which caused them to clog. Having spent an amount of time

| (a) A roll of PET-A. | (b) PMMA sheets. |

Figure 5.7: The two types of polymer used in this project. The PMMA sheets measure 10×10 cm^2 and have a thickness of 1.5 mm. The blue color is due to the protective film in which they are wrapped. The Pet-A shown has a thickness of 0.2 mm.

with all three approaches, which allowed us to exclude the lack of sufficient dexterity as a reasonable explanation to the high rate of failure, we decided to explore alternative ways of making lids.

5.3 Polymer lid

Compared to glass, polymer is in general rather easy to process, it is durable and inexpensive. In this project we have used the very common polymers Polymethylmethacrylate (PMMA) and polyethylene teraphthalate (PET), see Fig. 5.7. The PMMA sheets we have used are 1 mm thick and have a transparency which matches that of the glass wafers. For PMMA the glass transition temperature is $T_g \approx 105°$C, for PET, T_g is $\sim 69°$C. The transparency of PET is poorer and we have used samples of thicknesses 0.2 mm and 0.75 mm. ITO-coated PET-sheets of thickness 0.2 mm are commercially available, however to our knowledge, no such thing exists for PMMA. Instead one may buy an ITO suspension which can be "painted" on the polymer and thus provide a home-made coating. The latter approach is a recently developed method, and consequently there is little evidence for its applicability. Finally, a third approach is to buy an ITO crucible in order to deposit the material by means of sputtering. Of these three, the pre-coated PET-sheets represent the easiest and most expensive choice.

5.3.1 Design

The processing of the polymer lid is done entirely using the CO$_2$-laser. Combined with the low cost of polymers, this makes the design process much more fast and flexible than it was the case for the glass lid.

5.3.2   Bonding

Two bonding methods have been investigated for polymer lids, SU-8 bonding and gluing using two different types of adhesive material. Applying the SU-8 bonding procedure to a polymer wafer had not been tried before and turned out to present us with a number of hurdles.

In order to spin SU-8 on the polymer, we needed a circular geometry and therefore used the laser to cut the polymer into circular wafers. However, the spinner cannot handle 0.2 mm thick PET-wafers since they are too floppy. To gain sufficient rigidity, we had to glue the thin ITO-coated PET-wafer to a thicker PET- wafer. To spread the glue evenly, we used a spinner (outside the cleanroom), and we experimented with three types of commercial cyanoacetate adhesives, various different recipes for home-made glue and finally the solvent acetone. The key challenge was to find an adhesive with the right viscosity allowing a thin and uniform layer to be spun onto wafer. Another important challenge was to minimize the loss in transparency resulting from the adhesives' tendency to turn milky when curing.

Hence, having glued together a thin and thick PET wafer and coated this composite wafer with SU-8 2005, the next problem was the soft-baking, which takes place at 70-90°C. This just exceeds the glass temperature of PET, and as a result, the thick PET-wafers crumbled when they were soft-baked. However, using a PMMA-wafer for support instead circumvented this problem.

After having been soft-baked, the wafer was wrapped in light-proof film before taking it out of the cleanroom as was with the glass lid. Cutting out the lid of the polymer wafer with the laser was no problem. However, during removal of the protective films, we noticed that the SU-8 seemed to stick to the film rather than the wafer leaving the wafer only partially coated. This suspicion was reinforced by the fact that SU-8 bonding between chip and polymer lid was very poor. It did not even last long enough for us to do a leakage test. After a number of failed bonding attempts, SU-8 bonding of polymer lids seemed to be the wrong approach.

Successful use of the commercial glue Loctite® as an adhesive between the SU-8 structure and ITO-coated polymer lid has been reported by Hunt *et al.* [32] and this approach was therefore tried and the results certainly seemed more promising than SU-8-bonding, yet no true breakthrough has been achieved. Also, uv-glue has been tested as an adhesive. Fig. 5.8 shows two micrographs of a SU-8-chip with a polymer lid uv-glued to it.

5.4   DST-chip

The massive bonding problems associated with the SU-8 chip forced us to think untraditionally. Instead of using SU-8 as the building material for the channel walls other materials had to be considered. Zhou [33] reports successful use of polytetrafluoroethy-
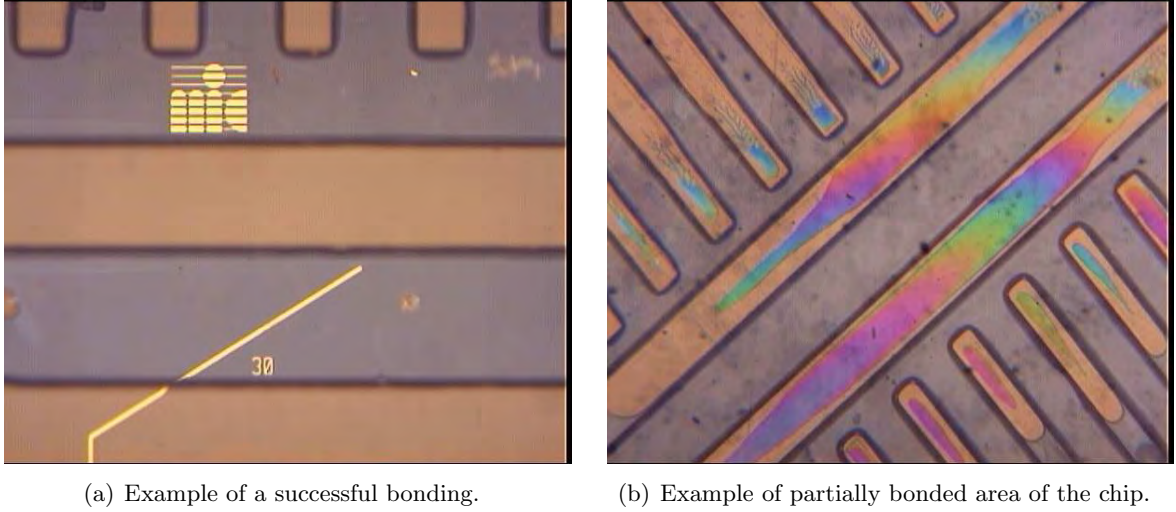
(a) Example of a successful bonding.

(b) Example of partially bonded area of the chip.

Figure 5.8: UV-glue as the adhesive material between chip and lid is perhaps the way to a reliable bonding. The brownish color of the polymer indicates perfect bonding, (a) shows an example of this. The rainbow colored pattern appearing on the polymer structure in (b) is known as *Newton rings*, and it indicates that the bonding is only partial. Pictures are curtesy of Troels Balmer Christensen, MIC, DTU.

lene (PTFE) as channel wall material with ITO covered glass lids and Wu [28] does the same for PDMS. However, due to time limitations and our access to the CO_2-laser we decided to experiment with double-sided tape (DST). DST consists of a polymer base film coated with adhesive material on both sides. In our case, the polymer was PET and the adhesive was acrylic. The idea was now to define the channels directly into the DST by means of laser ablation. Fig. (5.9) shows an example of such a design realized. This design differs from the SU-8 design by lacking the waveguides and by having a larger contact area for the lid since the contact area is the entire chip except for the channels.

5.4.1 Electrode fabrication

Electrodes for the DST-chip are made in the exact same way as for the SU-8-chip, please refer to Sec. 5.1.3.

5.4.2 Channel fabrication

A piece of DST, the area of which is a bit larger than that of the chip is cut out, and a piece of protective film is placed on its sticky side so that the piece is smooth on both sides. The piece is then placed on the metal chuck beneath the CO_2-laser aperture, see Fig. (5.6(b)), and the channel pattern is created by laser ablation. Some adjustments of the laser parameters were necessary in order to optimize the channel wall smoothness, the lack of which turned out to be one of the most serious shortcomings of this fabrication approach. Once the channel structure has been created, the channel pattern is to transferred to the chip. This is the most critical step in the fabrication process, because the functionality of the chip relies on the precise alignment of channel walls with the electrodes. Therefore,
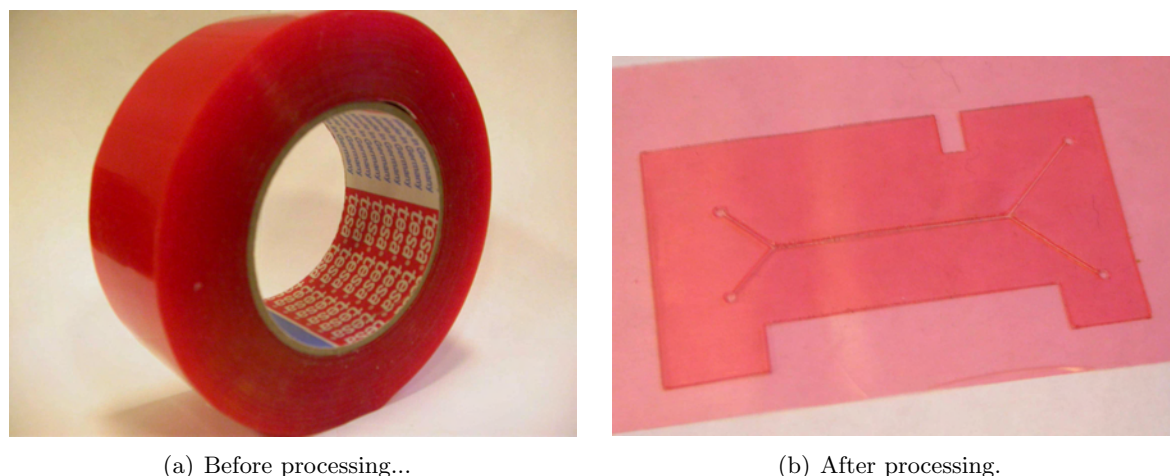
(a) Before processing...   (b) After processing.

Figure 5.9: A roll of the double-sided adhesive tape used to fabricate the channel structure.

prior to transfer, a ink marker is used to indicate the positions of the individual electrodes which are barely visible to the naked eye. The marking is done under a microscope. The resulting line of dots can then be used as alignment marks when the channel structure is transferred manually to the chip.

5.4.3   Polymer lid

Using DST as the channel material we had eliminated the need for extra adhesives for the bonding of the lid. We simply cut out the lid directly from the pre-made ITO-coated PET-sheets and placed it manually on the DST-chip. Alignment of lid and chip could be done manually if appropriate care was exercised. The completed DST-chip including lid is shown in Fig. 5.10(b).

5.5   Summary of chapter 5.

A microchip consisting of a main channel to the ends of which three inlet and two outlet channels are connected has been designed. The main channel features 2 focusing and 10 guiding electrodes, and the outlet channels are equipped with polymer waveguides for the purpose of flow cytometry. Using glass for the substrate, gold for the electrodes and SU-8 for the polymer channel walls, the chip has been fabricated in the cleanroom by means of standard techniques of metal depositing, photolithography and lift-off. A glass lid has been successfully attached to the chip by means of a home made SU-8 bonding protocol. However, due to the cumbersome and not very beneficial out-of-cleanroom procedure of making in- and outlet holes in the glass lid, glass has been discarded as lid material. The polymer PET-A has been tried as an alternative lid material but has been found unqualified due to its glass transition temperature which is below the SU-8 processing temperature. Another polymer, PMMA, has proven able to endure the entire SU-8 process including bonding,
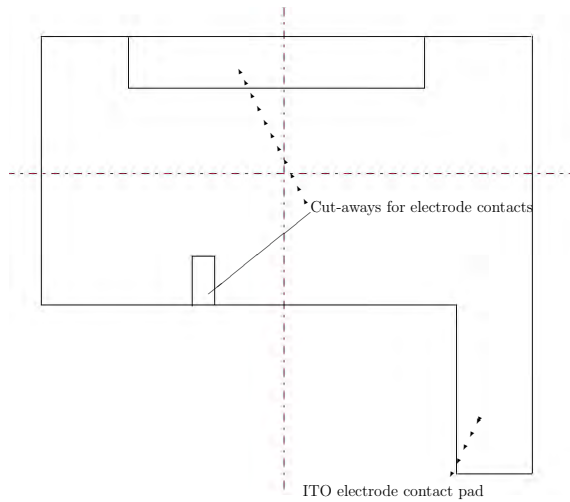
(a) CAD drawing of the ITO-lid.
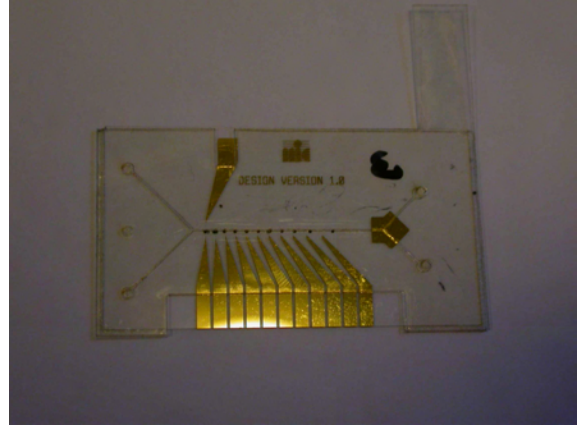
(b) The DST-chip with a ITO-coated PET lid. Note the black ink dots alongside the main channel. They are located on the backside of the chip and serve to facilitate the manual alignment of channel and electrodes. The flab in the top right corner provides external electrical contact to the ITO electrode.

Figure 5.10: ITO-lid design and DST-chip.

yet this material does not adhere well enough to SU-8. Also, PMMA with an ITO (indium tin oxide)-coated sheet of PET glued to it has been attempted bonded to the chip with the same unsatisfactory result. Finally, commercial as well as home-made glues have been tested as adhesive materials between lid and chip however with limited success.

As an alternative solution, the SU-8 channels have been replaced by a piece of double-sided tape into which the channels have been created by means of laser ablation. The piece of tape containing the channels has then been transferred manually onto the glass substrate carrying the gold electrodes. ITO-coated PET-sheets have been cut out using the laser and used as lid. While this fabrication method offers less control of design on the micrometer scale, it is faster and more flexible. In addition, the chips can be reused since the tape can be removed by acetone.

Chapter 6

Experiments

6.1 The chip holder

To provide a handy and robust interface to the chip during experiments, a chip holder has been designed and constructed, see Fig. 6.1(a). The holder is basically two slabs of polymer between which the chip is sandwiched. While the bottom slab serves as solid support, the top piece features the five fluidic and 12 electric interconnections. Rubber O-rings provide leakage free connection to the chip while the mini-stac tappings allow mounting of standard microfluidic tubes as shown on the photo. The electric connections are facilitated by spring loaded metal probes. The center of both bottom and top slab has been removed to ensure optimal visual access to the main channel of the chip from either direction. Please refer to Appendix F for the detailed design of the chip holder.

6.2 Fluidic performance

First of all, we wished to examine the behavior of the double sided tape when exposed to water. We feared that the chip would leak or that the tape would absorb water and swell. By pumping water manually through the chip at great speed we verified that the chip and chip holder were practically water-tight.

Having verified this crucial property of the chip we built an experimental setup in the laboratory shown schematically in Fig. 6.2(a) and photographically in Fig. 6.2(b). We then wished to investigate whether a two phase flow could be established in the main channel in spite of the irregularity and roughness of the tape channel walls. A well-defined two phase flow is absolutely critical in order for the sorting principle to work. One pump was loaded with plain water, the other with a solution of phenol red (phenolsulfonphtalein) to give color. It turned out, that a fairly well-defined two-phase flow was established when the pumps operated at the same flow. Fig. 6.3(a) shows a micrographs of the result. However, the roughness of the channel walls did seem to promote the formation of bubbles and cause them get stuck in the channel, see Fig. 6.3(b). Trapped bubbles will distort the flow profile and may even block the channel completely if they are large enough.
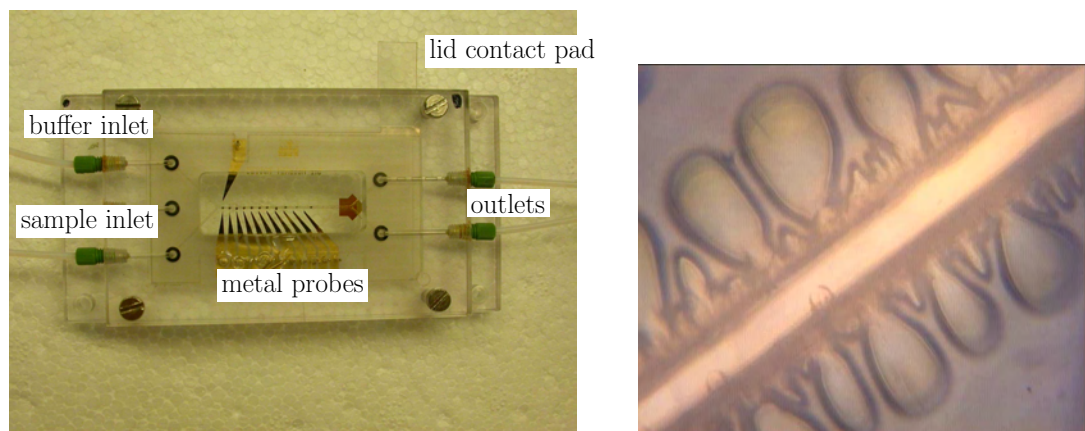
(a) he chip holder provides a handy interface between the chip and laboratory. This design was inspired by an earlier chip holder design by Anders Brask.

(b) After a few hours of constant use, the double-sided tape channel walls had absorbed a considerable amount of water.

Figure 6.1: Chip holder and swollen channel walls.

After a few hours of constant exposure to water, it was noticed that the tape began to absorb water at the edges which caused the channel walls to swell and the channel to narrow. Fig. 6.1(b) shows an evidence of this.

6.3   Cell manipulation

Having tested and verified the fluidic functionality of the DST-chip in Sec. 6.2, we progressed to test the ability of the chip to manipulate biological particles.

6.3.1   Cell preparation

Yeast cells (*Saccharomyces cerevisiae*) were chosen as test material because they are readily available, inexpensive and well-studied. In order to make the cells visible in the microscope, they were labelled with the molecule FITC (fluorescein 5-isothiocyanate) which is fluorescent at 632.8 nm (Please refer to reference [34] for the detailed cell preparation protocol). The labelled cells were suspended in MilliQ water to which a bit of KCl was added in order to achieve a conductivity of $1.9 \cdot 10^{-2}$ S m^{-1}. This was done partly because negative dielectrophoresis has been observed previously [15] at medium conductivities of this order and partly because the conductivity of a real biological sample would be higher than that of MilliQ-water [1].

6.3.2   Cell guiding

The sample pump, c.f. Fig. 6.2(a), was loaded with the yeast suspension, prepared as described in Sec. 6.3.1, while the buffer pump was loaded with deionized water to which KCl

---

[1]The conductivity of blood is approximately 0.61 S m^{-1}.

(a) Schematic of the experimental setup.
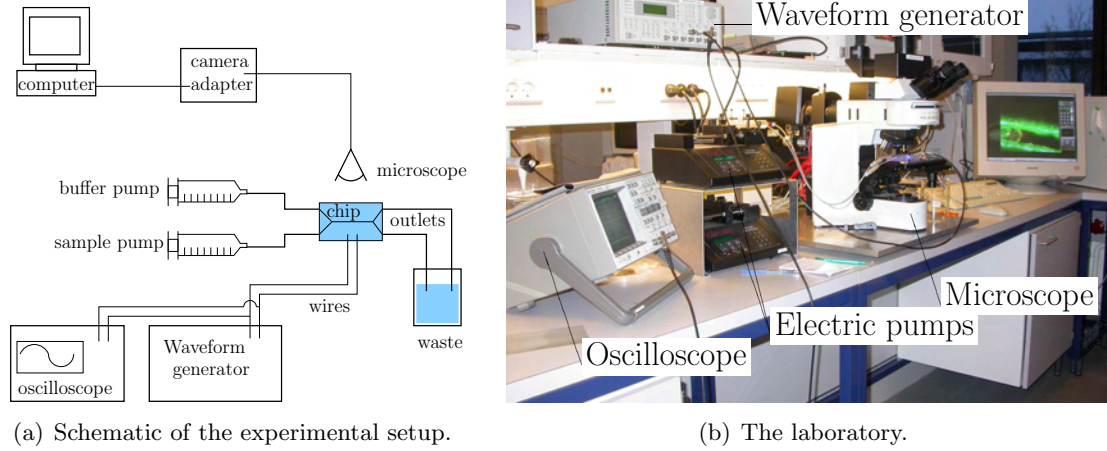
(b) The laboratory.

Figure 6.2: Experimental setup.

had been added in order to achieve the same conductivity as that of the cell suspension. The flow rate was varied between 0.5 μL min^{-1} and 100 μL min^{-1}, 1 μL min^{-1} being the typical value.

Our first observation was that a steady two-phase flow, like the one in shown in Fig. 6.3(a), was difficult to establish with the yeast cells. At the merge of the inlets, the two phase flow existed, see Fig. 6.4(a), however the roughness of the channel walls distorted the flow so badly that already at the 80°-electrode, the two phases were hard to distinguish. Also, the flow exhibited a pulsing behavior oscillating between practically zero flow velocity one moment and very high velocities the next. This effect can probably also be imputed to the channel roughness, which partially clogs the channel causing pressure to build up until a point when it reaches a magnitude sufficient to break through the clog. Increasing the flow rates of both pumps or alternatively just the buffer pump to 100 μL min^{-1} did stabilize the flow to a certain extent, but still the phases mixed too much to allow sorting of any kind. However, this did not prevent us from investigating the cell guiding ability of the chip. Table 6.1 summarizes our observations. In Table 6.1, Q is the flow rate per unit channel width, and $\theta^\star$ is the critical angle below which all cells should be guided according to our model. The critical angle is calculated on basis of γ, the values of which are listed in the table, and $\chi = d/h$ which is 0.125 for all experiments.

First of all, it is interesting to note the dielectric behavior of the cells at different frequencies. Negative dielectrophoresis could only be established for frequencies ≤5 kHz. After a few hours of experimenting, we were only able to generate positive dielectrophoresis even at frequencies as low as 1 kHz. We assumed that the cells had died and their conductivities changed accordingly. Measuring the conductivity of the sample after finishing the experiment, we found that it had risen from the initial $1.9 \cdot 10^{-2}$ S m^{-1} to $4.2 \cdot 10^{-2}$ S m^{-1}. These observation should be held against the theoretical predictions of the shell model, introduced in Sec. 4.8.2. Using data for ϵ, σ and shell radii taken from the literature [1],

(a) Two-phase flow at the 45°-electrode.   (b) Two bubbles distort the flow interface.
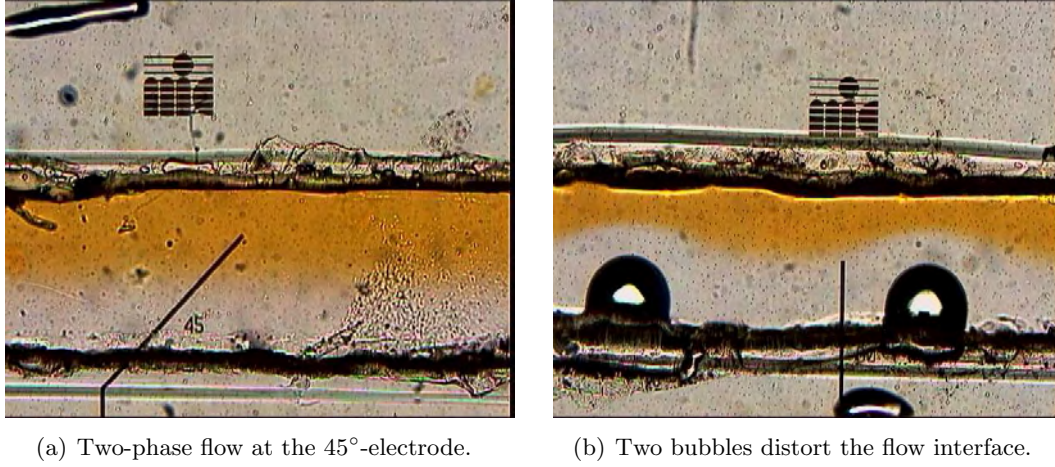
Figure 6.3: In spite of the irregular channel walls resulting from laser ablation of the double sided tape, a fairly well-defined two phase flow is established in the main channel.

we use a 2-shell model to calculate the spectrum of the Claussius-Mossotti factor $K(\omega)$ for viable and non-viable yeast. The result is shown in Fig. 6.5. Although the data on which Fig. 6.5 has been obtained at different medium conductivities, the spectrum is still in good agreement with our observations. In accordance with our observations, non-viable yeast exhibits pDEP for all frequencies within our range. Our frequency range was upwardly limited by the maximum capability of the generator (16 MHz), and at frequencies below 1 KHz, the rapid formation of hydrogen bubbles at the electrodes due to the electrolysis of water made it impossible to observe the behavior of the cells in the vicinity of the electrodes. Fig. 6.6 conveys evidence of electrolysis as well as a record of both nDEP and pDEP.

Although we lack quantitative data on the guiding efficiency of the chip in our experiments, it is still interesting to compare predictions of our theory with the observations in Table 6.1. As to theory, our model predicts the phase diagrams shown in Fig 6.7 which are based on the values of γ and χ by which each nDEP-experiment is characterized. Also, the model predicts the critical angles $\theta^\star$ listed in the rightmost column of Table 6.1. As to the experimental results, we turn to Table 6.1 and note that in experiments 1 and 3, the electrode angles θ are comparable and exceed the critical angle $\theta^\star$, respectively, therefore one would expect all or practically all cells to be guided by the electrodes. In the meantime, we observed that roughly 50% of the cells escaped the DEP-force of the electrode. This discrepancy may have several explanations. First of all, there is some uncertainty associated with the value of Q, the flow rate Q_{vol} per channel width, w. This owes to the uncertainty in our knowledge of both of these parameters. The channel width is hard to control precisely with the laser, and in addition, the channel structure is likely to be stretched or compressed when it is transferred to the chip. The flow rate Q_{vol} on the other hand, is fixed with adequate precision on the pump, however the pulsing behavior of the flow described earlier in this section brings about considerable variation in the flow rate
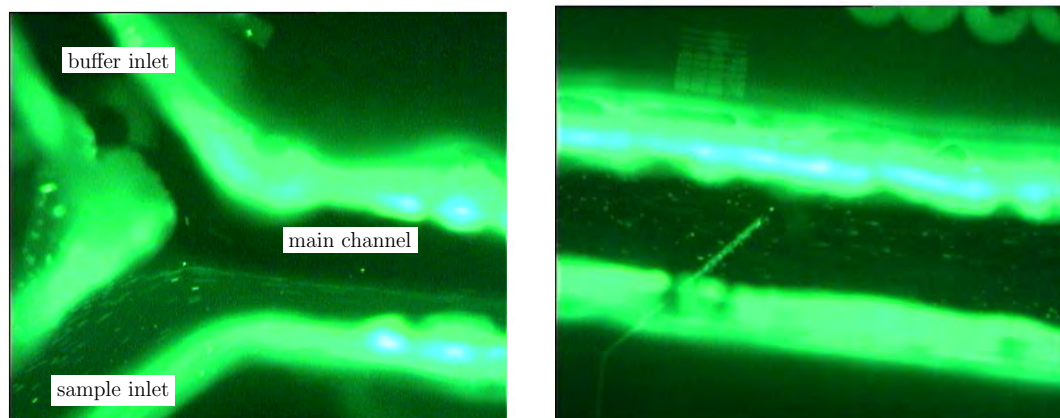
(a) Two-phase flow at the merge of the inlet channels. The intense coloring of the channel wall is caused by the auto-fluorescence of the polymer.

(b) Further downstream the two phases have ceased to exist.

Figure 6.4: Failing to establish a stable two-phase flow during the biological sample experiments.

over time. Secondly, the listed fraction of cells which is guided is based on a mere visual estimate obtained from a video recording of the experiment. Needless to say, this method of observation involves quite a bit of ambiguity. Finally, generally speaking, even though most of the channel's vertical extent is within the guiding zone for a given value of θ, see Fig. 6.7, the part that is not is situated in the fast flowing region of the channel and hence the number of cells escaping the electrode in a given time span will seem disproportionately high, when compared to the extent of the non-guiding section. To correct for this, one could assume a given distribution of cells along the vertical channel dimension and combine this with the velocity profile of the fluid to give a theoretical estimate of the fraction of escaping cells, however the amount of uncertainty associated with the available data, makes it futile to process it any further. In experiment 2, the chip performs better than expected from theory. However, in this experiment, the recording shows clear evidence of an oscillating flow rate, and we may therefore assume that the true flow rate is below the tabulated 1μL min^{-1}. We shall conclude this section by stating that experiment 6 is in good agreement with the theoretical expectations keeping in mind the uncertainty factor.

	Experimental parameters				Calculated parameters		
Exp. no.	Flow rate Q_{vol} [μL min^{-1}]	f [Hz]	θ	Observation	Q [m^2 s^{-1}]	γ	$\theta^\star$
1	0.5	$1 \cdot 10^3$	45°	App. 50% of the cells were guided by nDEP	$2.77 \cdot 10^{-8}$	3.9	41°
2	1	$1 \cdot 10^3$	40°	Majority of cells were guided by nDEP	$5.54 \cdot 10^{-8}$	1.9	19°
3	1	$5 \cdot 10^3$	10°	App. 50% of the cells were guided by nDEP	$5.54 \cdot 10^{-8}$	1.9	19°
4	1	$10 \cdot 10^6$	45°	App. 50% the cells were caught by pDEP	$5.54 \cdot 10^{-8}$	1.9	19°
5	1	$16 \cdot 10^6$	10°	App. half the cells were caught by pDEP	$5.54 \cdot 10^{-8}$	0.48	–
6	5	$1 \cdot 10^3$	10°	App. 50% the cells were guided by nDEP	$2.77 \cdot 10^{-7}$	0.38	4°
7	10	$10 \cdot 10^6$	70°	pDEP	$5.54 \cdot 10^{-7}$	0.19	–
8	10	$10 \cdot 10^6$	90°	pDEP	$5.54 \cdot 10^{-7}$	0.19	–

Table 6.1: Experimental results. The experiments were conducted at medium conductivies $\sigma_m = 1.9 \cdot 10^{-2}$ S m^{-1}. In all cases $V = 20$ V, the cell radius $a \sim 3.5$ μm, the channel height $h = 80$ μm, the electrode width $d = 10$ μm, medium permittivity $\epsilon_m = 78\epsilon_0$ and the width of the channel was ~ 300 μm. This gives $\chi = 0.125$ for all experiements. Note that in experiment 5 $V = 10$ V, hence the lower value of γ.

6.4   Summary of chapter 6

It has been verified that both DST-chip and chip holder constitute a water-tight fluidic system in which a two-phase flow can be realized but not necessarily reproduced. The latter fact owes to irregularity of the channel walls which distort the flow and destroy the phase boundary. The breakdown of the phase boundary renders the chip incapable of sorting cells, since this ability relies on the existence of a two-phase flow. The irreproducibility of the DST-chip is the result of the insufficient precision in the channel fabrication which is based on laser ablation as well as the manual transfer of the tape to the chip. It has been observed that the chip absorbs slowly absorbs water which causes the channel walls to swell. The chip thus has a working lifetime of 2-3 hours. Despite these shortcomings, the chip has proven capable of guiding viable yeast cells using negative dielectrophoresis. The dielectric behavior of the yeast cells has been examined for various frequencies within the range 1 kHz-16 MHz and all observations are in agreement with the predictions of the spherical two-shell cell model. Quantitative data on the guided fraction of cells has not been obtained due to design related limitation associated with the DST-chip, however
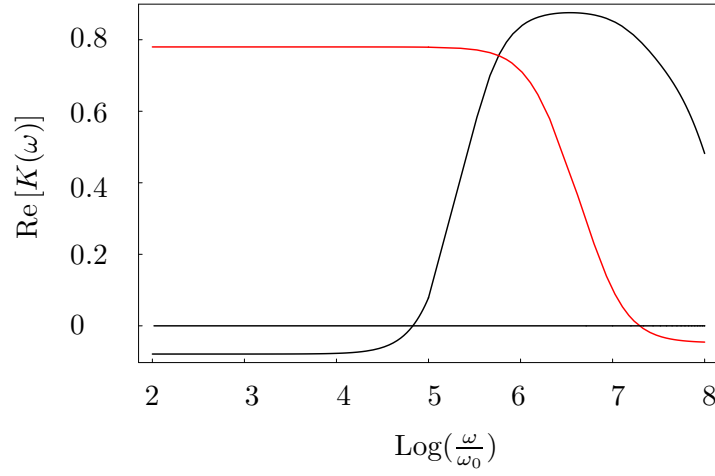
Figure 6.5: The frequency dependence of the Claussius-Mossotti factor for viable (black) and non-viable (red) yeast cells as predicted by a spherical two shell model based on the parameters taken from literature [1]. The cell conductivity data was obtained at medium conductivities $\sigma_{m_{\text{viable}}} = 3 \cdot 10^{-3}$ S m^{-1}, $\sigma_{m_{\text{non-viable}}} = 5 \cdot 10^{-4}$ S m^{-1}.

most observed phenomena can be explained qualitatively by theory.
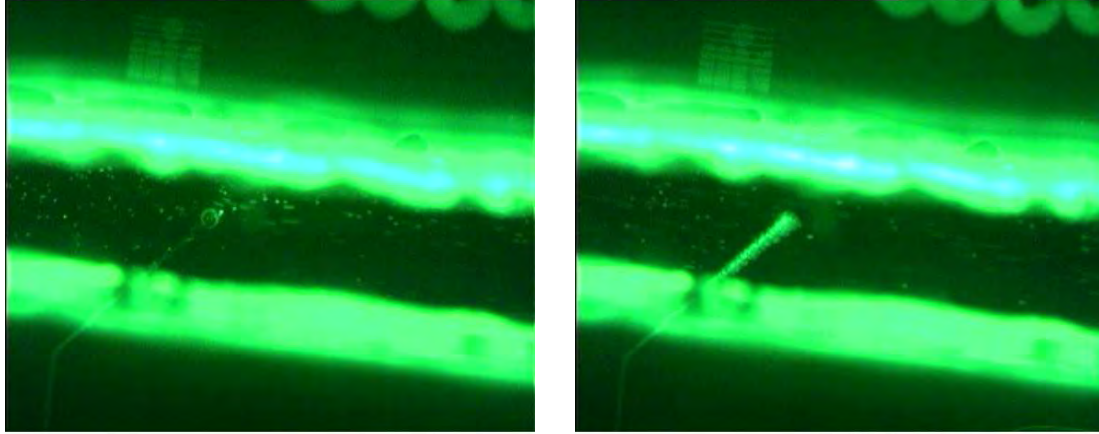
(a) Negative dielectrophoresis observed in experiment no. 1 in Table 6.1. Note the hydrogen bubble formed at the tip of the electrode due to the electrolysis of water.

(b) Positive dieletrophoresis observed experiment no. 4 in Table 6.1.

Figure 6.6: Dielectrophoresis at two different frequencies.

(a) Experiment 1.
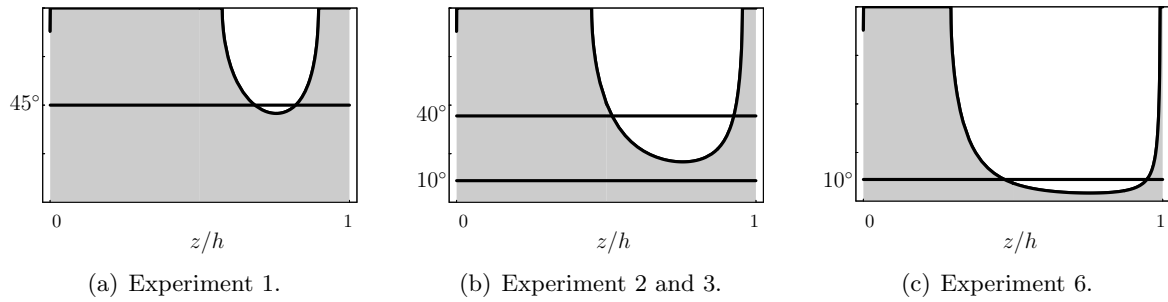
(b) Experiment 2 and 3.

(c) Experiment 6.

Figure 6.7: Phasediagrams for the nDEP-experiments listed in Table 6.1. In experiment 3, the electrode angle is $10°$ which is below the critical angle for this value of γ and we expect guidance of all cells. The same is almost true for experiment 1.

Chapter 7

Summary and outlook

The theoretical work presented in this thesis has primarily resulted in analytical solutions to the dielectrophoretic force fields of three different cell guiding electro-fluidic devices. Each device has been modelled in two ways of differing complexity which has given rise to two different solutions the key features of which are the same. In the process, a handy mathematical solution formula based on Fourier transforms has been developed. The formula expresses on closed form the solutions to linear Dirichlet problems defined on infinite strip domains. The obtained field solutions have been combined with basic hydrodynamic solutions to the flow in a microchannel to form a theoretical model the object of which is to predict whether or not a cell will be guided by the dielectrophoretic force for a given set of parameter values, which are easily obtained. The model has been applied to the three devices and thus provided insight of the dynamics of continuous cell guiding using negative dielectrophoresis. In particular, for the electrode angle, which is the angle between the guiding electrode and the flow direction, the model predicts a critical value below which all cells are guided.

On the practical part, a microfluidic test device corresponding to one of the theoretically treated designs has been produced and subjected to preliminary tests in the laboratory. The device has glass as its base substrate and carries gold electrodes. The original plan was to define the channel structures in the cleanroom using the photoresist SU-8, however providing such a device with a lid has proven to be a serious obstacle. While glass lids bond quite well to the SU-8 channel walls they are too fragile, when it comes to making inlet and outlet holes. The opposite is true for polymer lids. For the glass lids, both drilling and powder blasting have been employed in an attempt to produce the holes in a gentle manner. For the polymer lids, different polymers as well as a wide range of different adhesives has been tested without success.

SU-8 has therefore been abandoned as a channel material in favor of double-sided tape. In the double-sided tape approach, the channels have been cut into the tape using a computer controlled laser, and the patterned piece of tape has been manually transferred to the glass substrate carrying the electrodes. An indium tin oxide coated polymer sheet is used as a lid. Though this fabrication method lacks precision in channel definition and

involves alignment problems, it is faster and more flexible than its SU-8 counterpart.

One series of experiments has been conducted with the double-sided tape device. The device is water-tight and has an effective lifetime of 2-3 hours. Successful guiding of yeast cells using negative dielectrophoresis has been observed although cell sorting has not been achieved. The reason for this is the irregularity of the channel walls caused by the laser ablation. Because the double-sided tape chip lacks the flow cytometer feature, which was part of the original SU-8 design, quantitative data on cell guiding has not been obtained for the device. Consequently, comparison of theoretical predictions and empirical observations has not been performed.

Future challenges within the field of research treated by this thesis include the development of a reliable SU-8 bonding protocol for polymers and alternative methods of producing regular channel structures in adhesive tapes. Also, it would be interesting to experiment with protocols for the recently commercialized indium tin oxide emulsion which can be painted on potentially any material. Such a protocol would provide an extended freedom of choice when it comes to lid material.

Theoretically, it would be interesting to expand the cell guiding model so as to take into account the vertical component of the dielectrophoretic force field. During the experiments, this component was seen to play a significant role for the cell trajectories. Calculations of the dielectrophoretic force could be refined by taking into account the finite size of the cells and by setting up more refined boundary conditions for the potential than it has been done in this thesis.

Appendix A

Verification of potential solution in Sec.4.4.2

We shall here check that $\phi_{1,\Theta}$ satisfies the boundary conditions. We do this using an alternative expression for $\phi_{1,\Theta}$ which can be shown to be equivalent with Eq. (4.23). If we let $d \to 0^+$ while $V \to \infty$ so that $Vd = A$ remains constant we should recover the

δ-solution from Section 4.4.1. We get:

$$
\begin{aligned}
\lim_{d\to 0^+} \phi &= \lim_{d\to 0^+} \frac{iA\Theta(\frac{d}{2})}{2\pi d}\left[\ln\left(-\frac{e^{\frac{\pi}{h}x}+e^{i\frac{\pi}{h}z}}{e^{\frac{\pi}{h}x}+e^{-i\frac{\pi}{h}z}}\right) + \ln\left(-\frac{1+e^{\frac{\pi}{h}(x+iz)}}{1+e^{\frac{\pi}{h}(x-iz)}}\right) + \right.\\
&\qquad\left. \ln\left(-\frac{e^{\frac{\pi}{h}d/2}+e^{\frac{\pi}{h}(x-iz)}}{e^{\frac{\pi}{h}d/2}+e^{\frac{\pi}{h}(x+iz)}}\right) + \ln\left(-\frac{e^{\frac{\pi}{h}(d/2+x)}+e^{-i\frac{\pi}{h}z}}{e^{\frac{\pi}{h}(d/2+x)}+e^{i\frac{\pi}{h}z}}\right)\right]\\
&= \lim_{d\to 0^+} \frac{iA\Theta(\frac{d}{2})}{2\pi d}\, ln\left(\frac{\left(e^{\frac{\pi}{h}x}+e^{i\frac{\pi}{h}z}\right)\left(1+e^{\frac{\pi}{h}(x+iz)}\right)\left(e^{\frac{\pi}{h}d/2}+e^{\frac{\pi}{h}(x-iz)}\right)\left(e^{\frac{\pi}{h}(d/2+x)}+e^{-i\frac{\pi}{h}z}\right)}{\left(e^{\frac{\pi}{h}x}+e^{-i\frac{\pi}{h}z}\right)\left(1+e^{\frac{\pi}{h}(x-iz)}\right)\left(e^{\frac{\pi}{h}d/2}+e^{\frac{\pi}{h}(x+iz)}\right)\left(e^{\frac{\pi}{h}(d/2+x)}+e^{i\frac{\pi}{h}z}\right)}\right)\\
&= \lim_{d\to 0^+} \frac{iA\Theta(\frac{w}{2})}{2\pi d}\, ln\left(\frac{\left(e^{\frac{\pi}{h}x}+e^{i\frac{\pi}{h}z}\right)\left(1+e^{\frac{\pi}{h}(x+iz)}\right)\left(e^{\frac{\pi}{h}d/2}+e^{\frac{\pi}{h}(x-iz)}\right)\left(e^{\frac{\pi}{h}(d/2+x)}+e^{-i\frac{\pi}{h}z}\right)}{\left(e^{\frac{\pi}{h}(d/2+x)}+e^{i\frac{\pi}{h}z}\right)\left(e^{\frac{\pi}{h}d/2}+e^{\frac{\pi}{h}(x+iz)}\right)\left(1+e^{\frac{\pi}{h}(x-iz)}\right)\left(e^{\frac{\pi}{h}x}+e^{-i\frac{\pi}{h}z}\right)}\right)\\
&= \lim_{d\to 0^+} \frac{iA\Theta(\frac{d}{2})}{2\pi d}\left[ln\left(\frac{\left(e^{\frac{\pi}{h}x}+e^{i\frac{\pi}{h}z}\right)}{\left(e^{\frac{\pi}{h}(d/2+x)}+e^{i\frac{\pi}{h}z}\right)}\right) + \ln\left(\frac{\left(1+e^{\frac{\pi}{h}(x+iz)}\right)}{\left(e^{\frac{\pi}{h}d/2}+e^{\frac{\pi}{h}(x+iz)}\right)}\right) + \right.\\
&\qquad\left. \ln\left(\frac{\left(e^{\frac{\pi}{h}d/2}+e^{\frac{\pi}{h}(x-iz)}\right)}{\left(1+e^{\frac{\pi}{h}(x-iz)}\right)}\right) + \ln\left(\frac{\left(e^{\frac{\pi}{h}(d/2+x)}+e^{-i\frac{\pi}{h}z}\right)}{\left(e^{\frac{\pi}{h}x}+e^{-i\frac{\pi}{h}z}\right)}\right)\right]\\
&= \frac{iA}{2\pi}\left[\lim_{d\to 0^+}\frac{1}{d}\ln\left(\frac{\left(e^{\frac{\pi}{h}x}+e^{i\frac{\pi}{h}z}\right)}{\left(e^{\frac{\pi}{h}(d/2+x)}+e^{i\frac{\pi}{h}z}\right)}\right) + \lim_{d\to 0^+}\frac{1}{d}\ln\left(\frac{\left(1+e^{\frac{\pi}{h}(x+iz)}\right)}{\left(e^{\frac{\pi}{h}d/2}+e^{\frac{\pi}{h}(x+iz)}\right)}\right) + \right.\\
&\qquad\left. \lim_{d\to 0^+}\frac{1}{d}\ln\left(\frac{\left(e^{\frac{\pi}{h}d/2}+e^{\frac{\pi}{h}(x-iz)}\right)}{\left(1+e^{\frac{\pi}{h}(x-iz)}\right)}\right) + \lim_{d\to 0^+}\frac{1}{d}\ln\left(\frac{\left(e^{\frac{\pi}{h}(d/2+x)}+e^{-i\frac{\pi}{h}z}\right)}{\left(e^{\frac{\pi}{h}x}+e^{-i\frac{\pi}{h}z}\right)}\right)\right]\\
&= \frac{iA}{2\pi}\frac{\pi}{2h}\left[-\frac{1}{1+e^{\frac{\pi}{h}(-x+iz)}} - \frac{1}{1+e^{\frac{\pi}{h}(x+iz)}} + \frac{1}{1+e^{\frac{\pi}{h}(x-iz)}} + \frac{1}{1+e^{\frac{\pi}{h}(-x-iz)}}\right],
\end{aligned}
\tag{A.1}
$$

using $\lim_{r\to 0^+}\frac{1}{r}\ln\left(\frac{ae^{\gamma r}+b}{a+b}\right) = \frac{a\gamma}{a+b}$. From Eq. (A.1) we can verify that $\Im\{\lim_{w\to 0}\phi\} = 0$ as it should be. So ϕ is given by the real part of Eq. (A.1) which is:

$$
\begin{aligned}
\lim_{w\to 0^+}\phi &= \Re\left[\lim_{d\to 0}\phi\right]\\
&= \frac{iA}{2\pi}\frac{\pi}{2h}\frac{2i\sin(\frac{\pi}{h}z)}{\cos(\frac{\pi}{h}z)+\cosh(\frac{\pi}{h}x)}\\
&= -\frac{A}{2h}\frac{\sin(\frac{\pi}{h}z)}{\cos(\frac{\pi}{h}z)+\cosh(\frac{\pi}{h}x)}
\end{aligned}
\tag{A.2}
$$

By insertion, Eq. (A.2) can be seen to satisfy the Laplace equation. To check whether Eq. (A.2) also satisfies the $\delta(x)$-boundary condition, Eq. (**??**), we investigate the limit

$z \to \pm h$. This limit is evaluated for two different cases, for $x \neq 0$ and $x \to 0$.

for $x \neq 0$:

$$\lim_{z \to \pm h \mp} \left(\lim_{d \to 0^+} \phi \right) = \lim_{z \to \pm h \mp} -\frac{A}{2h} \frac{\sin(\frac{\pi}{h}z)}{\cos(\frac{\pi}{h}z) + \cosh(\frac{\pi}{h}x)}$$

$$= 0$$

$$= \mp V d\delta(x) \ , \ \ x \neq 0$$

for $x = 0$:

$$\lim_{z \to \pm h \mp} \lim_{d \to 0^+} \phi \approx \lim_{z \to \pm h \mp} \left(-\frac{A}{2h} \frac{\sin(\frac{\pi}{h}z)}{\cos(\frac{\pi}{h}z) + \left(1 + \frac{\pi^2 x^2}{2h^2}\right)} \right) \ , \ \ x \approx 0 \qquad \text{(A.3)}$$

$$\approx \lim_{z \to \pm h \mp} -\frac{A}{2h} \frac{-\frac{\pi}{h}(z \mp h)}{\frac{\pi^2}{2h^2}(z \mp h)^2 - 1 + \left(1 + \frac{\pi^2 x^2}{2h^2}\right)} \qquad \text{(A.4)}$$

$$= \lim_{\alpha \to 0 \mp} \frac{A}{2h} \frac{2h}{\pi} \frac{\alpha}{\alpha^2 + x^2}$$

$$= A \lim_{\alpha \to 0 \mp} \frac{1}{\pi} \frac{\alpha}{\alpha^2 + x^2}$$

$$= \mp A\delta(x)$$

$$= \mp V d\delta(x),$$

where in Eq. (A.3) and Eq. (A.4) $\cosh(\frac{\pi}{h}x)$ and $\sin(\frac{\pi}{h}z)$ and $\cos(\frac{\pi}{h}z)$ have been taylor expanded to second order about $x = 0$ and $z = h$ respectively. Also the substitution $\alpha = z \mp h$ has been used.

Appendix B

The dipole moment of a dielectric sphere in a homogeneous field

Calculating the dipole moment of a linear dielectric sphere placed in a homogeneous electric field is a standard electrostatic problem, see [35], of which the highlights will be given in the following. We start out by finding the potential from which we will get the **E**-field
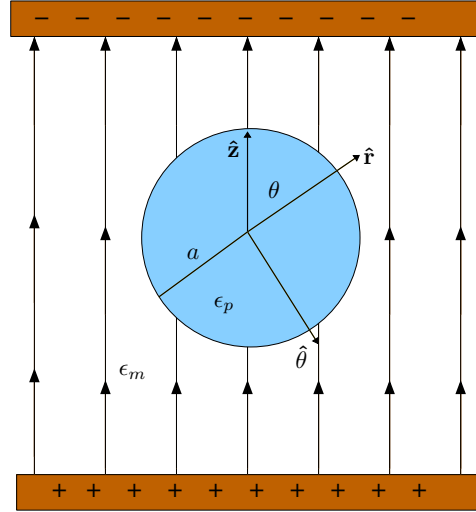
Figure B.1: A linear dielectric spherical particle of radius a is subjected to a homogeneous electric field. The permittivities of the particle and surrounding media are ϵ_p and ϵ_m, respectively.

generated by the particle. By comparing this **E**-field with that of a dipole which is (in polar coordinates):

$$\mathbf{E}_{\text{dip}} = \frac{p}{4\pi\epsilon_m r^3} \left(2\cos(\theta)\hat{\mathbf{r}} + \sin(\theta)\hat{\theta} \right) \tag{B.1}$$

we deduct the mathematical form of the dipole. In Fig. B.1 we see that the external **E**-field is given by:

71

$$\mathbf{E}_{\text{ext}} = E_0 \hat{\mathbf{z}},$$

and thus according to Eq. (2.3) ϕ_{ext} is given by:

$$\begin{aligned} \phi_{\text{ext}} &= -E_0 z \\ &= -E_0 r \cos(\theta) \end{aligned} \tag{B.2}$$

The three boundary conditions for ϕ are: continuity of the potential across the dielectric interface, the boundary condition for the electric flux density $\mathbf{D}$, cf. Eq. (2.8), when no free charge is present [1], and the fact that ϕ_{dip} must die out very far away.

$$\phi_{\text{in}}|_{r=a} = \phi_{\text{out}}|_{r=a} \tag{B.3a}$$

$$\epsilon_p \partial_r \phi_{\text{in}}|_{r=a} = \epsilon_m \partial_r \phi_{\text{out}}|_{r=a} \tag{B.3b}$$

$$\phi_{\text{out}}|_{r=\infty} = \phi_{\text{ext}} \tag{B.3c}$$

The general solution to the Laplace equation Eq. (2.2) in the presence of azimuthal symmetry as in this problem is given by a sum of Legendre Polynomials:

$$\phi = \sum_{l=0}^{\infty} \left(A_l r^l + \frac{B_l}{r^{l+1}} \right) P_l \left(\cos\left(\theta\right) \right) \tag{B.4}$$

To avoid a diverging potential and satisfy Eq. (B.3c) we must demand that

$$\phi_{\text{in}} = \sum_{l=0}^{\infty} A_l r^l P_l \left(\cos\left(\theta\right) \right) \quad , \quad r < a$$

$$\phi_{\text{out}} = -E_0 \cos(\theta) + \sum_{l=0}^{\infty} \frac{B_l}{r^{l+1}} P_l \left(\cos\left(\theta\right) \right) \quad , \quad r > a$$

Inserting these solutions into the boundary conditions Eqs. B.3, keeping in mind that $P_1 \left(\cos\left(\theta\right) \right) = \cos\left(\theta\right)$ we get:

$$A_l = B_l = 0 \quad , \quad \text{for } l \neq 1$$

$$A_1 = \frac{-3\epsilon_m}{\epsilon_m + 2\epsilon_p} E_0$$

$$B_1 = \frac{\epsilon_p - \epsilon_m}{\epsilon_p + 2\epsilon_m} a^3 E_0 \tag{B.5}$$

---

[1]In Eq. (B.3b), Eq. (2.9) and Eq. (2.3) have been used to write this boundary condition in terms of ϕ instead of $\mathbf{D}$.

giving a potential and **E**-field

$$\phi_{\text{out}} = -E_0 r \cos(\theta) + \frac{\epsilon_p - \epsilon_m}{\epsilon_p + 2\epsilon_m} a^3 E_0 \frac{\cos(\theta)}{r^2} \tag{B.6}$$

$$\mathbf{E} = \left(E_0 \cos(\theta) + 2 \frac{\epsilon_p - \epsilon_m}{\epsilon_p + 2\epsilon_m} a^3 E_0 \frac{\cos(\theta)}{r^3} \right) \hat{\mathbf{r}}$$

$$+ \left(-E_0 \sin(\theta) + \frac{\epsilon_p - \epsilon_m}{\epsilon_p + 2\epsilon_m} a^3 E_0 \frac{\sin(\theta)}{r^3} \right) \hat{\theta}$$

$$= E_0 \hat{\mathbf{z}} + \frac{\epsilon_p - \epsilon_m}{\epsilon_p + 2\epsilon_m} \frac{a^3 E_0}{r^3} \left(2 \cos(\theta) \hat{\mathbf{r}} + \sin(\theta) \hat{\theta} \right)$$

$$= \mathbf{E}_{\text{ext}} + \mathbf{E}_{\text{dip}}$$

and comparing with Eq. (B.1) we see that

$$p = 4\pi \epsilon_m \frac{\epsilon_p - \epsilon_m}{\epsilon_p + 2\epsilon_m} a^3 E_0. \tag{B.7}$$

Appendix C

Process sequence for SU8-chip

- 1. Cleaning of wafers: Washing in ultrasound bath for 10 min with soap. Rinse 10min in Piranha (4:1 H2SO4: H2O2).

- 2. Dehydration of wafers: Dehydrate wafers in 120 C oven for approx one hour.

- 3. HMDS: HMDS treatment for $\frac{1}{2}$ hour. Use recipe 4.

- 4. Spincoating with photoresist for lift-off: Track 1, 1.5 m AZ5214 resist, softbake (recipe: pr1_5 on 90 C hotplate).

- 5. Photolithography: UV exposure through mask 1 "metal", 5 seconds exposure time, 275W const. Power, hard contact mode.

- 6. Image reversal: Reverse bake on 120° C hotplate for 2min, UV flood exposure wafers for 50 sec.

- 7. Development of resist: Develop wafers in a 1 AZ351B: 5 DI water solution for about 1 min. (800mL developer and 4 L DI water). Rinse for 5 min. in bubble bath.

- 8. Plasma asher: 100W, 20sec, recipe 11. (Gas1 (O2): 100 mL/min.)

- 9. Metal deposition: Alcatel: Deposition of 10nm Ti followed by 200nm Au. (Alcatel unit: kÅ)

- 10. Lift-off: Lift-off bath (acetone) with ultrasonic agitation 10-15min. Bubble bath for 5 min.

- 11. Plasma asher: 100W, 1min, recipe 11.

- 12. Dehydrate bake: Leave in 250 C oven overnight, and prepare SU-8 25.

- 13. Spinning of SU-8 layer for channel definition. KS-Spinner. Type: SU-8 25 Take wafer directly from oven. Dispense approximately 4 ml SU-8 on the wafer. Automatic dispenser: "inner scale": 2, time: 2 sec. Spinner program: "amj-deep-experimental" Ramp to 500 rpm at 100 rpm/second acceleration and hold for 5-10

seconds. Ramp to 1250 rpm at an acceleration of 300 rpm/second and hold for a total of 30 seconds.

- 14. Softbaking of SU-8 Wipe wafers with acetone on backside. Hotplate Softbaking program: Ramp for 10 min. to 95°C. Hold for 20 min. Cool down (over 2 hours) to room temperature. Cool down to room temperature.

- 15. Photolithography KS-Aligner. Mask 2: channel definition Constant power 275W. Soft or hard contact. Exposure time 25 seconds.

- 16. Post Exposure Bake Hotplate Post Exposure Bake Ramp for 20 min. to 95°C. Hold for 5 min. Cool down to room temperature.Cool down to room temperature.

- 17. Development of SU-8 Develop in PGMEA. Approximately 5 min. in developer labeled "SU-8 first" Approximately 2 min. in developer labeled "SU-8 final" Check for remainders of SU-8. If any SU-8 left, develop again. Rinse in PGMEA and isopropanol and drie with N2.

Appendix D

SU-8 to SU-8 bonding of lid to chip

- 1. Cleaning of wafers Wash in ultra-sound bath with triton-soap. rinse 10min in 7-UP (4:1 H2SO4: H2O2).

- 2. Dehydrate bake: Bake in 250 C oven overnight. SU-8 2005 is a standard SU-8 placed at the spinnes place.

- 3. Spinning of SU-8. A layer of SU 2005 is spin coated on the wafer. KS-Spinner. Type: SU-8 2005 Take wafer directly from oven. Dispense approximately 4 ml SU-8 on the wafer. Ramp to 500 rpm at 100 rpm/second acceleration and hold for 5 seconds. Ramp to 3000 rpm at an acceleration of 300 rpm/second and hold for 30 seconds. Program: amj-thn-su8

- 4. Softbake Hotplate Ramp for 10 min to 90 C (5 C less than standard protocol to enhance polymerization in the bonding). Hold for 2 min. Cool down to room temperature. OR Softbake on the KS Spinner Bake program: SU-8 2005 (bakes at 90 C) or AMJ 2005 (bakes at 70 C).

- 5. Protection of the SU-8 Cover the wafer with blue film and black film to protect from light. Take the wafer out of the cleanroom in a lightproof box.

- 6. CO2 laser definition of pattern in the wafer Place the wafer on the holder in a position that gives a good position of the hole-pattern. Burn the pattern on both side of the wafer. REMEMBER: Orientation of the wafer. Holes to the electrodes must be placed beneath the the channel.

- 7. Making the holes Make the holes using the powder blaster

- 8. Hand alignment of lid to channel structure. Clean and wash the blue/black film on the wafer. Bring the wafer to the cleanroom entry and was thoroughly the wafer. Position the lid on the channel structure so the lid holes and inlets/outlet fits.

- 9. Heat and pressure: SU-8 to SU-8 bonding EVG NIL bonder Program: SU-8/SU-8

- 10. Alignment and exposure in the KS Aligner The structure on the lid should be aligned with the mask: channel. Settings: 35 seconds exposure time, constant power of 275W. Soft or hard contact mode.

- 11. Post Exposure Bake Hotplate Ramp for 10 min to 95 C. Hold for 2 min. Cool down to room temperature.

- 12. Development Develop in PGMEA. First in developer labeled "SU-8 first". Rinse carefully with PGMEA in lid through holes. Then in developer labeled "SU-8 final". Rinse in PGMEA and isopropanol and drie with N2.

Appendix E

Equipment and materials

E.1 Equipment

- CO_2-Laser: Synrad Duo-Lase.

- Pumps: Harvard PHD 2000.

- Waveform Generator: Wavetek 40 MHz Universal Waveform Generator 195.

- Oscilloscope: Hewlett Packard 54602A.

- Microscope: Olympus BX51.

- Camera adapter: Sony CMA-D2.

- Multimeter: Fluke 26 III.

- Drill: RS-606-478 variable speed p.c.b. drill.

- Conductivity meter: MeterLab CDM210, Radiometer

E.1.1 Software

- CO_2-laser CAD-program: WinMark 4.6.0 Synrad

- Mathematical program packages: Mathematica 5.1, Maple 9

- Simulation: FemLab 3.1 Comsol AB, MatLab 7.0 The MathWorks Inc.

- Lithographic mask design: L-Edit 11.0 Tanner Research Inc., Prometheus

E.2 Materials

- Double-sided tape: Tesa® 4982, Thickness: 4 mil = 101.6 μm, adhesion: oz/in-90, adhesive: acrylic, temp. resistance: 200°C.

- Protective blue film: Nitto Plastic SWT 20, basefilm: PVC, adhesive material: acrylic, film thickness 70 μm, adhesive thickness 10 μ.

- Black light-proof tape: Nitto Plastic 21BK (thickness 0.19 mm).

- Photo resists: AZ5214E, SU-8-25 and SU-8-2005 MicroChem Inc.

- Deveolpers: propylenglycolmonomethyletheracetat (PGMEA) for developing SU-8, AZ351B for developing AZ5214E.

- Glass wafers: Borofloat $^{®}$, thickness 0.5 mm

- Drill pieces: Komet Diamant Cylinder, DanDental (Brasseler GmbH & Co., stock no. 835 314 008 and 835 204 008).

- Powder (powder blasting): Aluminum Oxide 110 micron tan, Danville Engineering.

- Soap: Triton X-100

- Commercial Glue: Loctite 401, 420 and 431 (cyanoacrylat), Loctite Denmark A/S.

- Home-made glue: Kontakt Lim Super S9 (Casco A/S) mixed with toluene in various proportions.

- Polymers: PMMA thickness 1.5 mm, PET-A thickness 0.2 mm, PET-A thickness 0.75 mm (Nordisk Plast).

- ITO coated polymer: ITO (In_2SNO_5) on PET slide, (thickness 0.2 mm, resistance 8-12 Ω) Sigma-Aldrich Co.

- Fluorescent label: FITC (fluorescein 5-isothiocyanate), Sigma-Aldrich Co.

- Ministac fittings: Upchurch Scientific, M-644-03 and M647
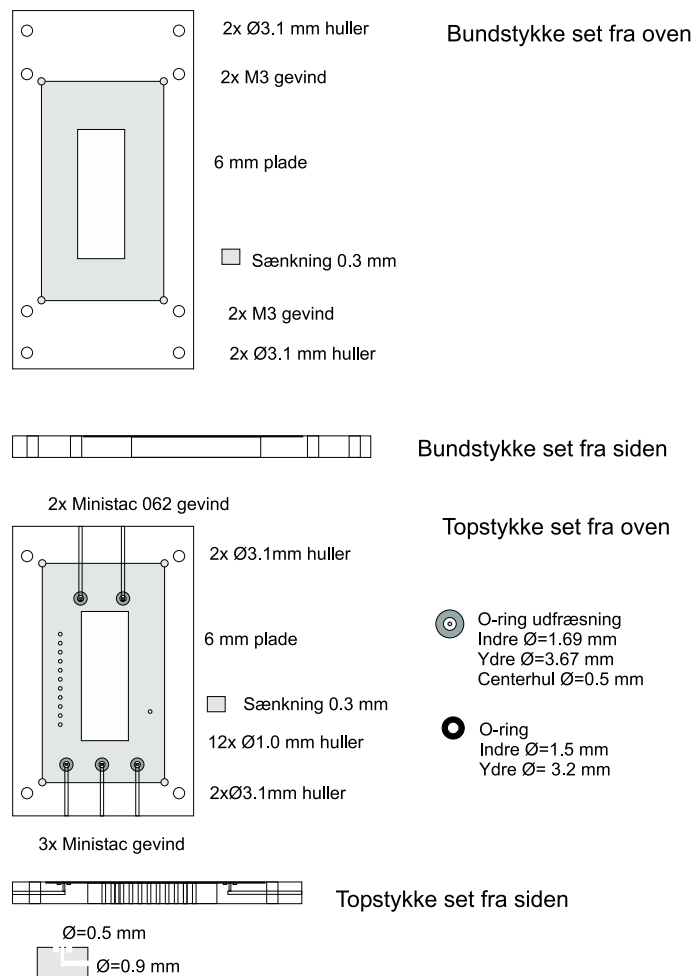
Appendix F

Chip holder design

2x Ø3.1 mm huller

Bundstykke set fra oven

2x M3 gevind

6 mm plade

Sænkning 0.3 mm

2x M3 gevind

2x Ø3.1 mm huller

Bundstykke set fra siden

2x Ministac 062 gevind

Topstykke set fra oven

2x Ø3.1mm huller

6 mm plade

O-ring udfræsning
Indre Ø=1.69 mm
Ydre Ø=3.67 mm
Centerhul Ø=0.5 mm

Sænkning 0.3 mm

12x Ø1.0 mm huller

O-ring
Indre Ø=1.5 mm
Ydre Ø= 3.2 mm

2xØ3.1mm huller

3x Ministac gevind

Topstykke set fra siden

Ø=0.5 mm

Ø=0.9 mm

Figure F.1:

Bibliography

[1] M. P. Hughes, Electrophoresis **23**, 2569 (2002).

[2] R. Zengerle, *Microfluidic Roadmap for the Life Sciences* (Books on Demand GmbH, Norderstedt, Germany, 2004).

[3] A. Wolff, Lab on a Chip **3**, 22 (2003).

[4] U. Seger, Lab on a Chip **4**, 148 (2004).

[5] H. A. Pohl, Journal of Applied Physics **22**, 869 (1951).

[6] H. Pohl, *Dielectrophoresis* (Cambridge University Press, 1978).

[7] G. A. Kallio, *Dielectrophoretic leviation of spheres and shells, M.S. Thesis*, PhD thesis, Dept. of Electrical Engineering, Colorado Stat University, 1978.

[8] T. B. Jones, Journal of Electrostatics **6**, 69 (1979).

[9] U. Zimmermann, Naturwissenschaften **69**, 297 (1982).

[10] H. Morgan, Journal of Physics D: Applied Physics **34**, 1553 (2001).

[11] R. Pethig and G. H. Markx, Trends in Biotechnology **15**, 426 (1997).

[12] Y. Huang, Physics in Medicine and Biology **37**, 1499 (1992).

[13] G. H. Markx, Journal of Liquid Chromatography and Related Technologies **20**, 2857 (1997).

[14] I. Doh, Sensors and Actuators **121**, 59 (2005).

[15] J. T. B. and K. G. A., Journal of Electrostatics **6**, 207 (1979).

[16] G. G. Stokes, Cambridge Philos. Trans. **9**, 8 (1851).

[17] S. Huang, Analytical Chemistry **74**, 3362 (2002).

[18] M. S. Markx, Journal of Biotechnology **32**, 29 (1994).

[19] A. Ajdari, Physical Review E **61**, R45 (2000).

[20] L. Ejsing, (2005).

[21] N. Asmar, *Partial Differential Equations and Boundary Value Problems* (Prentice Hall, Upper Saddle River, New Jersey, 2000).

[22] S. Choi, Lab on a Chip **5**, 1161 (2005).

[23] H. Morgan and N. G. Green, *AC Electrokinetics: colloids and nanoparticles* (Research Studies Press Ltd., Baldock, Hertfordshire, England, 2003).

[24] T. B. Jones, *Electromechanics of Particles* (Cambridge University Press, The Pitt Building, Trumpington Street, Cambridge CB2 1RP, 1995).

[25] R. Hölzel, Biophysical Journal **73**, 1103 (1997).

[26] Z. Wang, IEEE **4**, 367 (2004).

[27] Z. Wang, Lab on a Chip **4**, 372 (2004).

[28] H. Wu, Lab on a Chip **5**, 1393 (2005).

[29] F. Agirregabiria, Lab on a Chip **5**, 545 (2005).

[30] F. J. Blanco, Journal of Micromechanics and Microengineering **14**, 1047 (2004).

[31] E. Belloy, Sensors and Actuators **84**, 330 (1999).

[32] T. P. Hunt, Applied Physics Letters **85**, 6421 (2004).

[33] H. Zhou, Colloid and Interface Science **285**, 179 (2005).

[34] Z. t. Wang, (2005).

[35] D. J. Griffiths, *Introduction to Electrodynamics* (Prentice Hall, Upper Saddle River, New Jersey, 1999).